2018

Cellulose-Based Magnetoelectric Composites

Yan Zong

Intelligent Polymer Research Institute (IPRI)

Australian Institute for Innovative Materials (AIIM)

Cellulose-Based Magnetoelectric Composites

By

Yan Zong

A thesis submitted in (partial) fulfilment of the requirements for the award of the degree

Doctor of Philosophy

from

The University of Wollongong

February 2018

PUBLICATIONS

Zong, Y.; Zheng, T.; Martins, P.; Lanceros-Mendez, S.; Yue, Z.; Higgins, M. J. *Cellulose-based magnetoelectric composites*. Nature Communications **2017**, *8*, 38.

Zheng, T.; **Zong, Y.**; Yue, Z.; Wallace, G. G.; Higgins, M. J. *Magnetoelectric Composites for Bionics Applications* in Magnetoelectric Polymer-Based Composites; Wiley-VCH Verlag GmbH & Co. KGaA: **2017**, p 171.

Zong, Y.; Yue, Z.; Higgins, M. J. *Nanocrystalline cellulose for anisotropic magnetoelectric composites*. Macromolecular Materials and Engineering **2018**, *303*, 201800099.

Zong, Y.; Yue, Z.; Martins, P.; Zhuang, J.; Lanceros-Mendez, S.; Du, Y.; Higgins, M. J. *Magnetoelectric Coupling in Nanoscale 0-1 Connectivity.* (submitted)

ABSTRACT

For the modern electronic industry, miniaturized, multifunctional, low-cost and easily processable materials are always desired to meet the requirements of integrated devices. For many decades, magnetoelectric (ME) composites that allow magnetic-to-electrical signal conversion have been highly attractive for applications, including sensing, actuating, memory and energy harvesting devices. In these ME materials, such as ceramic composites $BaTiO_3/Fe_3O4$ and lead zirconate titanate (PZT)/$NiFe_2O_4$, the magnetic-to-electrical conversion is not an intrinsic property of the ME materials but is essentially due to the strain coupling between a piezoelectric (PE) and magnetostrictive (MS) materials. Most significantly, the strain-mediated output voltage of ME composites can be generated at room temperature and is an order of magnitude higher than previously studied single-phase ME crystals, *e.g.* Cr_2O_3. Thus, ME composites are considered to be suitable for practical use in electronic applications. Since PE polymers such as poly(vinylidene difluoride) (PVDF) were first introduced into ME composites in 2002, the polymer-based ME composites enabled more flexible and lighter weight candidates to replace the fragile, heavy and toxic ME ceramic composites. Polymer-based ME composites are now proving to be potential candidates in the development of portable, flexible and stretchable electronic devices.

To date, the synthetic and well-known PE PVDF and its copolymers are mostly used in polymer-based ME composites. This has led to the emergence of a central dogma where PVDF is viewed as the “material of merit” despite the enormous potential for other PE polymers to bring significant added value properties and function to ME composite devices. With the emerging area of organic bioelectronics, the desire to explore advantages of other polymers is needed to meet the increasing demands for transparent, biocompatible and biodegradable devices. In this case, naturally occurring biopolymers with inherent

piezoelectricity are undoubtedly a promising class of materials for next generation renewable ME composites in biomedical applications. Their PE properties occur from the well-aligned dipolar segments, *e.g.* the amino acid or saccharide monomers. Such PE biopolymers (*e.g.* collagen and cellulose) are widely distributed in animals or plants, providing almost an inexhaustible materials resource, as well as considerable economical benefits. This thesis has verified the possibility of using naturally occurring polymer, cellulose, as the PE phase in ME composites. ME coupling in different connectivities have been developed and the influencing factors (*e.g.* cellulose crystallinity, water content) on ME effect have been elucidated. The results are expected to promote the development of the next generation biodegradable and biocompatible ME composite by using biopolymers.

THESIS AIMS

Despite their (biopolymers) enormous potential in polymer-based ME composites, there are a number of challenges in their development for this new research field. Firstly, although PE biopolymers are abundant in nature, they usually coexist with other compounds, structures or impurities which requires further extraction and isolation and inevitably hinders their practical application. Also, the use of PE biopolymers have yet to be reported in ME composites and have very different PE mechanisms compared to traditional, well-characterized synthetic PE polymers such as PVDF. Furthermore, many PE biopolymers come in the form of various nanostructures of which their nanoscale PE mechanisms are difficult to characterize using bulk methods and poorly understood. Therefore, this field requires exploring unknown properties that may perturb the ME effect and its mechanisms. Lastly, their integration into ME composites has not been studied and will require optimization of the interactions between the PE biopolymers and the MS materials, the latter of which can commonly occur as nanomaterials (*e.g*. magnetic nanoparticles). To address the above, this thesis aimed to explore the development and use of the PE biopolymer, cellulose, as the PE component in polymer-based ME composites. Therefore, the aims of thesis were to:

1. **Explore the use of biopolymer, in particular regenerated cellulose, in ME composite.**
2. **Utilize the high crystalline form of cellulose, CNC, to optimize the performance of ME composite.**
3. **Develop nanoscale cobalt ferrite (CFO) nanoparticles/CNC nanowhiskers based ME composites to explore novel ME coupling connectivity.**

SUMMARY OF THESIS CHAPTERS

In the first introduction chapter **(Chapter 1)**, we firstly highlight the discovery and history of the ME materials and define the different configurations of ME composites and how their structure-property relationship affects the ME effect. In particular, we mainly focus on the two main classes of ME composites, the ceramic- and polymer-based ME composites. The methodologies to study ME composites are also described in this section, including using a bulk testing system for the measurement of ME output voltages and the characterization of PE materials and structures at the nanoscopic level using Piezoresponse Force Microscopy (PFM). Following this, we introduce naturally occurring biopolymers that have PE properties and represent a novel group of materials in ME composites, which are the focus of the thesis. Lastly, we describe the potential applications of ME composites, including magnetic sensors, energy harvester and biomedical devices for cell stimulation, and the benefits that naturally occurring polymers can bring to these applications.

The first experimental chapter (**Chapter 2**) employed regenerated cellulose as the PE component to fabricate ME composites. α-cellulose powder extracted from cotton was dissolved in a binary solvent system of dimethylacetamide (DMAc)/LiCl and the solution drop-cast to produce cellulose films. The ME composites were fabricated in a 2-2 connectivity, with the cellulose film combined with a MS layer, Metglas, *via* an epoxy glue to enable strain coupling. To test the effect of cellulose crystallinity on the ME composite properties, the cellulose films were either air-dried under room temperature or hot-pressed at higher temperatures to induce greater crystallinity. Differential Scanning Calorimetry (DSC) and Piezoresponse Force Microscopy (PFM) confirmed that a higher crystallinity increased the PE response, in addition to enhancing the ME coefficient, with highest values of 1.41 V

cm^{-1} Oe^{-1}. Importantly, this value is considered to be giant ME effect (>1 V cm^{-1} Oe^{-1}) and suitable for sensing or electrical stimulation applications. Interestingly, a previously predicted Fano-resonance profile in an enhanced ME response but yet to be experimentally observed for the first time in the cellulose-based ME laminates.

The second experimental chapter (**Chapter 3**) used two forms of nanocrystalline cellulose (CNC), namely the nanowhiskers and nanospheres to fabricate ME laminate composites. The CNCs were synthesised from α-cellulose powder using an acid hydrolysis method and different pre-treatments produced the different CNC structures of nanospheres or nanowhiskers. The structural and PE properties of synthesised CNCs were characterized using XRD, FT-IR and PFM and in doing so a cellulose crystal II lattice was observed for the first time in CNC. It was also verified that both types of CNCs were highly crystalline and when used in ME laminate composites with Metglas gave the highest ME coefficient of 2.33 V cm^{-1} Oe^{-1}. Highly crystalline CNC not only enhanced the ME response but also resulted in different Fano-resonance profiles than those of the regenerated cellulose composites. Moreover, by taking advantage of the low-dimensional CNC, an anisotropic ME effect was induced from composites comprising aligned CNC nanowhiskers. This represents the first observation of an anisotropic ME response occurring from the PE polymer component, with the ME output voltage giving an order of magnitude higher value compared to those in previously studied anisotropic effects in ME composites.

The third experimental (**Chapter 4**) established an ME coupling in a novel 0-1 connectivity. Specifically, the ME response was induced from interactions between the 0-dimensional MS nanoparticles and the 1-dimensional PE cellulose nanowhiskers. Two types of MS nanoparticles, either hydrophilic $CoFe_2O_4$ (CFO) or hydrophobic Cetyltrimethylammonium Bromide (CTAB) modified CFO, were used to understand the effect of physical surface

properties on the strength of ME coupling. The properties of the MS nanoparticles, CFO and CTAB-CFO, as well as the developed ME nanocomposites were characterized using different methods. It was found that the ME response was stronger when the two phases were both hydrophilic. This was due to the hydrogen bonding interactions that promoted the nanoparticles dispersion in the composite and meanwhile led to better ME effect.

Finally, the different factors that have potential to influence the ME effect are discussed in a summary/future work chapter (**Chapter 5**). Suggested future works include the introduction of new PE and MS materials, as well as the novel structural configuration of ME composites. The chapter also recommends the exploration of other PE biopolymers for ME device fabrication.

ACKNOWLEDGEMENTS

Firstly, I would like to give my great appreciation to my principle supervisor, A/Prof. Michael Higgins, and my co-supervisor, Dr. Zhilian Yue. Thanks for their guidance, support and patience during my PhD study.

Then I would like to thank my collaborators from the University of Minho, Prof. Senentxu Lanceros-Méndez and Dr. Pedro Martins. I would also like to thank them for their kind help for my graduate research as well as their warm welcome during my exchange program in Portugal.

I would also like to thank Dr. Yi Du, Dr. Jincheng Zhuang, Dr. Tian Zheng and Mr. Long Ren for their technical support. My special thanks to my best friends Dr. Hongrui Zhang, Dr. Qi Gu and Dr. Yu Chen. The wonderful memories with my friends will not be forgotten in my lifetime.

Additionally, I would like to acknowledge the Intelligent Polymer Research Institute (IPRI) for the prestigious research environment. My appreciation to all IPRI members who have worked with me in the past three years.

Finally, I would to give my gratitude to my parents. I would like to thank them for their financial support for my PhD study and, more importantly, without their understanding, encouragement and endless love I could not have made it this far.

ABBREVIATIONS

AFM	Atomic Force Microscopy
PFM	Piezoresponse Force Microscopy
SS-PFM	Switching Spectroscopy-PFM
DART	Dual AC Response Tracking
DSC	Differential Scanning Calorimetry
TGA	Thermogravimetric Analysis
SEM	Scanning Electron Microscope
FT-IR	Fourier Transform Infrared
XRD	X-Ray Diffraction
H_{ac}	Alternating Magnetic Field
H_{dc}	Constant Magnetic Field
ME	Magnetoelectric
PE	Piezoelectric
MS	Magnetostrictive
MF	Multiferroic
CNC	Cellulose Nanocrystal/Crystalline Nano-cellulose
CNF	Cellulose Nanofiber

DMAc	Dimethylacetamide
HDMS	Hexamethyldisilazane
PVDF	Poly (vinylidene fluoride)
P(VDF-HFP)	Poly (vinylidene fluoride-co-hexafluoropropylene)
P(VDF-TrFE)	Poly (vinylidene fluoride-trifluoroethylene)
PZT	Lead Zirconate Titanate
CFO	Cobalt Ferrite
CTAB	Cetyltrimethylammonium Bromide

TABLE OF CONTENTS

Chapter 1. Introduction

Magnetoelectric (ME) materials enable the conversion of magnetic energy to electrical signals and *vice versa*. The ME effect is obtained from the simultaneous existence of different orders, in particular, a magnetostrictive (MS) component and a piezoelectric (PE) component. The cross-coupling between the two orders has drawn significant interest over many decades and once the development of ME materials encounters the commercial electronic and technology industries, devices employing this sort of material will find applications, such as energy harvesting[1], magnetic sensors[2] and non-volatile memory storage devices[3]. In recent years, the introduction of synthetic PE polymers has made it possible to fabricate portable and flexible ME composites with considerable ME responses for practical use. However, there are numerous naturally occurring polymers with piezoelectricity that have not yet been explored. Introducing natural biopolymers and exploring their unknown properties are expected to bring added values for ME composites, which not only broaden the horizon of ME materials but also provide the access to next generation softer, biodegradable and more bio-compatible contactless electrodes for biomedical applications.

1.1. ME Single Crystals

Ferroic single crystals combining two or more ferroic properties are known as Multiferroics (MF) and only MF crystals consisting of ferromagnetic and ferroelectric orders exhibit an ME effect. Specifically, there are a total of 3 classes of ferroic orders (**Figure 1.1**); in ferromagnetic materials, the alignment of electron spins can be switched by a magnetic field; in ferroelectric materials, electric dipoles can be switched by an electric field; in ferroelastic materials, the strain alignment can be switched by a stress field. The cross-interaction between different orders not only preserves the properties of each ferroic order, but also results in multiple functions to MF crystals.[4] For example, MF crystals with ferromagnetic and ferroelectric coupling enable magnetic-to-electrical conversion (the direct ME effect) because the dielectric polarization can be switched in an external magnetic field and *vice versa*.[5] Hence, ME materials are extremely useful for device miniaturization as they render a single device component with more than one function or signal output.

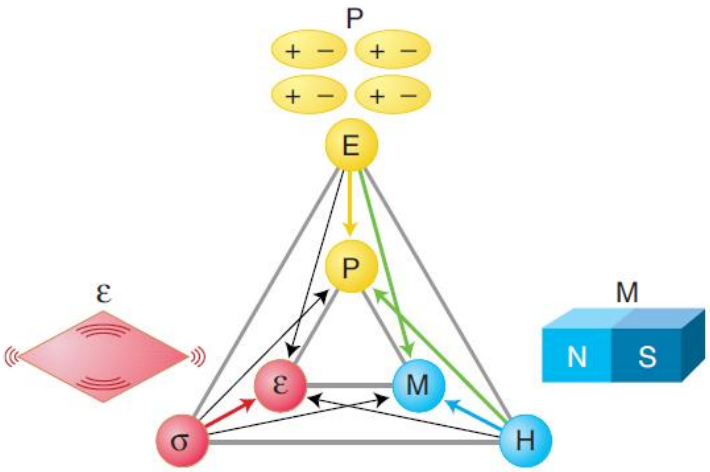

Figure 1.1. Ferroic ordering, the electric field E, magnetic field H, and stress σ, lead to a spontaneous alignment of electric polarization P, magnetization M, and strain ε, respectively.

By using ME materials, one can magnetically induce and remotely switch a localized output voltage. Generally, the direct ME response of a material is evaluated by the ME voltage coefficient (α_{ME}), which is defined as:

$$\alpha_{ME} = E/H \qquad (1.1)$$

where E and H represent the strength of the electrical and magnetic fields, respectively. The unit of α_{ME} is V cm^{-1} Oe^{-1} or mV cm^{-1} Oe^{-1}, which describes the voltage output per of the stimulating magnetic field and thickness of the material.

The ME effect was conjectured by Curie in 1894.[6] At an early stage, studies were initiated on single phase crystals and the ME effect observed for the first time in a

Cr_2O_3 crystal in 1960.[7] However, progress in further discovery of ME single crystals was relatively slow owing to the atomic level ferromagnetism and ferroelectricity that are rarely met because they require empty and partially filled transition metal orbitals, respectively.[8] This condition has not changed until theoretical breakthroughs in understanding the coexistence of magnetic and electric coupling in oxides,[8] and as a result previously unknown ME materials have now been discovered. Theoretical studies have been able to better identify MF single crystals that fulfil the requirements for ferromagnetic and ferroelectric compatibility and accelerated the discovery of ME single crystals. For example, at a critical temperature T=9K, a clear magnetic-field induced ME effect has been observed in a perovskite, $TbMnO_3$.[9]

The other issue that hinders the practical application of ME single crystals is the ultra-low Curie temperature. Bismuth ferrite is the first single crystal being realized with an ME effect at room temperature.[10,11] In recent years, some ME single crystals with high Curie temperature have been developed, *e.g.* a Z-type hexaferrite, $Sr_3Co_2Fe_{24}O_{41}$ and layers of $(LuFeO_3)_m/(LuFe_2O_4)_1$ superlattices that both yield an ME effect over T=298K.[12,13] While this is an important step towards practical devices, single phase ME crystals are not attractive for applications in the short term because none of them generate large enough α_{ME} value for practical purposes. Their actual ME voltage is not detectable and the ME effect can only be evidenced by observing the field induced domain switching using high-resolution transmission electron microscopy (TEM) and/or piezoresponse force microscopy (PFM).[12,14]

1.2. Basic Principles of ME Composites

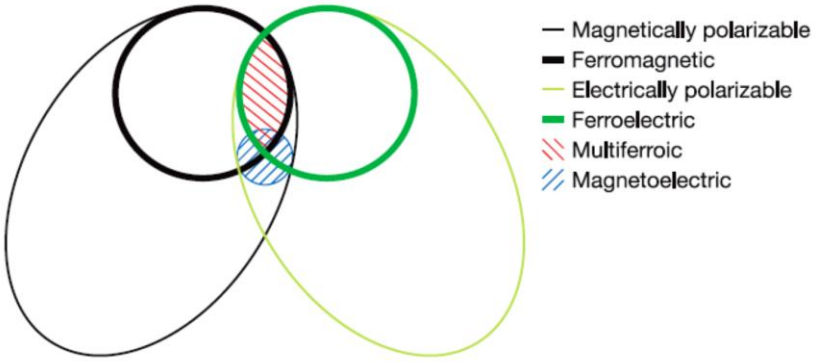

Figure 1.2. The relationship between multiferroic and ME materials.[6] The intersection (red hatching) represents materials that are multiferroic. ME coupling (blue hatching) is an independent phenomenon that can arise in any of the materials that are both magnetically and electrically polarizable. In practice, it is likely to arise in all such materials, either directly or *via* strain.

The discovery of ME composites has opened a new avenue to access the ME effect by indirect coupling and strain transfer between two orders which are magnetically and electrically polarizable, namely the MS and PE components (**Figure 1.2**). This means that the ME effect of the composite is not the natural property *per se*, as in ME single crystals, but is actually the result of strain mediated ME coupling. This approach has excluded the requirement of coexistence and compatibility of ferromagnetic and ferroelectric in oxides, but has broadened the range of useful materials to ceramics and polymers. According to the original definition proposed by Van Suchtelen,[15] the

magnetically induced dielectric polarization is known as the direct composite ME effect, where:[16]

$$\textit{Direct Composite ME Effect} = \frac{magnetic}{mechanical} \times \frac{mechanical}{electric} \quad (1.2)$$

In particular, this effect is described as an in-plane magnetic field (*H*) that induces strain in the magnetically polarizable component due to the MS effect, which is then mechanically transferred to the PE component that induces a dielectric polarization through the PE effect (**Figure 1.3a**).

On the other hand, the electrically induced magnetization change is defined as a converse composite ME effect:[16]

$$\textit{Converse Composite ME effect} = \frac{electric}{mechanical} \times \frac{mechanical}{magnetic} \quad (1.3)$$

Specifically, an out-of-plane electric field (*E*) induces strain in the electrically polarizable component due to the inverse PE effect, which is mechanically transferred to the MS component that induces a magnetization change (ΔM) or domain reorientation through the piezomagnetic effect (**Figure 1.3b**).

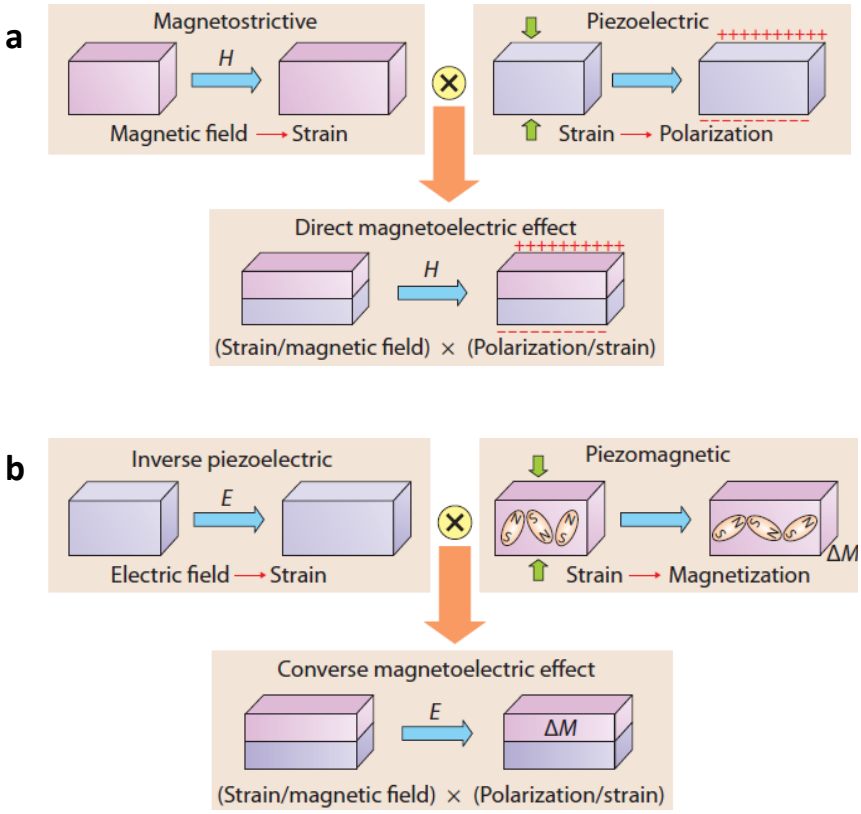

Figure 1.3. Schematic illustration of composite ME effect (a) Direct ME effect and (b) Converse ME effect.[17]

This approach allows the optimization of each individual phase, leading to enhanced α_{ME} and improved performance at room temperature. Firstly below, we separately examine the MS and PE properties and then discuss their strain-coupling mechanisms in ME composites.

1.3. Magnetostrictive (MS) Effect

The direct MS effect, which is also known as Joule effect, was first found by James Prescott Joule in the early 1840s in iron particles.[18] This effect is described as the dimension or shape change of an MS material when subjected to an external magnetic field (**Figure 1.4a**) and has been observed in other metals such as nickel and cobalt.[19,20] The reverse MS effect, which refers to the induction of a magnetic field when a MS material is deformed by an applied force, is known as Villari effect (**Figure 1.4b**).[21]

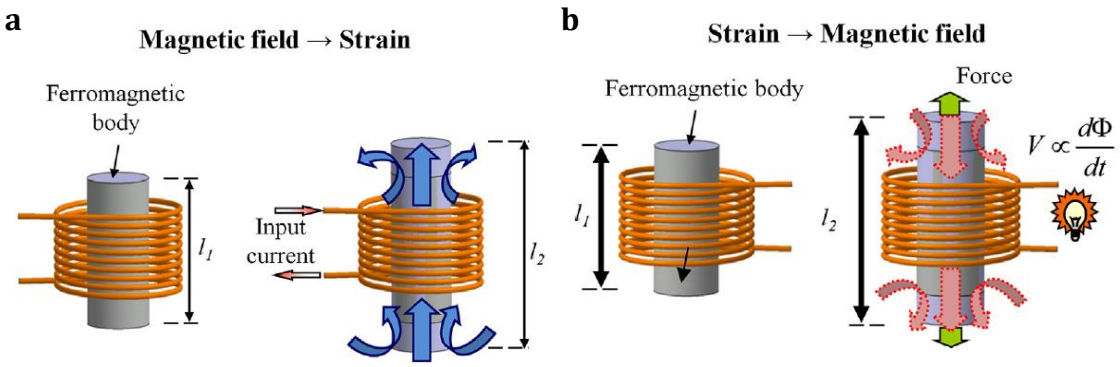

Figure 1.4. Schimetic illustration of (a) Joule effect: a magnetic field causes the shape change of an MS material and (b) Villari effect: the deformation of an MS material generates a magnetic field.[22]

The mechanism of the MS effect can be explained by two distinct processes at the microscopic level. The first one is the alignment of randomly orientated magnetic domains in the presence of an external magnetic field. The second process is more

complex but can be briefly described as the migration of domain walls in ferromagnetic materials in response to an applied magnetic field.[23] Since each domain is a region of uniform magnetic polarization and is associated with different length, the magnetically induced domain rotation and shift of domain wall causes bulk expansion or contraction, leading to strain in a MS material (**Figure 1.5**). The magnetostriction is evaluated by the length change of a MS material according to the direction of magnetic field, using unit parts per million (ppm). **Table 1.1** lists some MS materials and their magnetostriction.

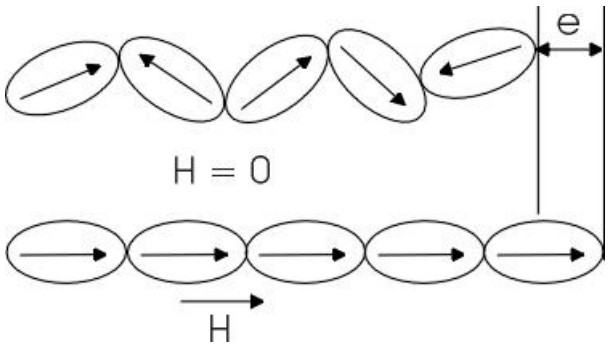

Figure 1.5. The representative mechanism of MS effect: the rotation and movement of magnetic domains causes a length change in the material.[23]

Table 1.1. Magnetostriction of MS materials (All measurements were performed under room temperature unless specified).[24]

Materials	Fe	Ni	Co	$Co_{0.5}Fe_{0.5}$	$Ni_{0.5}Fe_{0.5}$	$TbFe_2$	$Tb_{0.6}Dy_{0.4}$	Terfenol-D
Magneto-striction (ppm)	-14	-50	-93	87	19	2630	6000 (-196°C)	1620

MS materials of nickel-based alloys, which provide magnetostriction of approximately 50 ppm[18], were first used in sonars during World War II. It was later discovered that some rare earth materials, such as terbium (Tb) and dysprosium (Dy),[25,26] could induce much larger magnetostriction of up to 10,000 ppm at ultra-low temperatures, therefore their applications are strictly limited. Large magnetostriction under room temperature is achieved by alloying rare earths with 3d orbit-transition elements. For example, iron and its alloys $TbFe_2$ and $DyFe_2$ exhibit magnetostriction of 2630 ppm and 650 ppm, respectively.[26] The rare earth-based alloys, once embedded in ME composites, significantly increase the strain coupling compared to MS metals, and thus give rise to giant ME effects (α_{ME}>1 V cm^{-1} Oe^{-1}).

1.4. Piezoelectric (PE) Effect

1.4.1. Fundamentals of the PE Effect

The PE effect is the ability of PE materials to produce an electronic charge proportional to an applied mechanical stress (**Figure 1.6a**). The PE effect was discovered by Pierre Curie and Jacques Curie in 1880 and very soon after this Gabriel Lippmann realized that a reverse effect (**Figure 1.6b**), comprising a geometric strain or deformation proportional to electronic intensity, always coexists with the direct effect.[27]

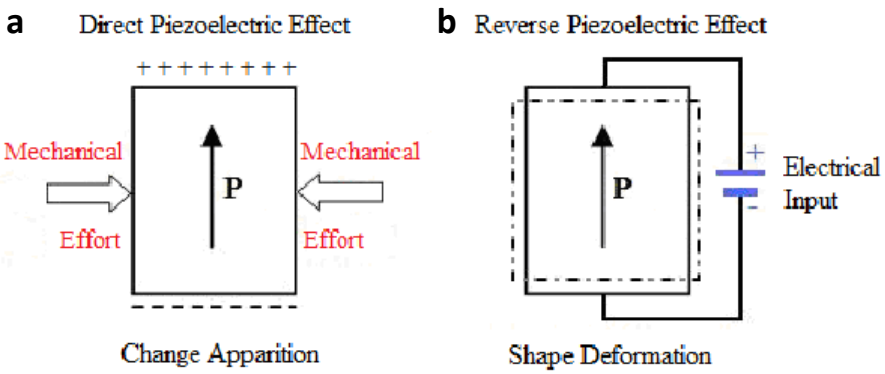

Figure 1.6. Schemetic illustration of direct and reverse PE effect.[28]

Three basic principles can be used to describe the mechanism of the PE effect. The first is the principle of dielectric constant and the second is to correlate dielectric constant to ferroelectricity. In particular, a PE effect only occurs in dielectric materials and essentially requires an anisotropic structure of the dipoles. The dipolar moments can be either ions in a crystal lattice, or positive and negative substituents in molecular groups.[29] For example, the most well-known PE polymer, poly(vinylidene fluoride-trifluoroethylene) (PVDF), is a semi-crystal polymer (**Figure 1.7a**) and its piezoelectricity comes from the positively and negatively charged atoms (or dipoles) arranged in a crystalline section but only in the configuration of a β-phase (**Figure 1.7b**).[30] An applied stress can change the distribution of positive and negative charges to induce an effective electric field (**Figure 1.7c**).[31] Interestingly, recent studies report that the PVDF piezoelectricity cannot be attributed solely to the electrostriction of the crystalline section, but is also due to electromechanical coupling between the

intermixed crystalline lamellae and amorphous regions.[32] This result has successfully correlated the PE response of PVDF and its copolymers to the dynamics of their microstructures.

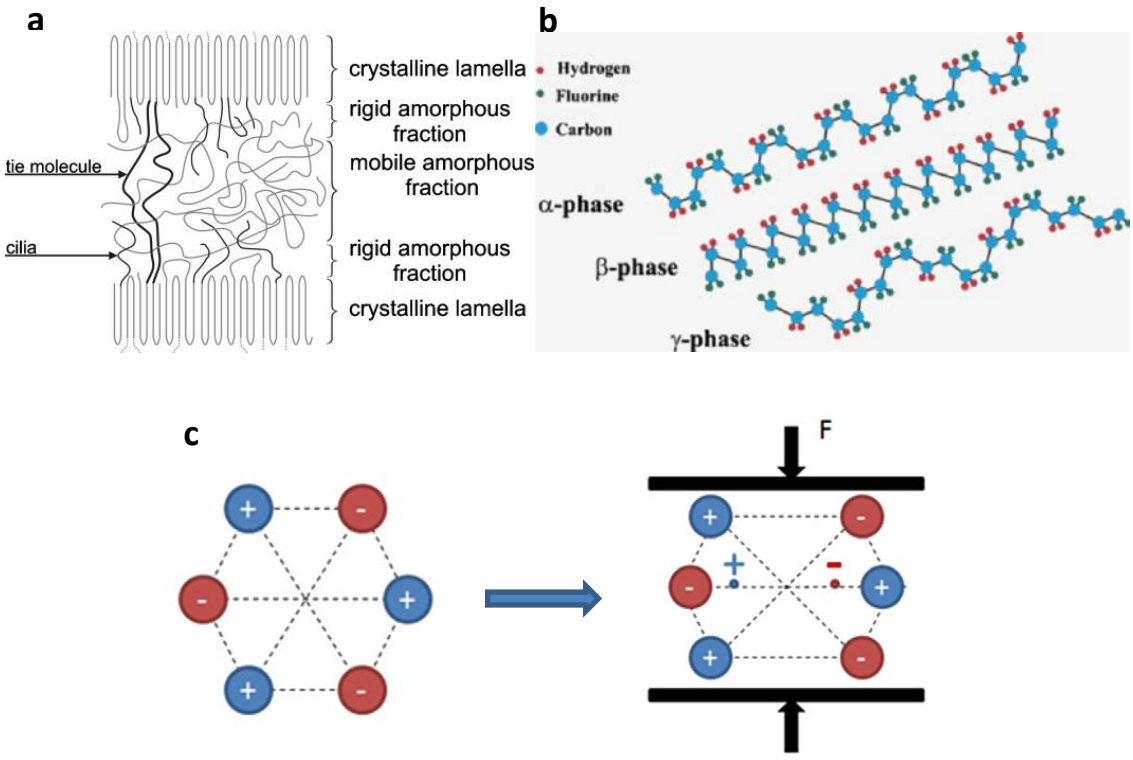

Figure 1.7. Schematic view of (a) semi-crystalline PVDF;[33] (b) the dipoles arrangement in PVDF and the PE effect occurs only in β and γ phases;[34] (c) the mechanism of PE effect described by 2D crystal structural model.[31]

1.4.2. Poling Treatment for PE Materials

The third step towards the PE effect is the poling treatment.[35] This significant step was to apply a sufficient voltage to reverse electrically dipolar moments in spontaneously polarized regions (**Figure 1.8**) in barium titanate ceramic in order to

generate a PE effect.[36] This is because PE materials possess randomly orientated electric diploes, thus rendering the overall polarization as zero. Consequently, when the material is subjected to a mechanical stress the PE effect is negligible. In contrast, after poling the diploes are electrically aligned and do not return to their original orientations. Poling treatment is of critical importance to generate and enhance the PE effect. Electrical poling is applicable to single crystals, *e.g.* quartz and Rochelle salt (sodium potassium tartrate tetrahydrate), through to polycrystalline crystal/ceramics, or even synthetic polymers, *e.g.* PVDF and its copolymers. **Table 1.2** lists some PE materials.

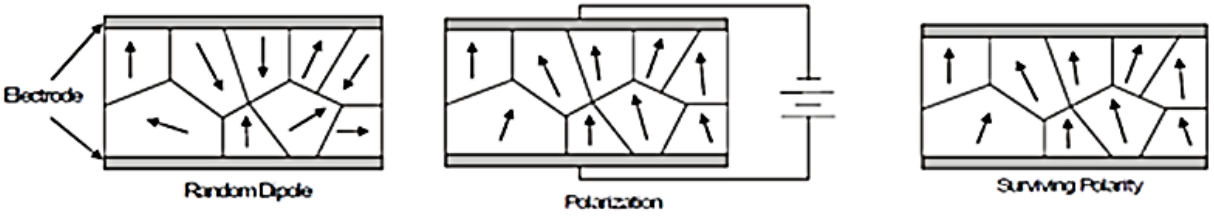

Figure 1.8. Illustration of poling treatment of materials to generate PE effect.

Table 1.2. List of Some PE Materials.

Ceramics	Synthetic Polymers	Naturally Occurring Polymers
$BaTiO_3$, ZnO, $Pb(Zr_xTi_{1-x})O_3$	PVDF, PVDF-TrFE	Cellulose, Collagen, Chitin

1.4.3. PE Modes for Polymers

In addition to synthetic PE polymers, such as PVDF, some naturally occurring polymers are also capable of generating a PE effect. The piezoelectricity of these polymers is essentially the result of their unique structure that consists of uniaxially oriented dipolar segments. A stress induced deformation leads to internal rotation of dipoles and therefore the positive and negative polarities appear on opposite faces.

Essentially the asymmetric charges in polymers gives rise to piezoelectricity; in this case, rectangular co-ordinates can be used to express the direct PE effect. More specifically, the z-axis is fixed as the axis of orientation and three components of polarization (P_x, P_y, P_z) are associated with components of stress (T_x, T_y, T_z, T_{xy}, T_{yz}, T_{xz}) as well as eighteen coefficients (d_{ij}, i=1, 2, 3 and j=1, 2, 3, 4, 5, 6) to establish the PE matrix. Three sorts of matrix are proposed for polymers with uniaxially oriented dipolar segments,[37] and some of the coefficients can be null according to their symmetry:[38]

1) C_∞ (∞)

$$\begin{bmatrix} 0 & 0 & 0 & d_{14} & d_{15} & 0 \\ 0 & 0 & 0 & d_{15} & -d_{14} & 0 \\ d_{31} & d_{31} & d_{33} & 0 & 0 & 0 \end{bmatrix}$$

2) D_∞ (∞2)

$$\begin{bmatrix} 0 & 0 & 0 & d_{14} & 0 & 0 \\ 0 & 0 & 0 & 0 & -d_{14} & 0 \\ 0 & 0 & 0 & 0 & 0 & 0 \end{bmatrix}$$

3) $C_{\infty v}$ (∞m)

$$\begin{bmatrix} 0 & 0 & 0 & 0 & d_{15} & 0 \\ 0 & 0 & 0 & d_{15} & 0 & 0 \\ d_{31} & d_{31} & d_{33} & 0 & 0 & 0 \end{bmatrix}$$

PE polymers, depending on the arrangement of their polarities, are classified approximately or exactly to a PE matrix. For example, if bio-macromolecule fibrils are heterogeneous in tissues, *e.g.* bone and tendon, the PE effect represents d_{31} and d_{33} components, corresponding to the class C_{∞}.[39] For polycrystalline with class D_{∞} symmetry, such as cellulose, chitin and chitosan, a shear component d_{14} usually dominates the PE effect. The class $C_{\infty v}$ is proposed for synthetic materials, such as electrically polarized films of polar polymers and laminate composites of ceramic particles embedded in polymers, *e.g.* PVDF and its copolymers.[40] **Figure 1.9** displays four common PE effects dominated by different modes.

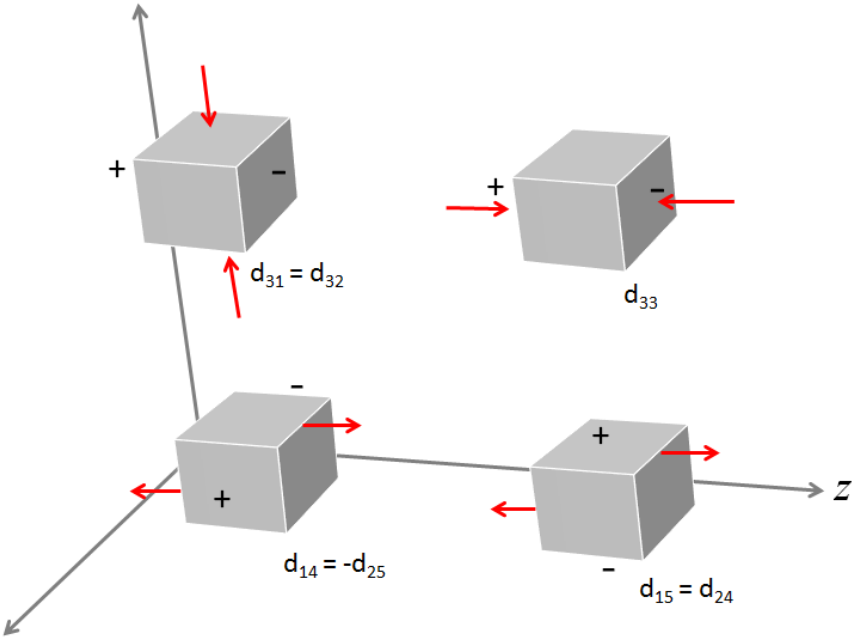

Figure 1.9. Illustration of stress induced PE effects dominated by different modes. The red arrows represent stress directions and the positive and negative polarities show the corresponding polarization status.

The PE coefficient qualifies the volume change of a PE material when it is subjected to an electric field, which is defined as:

$$d_{xy} = \frac{P}{\sigma} \tag{1.4}$$

where x and y correspond to different PE mode, P is the polarization and σ is the stress. PE coefficient can be measured by d_{33} meter or Piezoresponse Force Microscopy (PFM). The details of PFM are provided later in this chapter. If a sample is tested using a d_{33} meter the unit measured is pC N^{-1} (direct effect), while for PFM measurement the unit is pm V^{-1} (converse effect). The values from the two methods

are equivalent to each other. **Table 1.3** provides PE coefficient of different synthetic polymers.

Table 1.3. PE Coefficient of Different Synthetic Polymers.

	d_{33}	d_{31}
PVDF[41,42]	30 pC N^{-1}	20 pC N^{-1}
P(VDF-TrFE)[41]	N/A	12 pC N^{-1}

1.5. Methodology to Study the ME Effect

ME measurements involve studying both the direct and conversed ME effect, as shown in **Figure 1.10**. The direct ME effect is investigated by applying a magnetic field whilst recording the induced voltage from the ME composite. For the conversed ME effect measurement, a voltage is applied to the ferroelectric phase of the ME composite and the induced magnetic flux density associated with the ferrite phase is measured as a function of magnetic field strength.

Typically, there are three methods available to measure the ME output voltage directly. The first one is the static measurement, which records the ME output voltage as a function of increasing magnetic field.[43] In the second case, which is referred to as the quasi-static measurement[44], an impedance electrometer is employed to provide a time-varying dc magnetic field while the ME output voltage is measured as a function of time. Finally, the dynamic method simultaneously applies an ac magnetic field

superimposed onto a dc magnetic field. The ME output voltage is then recorded using a lock-in amplifier and the data is displayed as an oscilloscope.[45] **Figure 1.10** displays a schematic of the dynamic method, consisting of a pair of electromagnets to apply the dc magnetic field, Helmholtz coils to generate an alternating magnetic field, and lock-in amplifier to record ME voltage. The dynamic method is favoured to study ME composites, as it is capable of verifying a resonance enhancement by changing the frequency of the ac magnetic field. Hence, the dynamic method was used throughout the experiments in this thesis. **Figure 1.11** is the picture of the bulk testing system used to measure ME effect in this thesis.

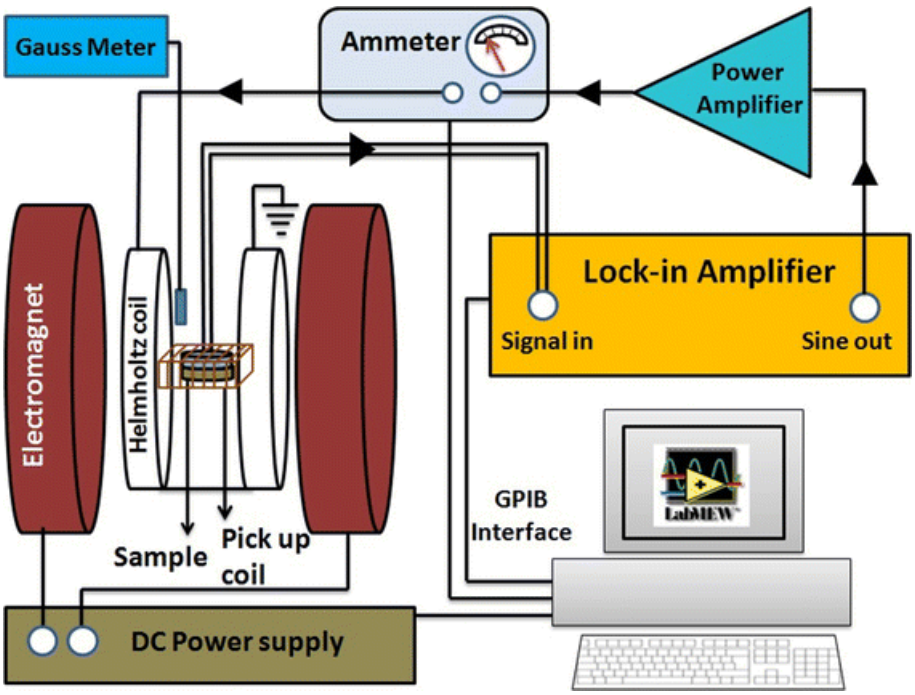

Figure 1.10. Schematic illustration of the experimental setup for measuring direct ME effect.[46]

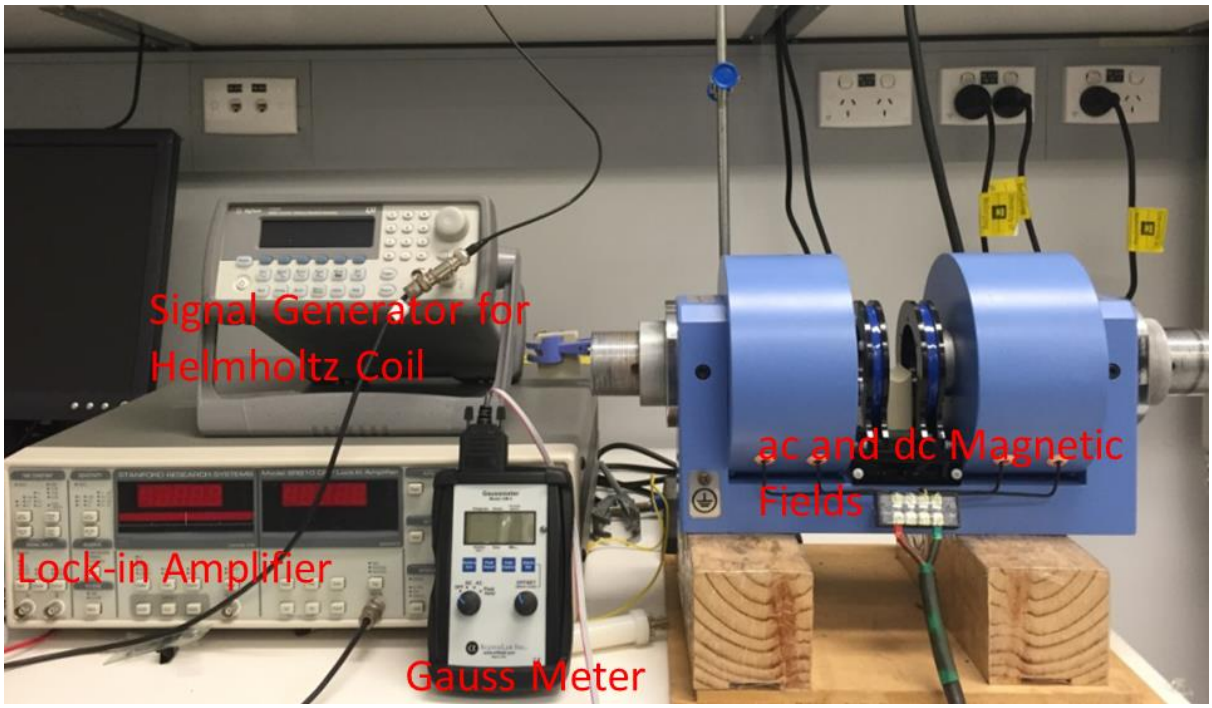

Figure 1.11. The bulk testing system for measuring direct ME effect.

Based on this method, the ME voltage coefficient is evaluated using the following equation:[47]

$$\alpha_{ME} = \frac{V_{ME}}{T \times H_{ac}} \qquad (1.5)$$

where α_{ME} is the ME voltage coefficient, V_{ME} is the actual voltage output monitored by the lock-in amplifier, T is the thickness of ferroelectric/PE phase and H_{ac} is the strength of ac magnetic field. The final unit for α_{ME} is V cm^{-1} Oe^{-1} or mV cm^{-1} Oe^{-1} depending on the property of the ME composites.

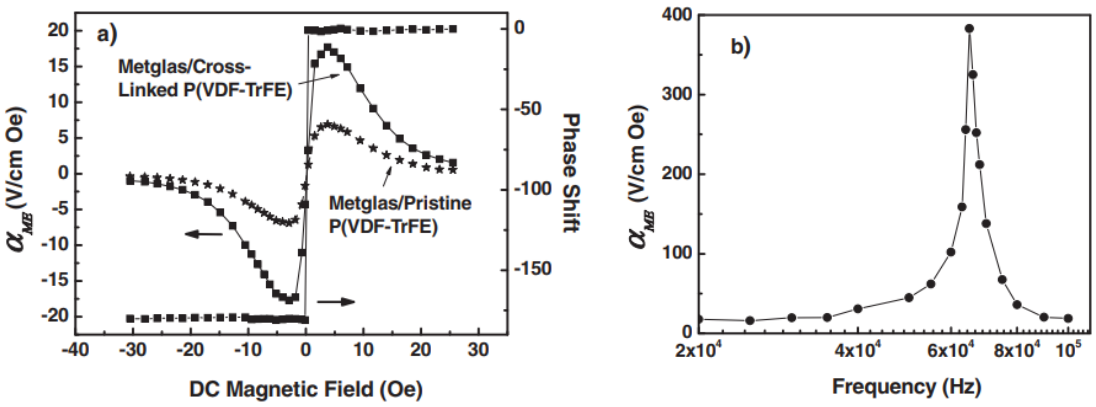

Figure 1.12. Resonance enhancement of P(VDF-TrFE) ME laminate. The length of the device is 3 cm and the peak value of α_{ME} is found at 65 kHz.[48]

Since the ME effect is induced by both constant and alternating magnetic fields, the α_{ME} values according to H_{dc} intensity and H_{ac} frequency are of significant interest in understanding the magnetic-to-electrical conversion efficiency. For example, **Figure 1.12a** shows H_{dc} dependent curves of a laminate (bilayer) ME composite, which is induced by a fixed H_{ac} and a gradually increasing H_{dc}. In the frequency-dependent curves (**Figure 1.12b**), both the H_{ac} and H_{dc} are fixed and only the H_{ac} frequency is adjusted. An interesting observation in ME laminate composites is that the α_{ME} is dramatically enhanced under the resonance excitation (**Figure 1.12b**). This unique phenomenon of ME laminates is known as the resonance enhancement effect, which is related to the properties of the MS layer. In particular, once the H_{ac} coincides with the resonant frequency of the MS structure, the mechanical strain is amplified and the α_{ME} reaches the peak value.[49] The resonant frequency of the MS layer, if oscillating

with a free end, depends on its density (ρ), Young's modulus (E) and the length (L) along the magnetic field:[50]

$$f_r = 1/2L \times \sqrt{E/\rho} \quad (1.6)$$

Hence, one can expect to accurately control the resonance enhancement of ME effect by controlling the dimensions of the laminate.

1.6. Ceramic-Based ME Composites

1.6.1. Oxides

Theoretical and experimental work in this field has mainly focused on bulk ceramic materials.[51] Various ferroelectric oxides (*e.g* $BaTiO_3$, $PbTiO_3$, $BaFeO_3$ and $Pb(ZrTi)O_3$) and ferromagnetic oxides (mainly ferrites consisting of different metal ions) have been combined *via* co-sintering methods to obtain bulk ceramic ME composites.[18,19] Generally, ceramic bulk ME materials can be classified into three types based on the connectivity of the ferromagnetic and ferroelectric phases, which are 0-3 particulate composites, 2-2 laminates and 1-3 vertical heterostructures (**Figure 1.13**).

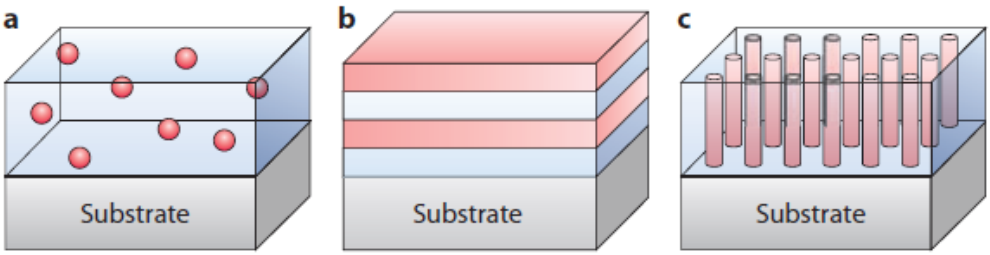

Figure 1.13. Three types of ceramic bulk ME materials: (a) 0-3 particulate composites, (b) 2-2 laminates and (c) 1-3 vertical heterostructures.[17]

In 0-3 type particulate composites with magnetic particles (0-dimension) encapsulated in the ferroelectric ceramic matrix (3-dimension), the conductive or semi-conductive ferrites particles might compromise the insulation of the composite. In these types of 0-3 composites, this is known as the current leakage problem. To avoid material defects caused by high-temperature co-firing, alternative techniques such as solution processing, microwave plasma and spark sintering have been employed to fabricate 0-3 particulate ME composites.[52-54] Although these methods have improved the ME effect to some extent, the relatively low output voltage, with equivalent α_{ME} less than 100 mV cm^{-1} Oe^{-1}, still limits the practical applications of the materials.[52-54]

The 2-2 type laminates consist of alternating ferrites and PE layers,[55] which effectively eliminates the leakage problem.[17] However, in some of the ME laminates, if the conductivity of the ferrite layers is not high enough to transmit an induced electrical signal, the loss of a direct ME output voltage is inevitable. Introducing an interface electrode between each layer can overcome this by directly collating the

output voltage from the PE layers and therefore can dramatically improve the ME response.[51] Moreover, the electrode pattern within the PE layers also influences the ME effect. For example, compared to a single layered structure, the incorporation of an intermediate PE phase to form a tri-layered geometry (**Figure 1.14**) has been shown to improve the α_{ME} from 412 to 782 mV cm^{-1} Oe^{-1}.[56] As mentioned above, the atomic interfacial inter-diffusion and thermal expansion mismatch are common problems for all ceramic-based ME composites and are extremely critical for the 2-2 type laminates. As such, low temperature processing such as pulsed laser/solution deposition has been employed to increase the ME output voltage.[57,58] In this case, the PE layer can gradually form on magnetic ferrites under relatively low annealing temperatures (600~700 °C) thus avoiding the material defects caused by high temperature co-firing.

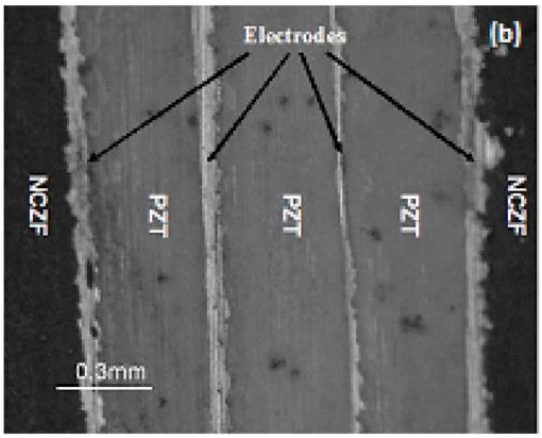

Figure 1.14. Cross-section optical image of NCZF-stack PZT-NCZF trilayer. NCZF ($Ni_{0.6}Cu_{0.2}Zn_{0.2}Fe_2O_4$) and PZT ($Pb(Zr_{0.52}Ti_{0.48})O_3$) are the MS and PE phases, respectively.[56]

The 1-3 vertically heterostructured ME composite involves magnetic spinel epitaxially embedded within the ferroelectric phase. Usually the MS pillars are grown on a substrate first and then encapsulated by a deposited PE matrix.[59,60] This vertical heterostructure has very limited connections to the substrate so higher strain transfer efficiency is expected between the MS and PE orders. However, again the α_{ME} is affected by the leakage problem caused by low resistance of the pillars penetrating through the composite bulk. The highest α_{ME} in 1-3 type ME ceramics is observed in a $CoFe_2O_4$–$BaTiO_3$ composite. The in-plane and out-plane α_{ME} values are 66 and 104 mV cm^{-1} Oe^{-1}, respectively.[61]

The studies on ceramic bulk ME composites have made great strides in understanding and optimising the strain coupling mechanisms to increase the α_{ME}. However, the material properties of ceramics, such as brittleness, low machinability and high cost, limit their practical applications. In addition, the uncertain biocompatibility may also restrict the use of ceramic ME composites for biomedical applications, at least in the short-term.

1.6.2. Rare Earth Alloys in Ceramic-Based ME Composites

A milestone in the development of ME composites was the incorporation of rare earth alloys, $Tb_{1-x}Dy_xFe_2$ (Terfenol-D), which is a type of ferromagnetic material with remarkable MS properties. Initially, a giant ME effect (α_{ME} >1 V cm^{-1} Oe^{-1}) using a Terfenol-D based ME composite was theoretically predicted by Nan *et al.* in 2001 and was later verified experimentally using lead zirconate titanate (PZT) as PE

material.[62-64] A resonance enhanced α_{ME} of ~17 V cm^{-1} Oe^{-1} is observed in a (Terfenol-D)-PZT-(Terfenol-D) sandwiched ME laminate. The greatly enhanced α_{ME} makes it feasible to use this type of ME composite for practical applications, including magnetic sensors, storage and energy harvesting devices.[65-67] Further improvement using Terfenol-D based ME composites has mainly focused on optimizing the assembly and configuration. For example, a self-amplification effect can be enabled by bonding a Rosen-type PE transformer to a classical ME sandwich consisting of two Terfenol-D layers and one $Pb(Mg_{1/3}Nb_{2/3})O_3$- $PbTiO_3$ (PMNT) layer (**Figure 1.15**).[68] This design has improved the ME voltage to 57 V cm^{-1} Oe^{-1}, which is over 50 times higher than the value in the original device without loading of secondary transformer.

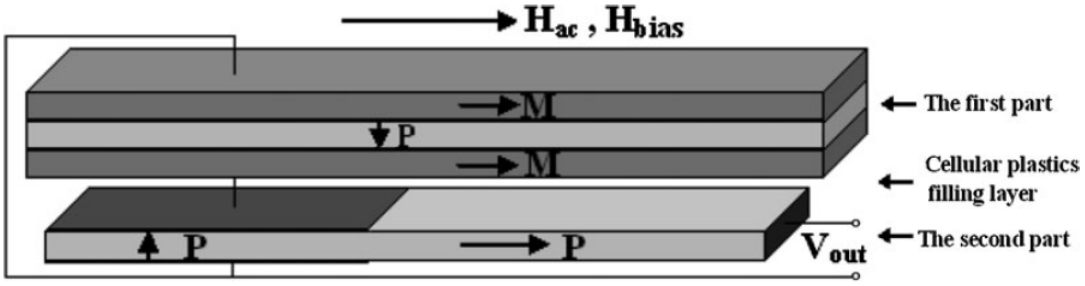

Figure 1.15. Schematic illustration of the proposed structure obtained by combining a ME laminated composite with a Rosen-type PE transformer. The first part is the ME sandwich device and the second part is the Rosen type PE transformer.[68]

Although Terfenol-D has high MS coefficient (1640 ppm),[69] it is not suitable for low magnetic field applications due to its low permeability and high field saturation

properties.[70] That is, the magnetization process is relatively slow and it is difficult to achieve the maximum magnetostriction without the presence of a strong magnetic field (>5,000 Oe).[69] Other alloys, such as Ni-Mn-Ga, Fe-Co (Permendur) and Fe-B-Si (Metglas), can be used as alternative materials, and among them, Metglas is the most promising one. Metglas is an amorphous alloy produced using a rapid solidification technique.[71] Due to its low magnetocrystalline anisotropy, Metglas possesses the unique magnetic property that allows fast and effective magnetization/de-magnetization process. More importantly, the saturation magnetostriction is reached under low magnetic fields (<10 Oe) (**Figure 1.16**).[72]

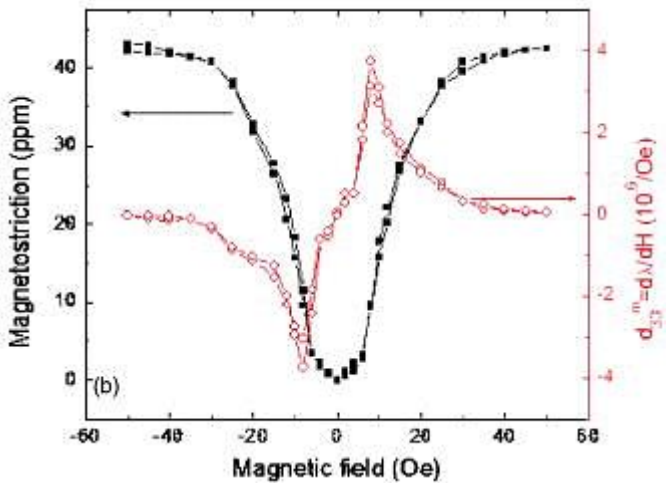

Figure 1.16. Magnetostriction (closed square) and piezomagnetic coefficient (open dot) for a Metglas 2605 SA1.[72] The piezomagnetic coefficient is the parameter to evaluate the stain transferring from MS layer (Metglas) to PE layer (PVDF). The advantage of Metglas is the low magnetic field (~5 Oe) requirement to achieve peak value of strain transfer.

Using materials with high magnetic permeability and low field saturated magnetostriction enables a high α_{ME} under weak magnetic field.[73,74] For example, a Metglas/$Pb(Mg_{1/3}Nb_{2/3})O_3$-$PbTiO_3$ laminated ME composites reaches the highest α_{ME}=19.5 V cm^{-1} Oe^{-1} under low magnetic field of 6.2 Oe,[75] and the other Metglas/PZT/Metglas sandwiched ME composites gives a peak output of α_{ME}=25.3 V cm^{-1} Oe^{-1} at ~7 Oe.[76] The ME composites based on these materials are especially promising for ultra-sensitive sensor applications.[77,78] Furthermore, a new era of ME composite research has emerged by combining Metglas and PE polymers.

1.7. Synthetic Polymer-Based ME Composites

Polymer-based PE materials take advantages of high strain transfer capacity, flexibility (*e.g.* to develop bendable or foldable ME composite) and ease of processing/machinability[79] and are therefore extremely attractive in ME devices. The most widely used PE polymers are poly(vinylidene fluoride) (PVDF) and its copolymers, poly(vinylidene fluoride-trifluoroethylene) (P(VDF-TrFE)) and poly(vinylidene fluoride-co-hexafluoropropylene) (P(VDF-HFP)). As given above, the classification of ceramic ME composites is based on the connectivity of the ferromagnetic and ferroelectric phases. Likewise, there are three types of polymer-based composites, including nanocomposites (0-3 connectivity), laminated

composites (2-2 connectivity) and polymer as a binder combining composites (0-0-3 connectivity) (**Figure 1.17**).[79]

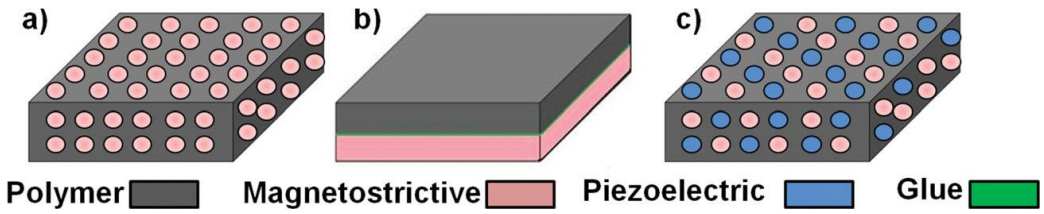

Figure 1.17. Three types of polymer-based ME materials: (a) nanocomposites (0-3), (b) laminated composites (2-2), and (c) polymer as a binder combining composites (0-0-3).[79]

In polymer-based ME nanocomposites, MS particles (*e.g.* $Ni_{0.5}Zn_{0.5}Fe_2O_4$ (NZFO) and $CoFe_2O_4$ (CFO)) are embedded in a PE polymer matrix.[80,81] This type of composite can be easily obtained using solution processing methods, however, its ME response is usually lower than ME laminates due to less MS-PE interfacial area. For example, a P(VDF-TrFE) based composite with CFO particles dispersed in the polymer matrix gives an α_{ME} of only 40 mV cm^{-1} Oe^{-1}.[80]

The polymer as a binder composites combine MS and PE particles together in a polymer matrix, and provide strain coupling between the two phases simultaneously. The first systematically studied composite of this type was that containing Terfenol-D (the ferromagnetic phase) and PZT (the ferroelectric phase) in a PVDF matrix. It was found that by optimizing the Terfenol-D fraction, the maximum ME effect could be

achieved without the leakage problem.[82] Apart from fraction optimization, well-dispersed MS particles is also desired for the purpose of improving the ME effect. The addition of surfactant is an effective approach to achieve this goal as it can enhance dispersion stability of the particles.[83,84]

Among all three types of polymer-based ME materials, laminated ME composite appears to be the most attractive one[79], namely because the ME effect is superior to the other connectivity structures. Moreover, the combination of a PE polymer and Metglas has significantly increased the α_{ME} of laminated ME composites to unprecedented values of >300 V cm^{-1} Oe^{-1}. Compared to 'conventional' PVDF/Metglas ME laminates, of which the highest α_{ME} is 238 V cm^{-1} Oe^{-1} driven at resonance frequency,[74] the improved ME voltage output is attributed to a high PE response that is achieved in a well-aligned polymer matrix. For example, the $Al(NO_3)_3$ $9H_2O$ doped P(VDF-HFP)/Metglas laminate exhibits giant α_{ME} value of 320 V cm^{-1} Oe^{-1}, which is attributed to the increased polar crystallinity and aligned hydrogen bonding network.[85] Similarly, utilizing a polymer chain-end crosslinking agent to build a oriented network in the PE polymer (**Scheme 1.1**)[48] for a P(VDF-TrFE)/Metglas laminate has led to a α_{ME} of 383 V cm^{-1} Oe^{-1}, achieving the highest reported value for polymer-based ME composites to date.

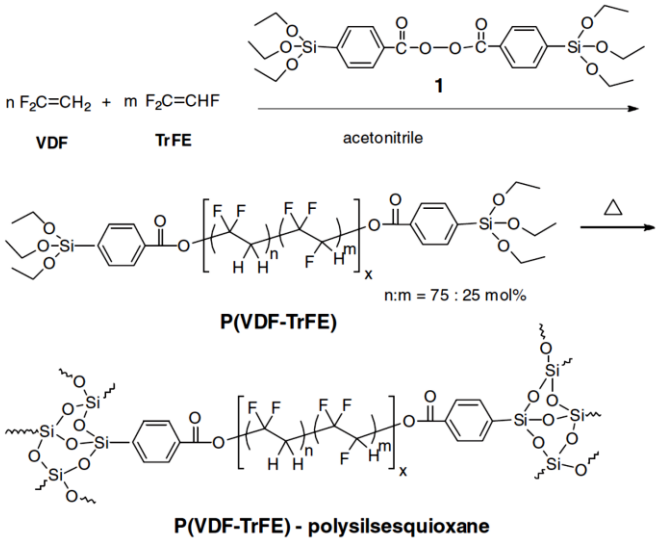

Scheme 1.1. Synthesis of cross-linked P(VDF-TrFE).

1.8. Applications of ME Composites

Due to the cross-coupling of MS and PE components, ME materials possess unusual properties and in turn render multifunction for devices, which promises the electronic miniaturization and integration of modern engineering.[86] The principle advantage of ME materials is the conversion of magnetic to electrical energy; a mechanism considered to be a magnetically switchable dipolarization process. This unique property has seen the advent of ME materials in various electronic devices, including magnetic sensors, energy harvesters and biomedical devices, which are hereforth discussed below.[87,88]

1.8.1. Magnetic Sensor

ME-based magnetic sensing devices can be based on either ceramics or polymers,[89-93] and the magnetic field strength is transduced into a reliable electrical output signal, the magnetic field can be thereby determined by measuring the generated voltage. For example, a simple but effective design for low magnetic field detection is rectangular ME laminate composites consisting of Metglas and PE component of PVDF (**Figure 1.18a**). When an ac magnetic field is applied at the ME resonance frequency, the ME output voltage is linearly proportional to the constant magnetic strength and is very sensitive to changes in the magnetic field from 0-2.0 Oe (**Figure 1.18b**).[94] It is known that the Earth's mean magnetic field is in the range of 0.4-0.6 Oe with variation according to longitude and latitude. The ME laminates provide the potential to develop a bio-mimicking navigator, which, just as migratory animals, are capable of sensing variations in geomagnetic fields. The different magnetic intensity can be correlated to the features of different geographic zones, which is helpful for compiling a map as a navigation source for long distance travel.[77]

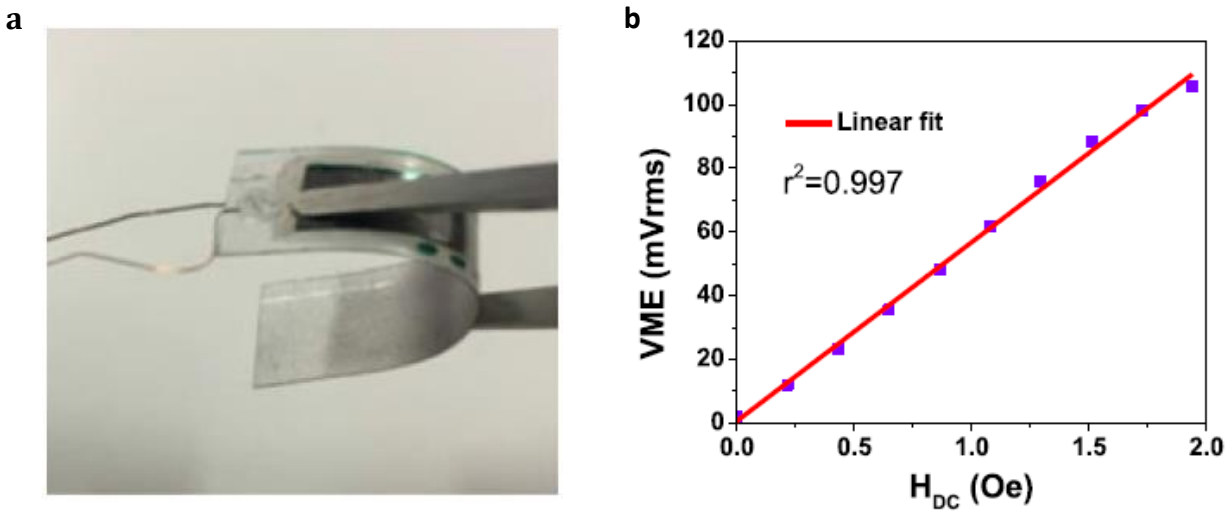

Figure 1.18. (a) Flexible PVDF/Metglas ME laminate for magnetic sensing application. (b) The linear relationship between ME output voltage and the variations of constant magnetic fields. The sample is induced by an alternating H_{ac}=0.68 Oe and at the resonance frequency of 25.4 kHz.[94]

The rectangular ME laminates are suitable for magnetic sensing, however, the applications are limited in a constant field detection. Using different configurations of ME devices one achieve measurements under complex conditions such as detecting rotating or vortex magnetic fields in power integrated circuits or superconducting films.[95-97] One example is sensing the vortex magnetic fields around live wires by employing ring-type ME laminates that can be fabricated with different outer/inter diameters depending on the diameter of wire being tested. Alternatively, the ring-type sensor is very sensitive to alternating magnetic fields induced by a wire carrying current. The measurement method is to apply an ac vortex magnetic field along the

circumferential direction of the ring consisting of MS and PE layers. The magnetic field oscillates the MS layer and excites a radial symmetric vibration in the PE layer, producing an ac voltage corresponding to the induced magnetic field (**Figure 1.19**).For example, once a vortex magnetic field induced from a wire is applied to the ring of the PZT/Terfenol-D laminate with sandwich structure (**Figure 1.19a**), the generated ME voltage displays an almost linear relationship with the magnetic strength of $10^{-9}<H_{ac}<10^{-3}$ T in the frequency range of 0.5 Hz to 2 kHz (**Figure 1.19b**).[98] To explore novel ME magnetic sensors, researchers have embedded nanomaterials in ME composites for the purpose of developing materials with anisotropic sensing ability.[99] In particular, the ME composite consists of δ-FeO(OH) nanosheets in a P(VDF-TrFE) polymer matrix and the ME effect arises from strain coupling due to the rotation of the magnetic nanosheets and not by conventional mechanisms of magnetostriction. In this case, the ME voltage coefficient is dependent on the incident magnetic field direction and intensity, with the highest α_{ME} of ~0.4 mV cm^{-1} Oe^{-1}.[99] Therefore, it is possible to test both the strength and direction of a magnetic field by monitoring the induced ME output voltage. Further studies have changed the δ-FeO(OH) to MS CoFeOOH nanosheets, and the composite possesses a similar anisotropic ME effect with enhanced α_{ME} of up to 5.0 mV cm^{-1} Oe^{-1}. As shown in **Figure 1.19c,** a testing angle of 0˚ ME voltage shows a linear relationship to the H_{dc} field from 0-1500 Oe. The H_{dc} is fixed at 500 Oe and the CoFeOOH/P(VDF-TrFE) sample is rotated from 0-360˚, and accordingly the highest ME voltage of 1.20 μV is obtained at 0˚, 180˚ and 360˚ and the lowest ME voltage of

0 mV is obtained at 90˚ and 270˚ (**Figure 1.19d**).[100] Although these studies have opened a new pathway for anisotropic magnetic sensing, it is noticeable that the ME voltage output remains relatively low with values of only a few microvolts (or α_{ME} at mV cm^{-1} Oe^{-1}). Ongoing research should focus on different nanomaterials, especially those that can generate ME voltages *via* the PE phase to improve the ME response.

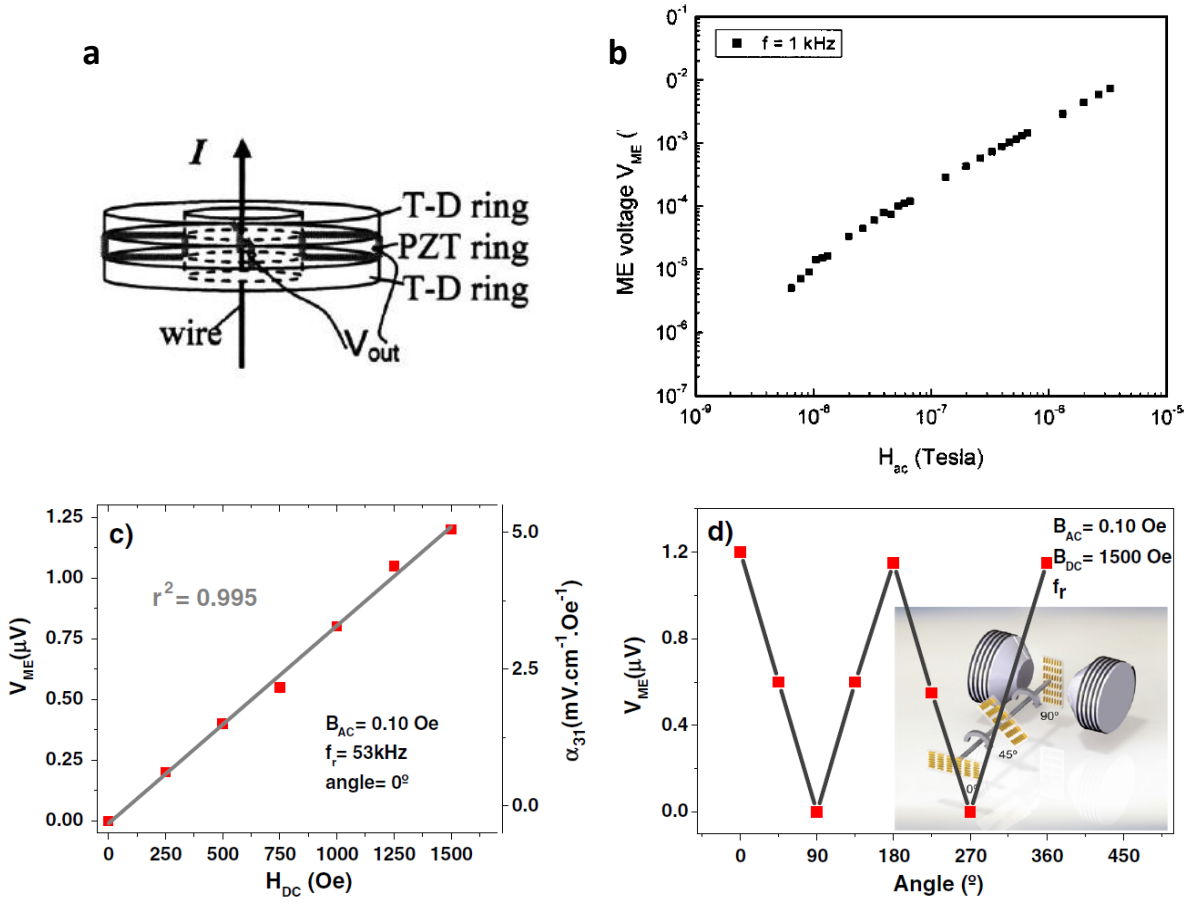

Figure 1.19. (a) Schematic illustration of vortex magnetic sensor based on ME laminate consisting of a PZT ring sandwiched by tow Terfenol-D rings. (b) Induced ME voltage as a function of magnetic field from $10^{-9}<H_{ac}<10^{-5}$ T.[98] (c) Room temperature ME voltage output ad ME voltage coefficient of CoFeOOH/P(VDF-TrFE) as a function of constant magnetic field at testing angle of 0˚. (d) Room temperature ME response of CoFeOOH/ P(VDF-TrFE) as a function of testing angles.[100]

1.8.2. Energy Harvesting Device

The principle of ME energy harvesting is using the product property of ME composites to generate electricity from a stray ac magnetic field, which usually occurs around live wires, vehicles and industrial machines. Since the ME effect is induced by the ac magnetic field, ME laminate composites showing a resonance enhancement effect are the most suitable candidates as an energy harvester (**Figure 1.20a**). For instance, a Terfenol-D plate embedded with multiple PE plates can generate electrical energy with a maximum value of 20 μW Oe^{-1}[1101]. Metglas/PZT ME laminates with a free-ending cantilever structure can generate significantly high power of 16 μW Oe^{-1} (at low frequency of 60 Hz) and 420 μW Oe^{-1} (at high frequency of 21 kHz), respectively.[102,103] To further increase the energy conversion efficiency, a dual-phase design is employed to obtain electricity simultaneously from both the ac magnetic field and mechanical vibration (**Figure 1.20b**).[104] In this specially designed structure, the induced strain from the different sources are combined together to enhance energy harvesting efficiency over 1 mW Oe^{-1}.[105,106]

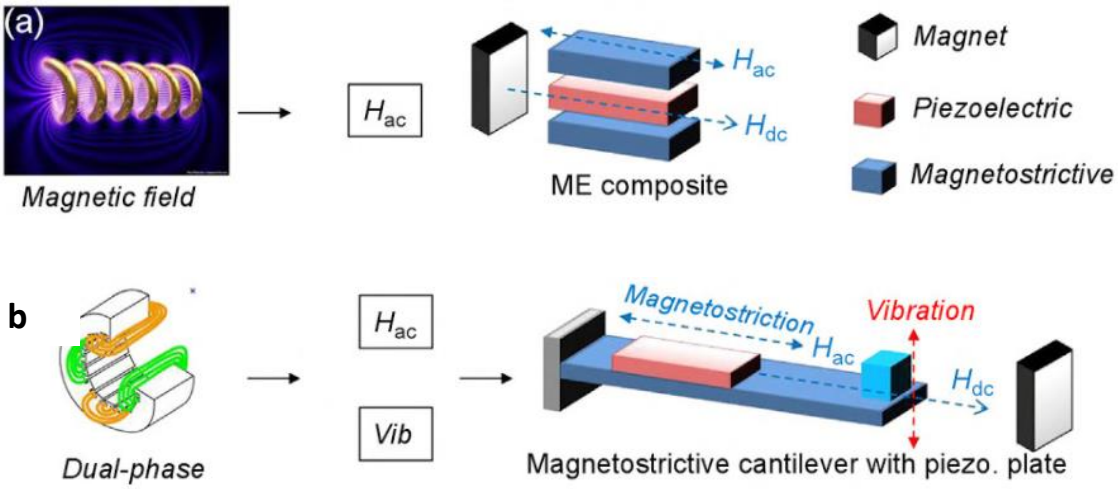

Figure 1.20. Schematic illustration of (a) energy harvester based on ME laminate and (b) dual-phase ME energy harvester.[104]

Recently, self-biased ME composites that can generate an ME voltage without the presence of dc magnetic field have attracted significant interest and among these the simple Ni/PZT bilayer design is the most promising one.[1,106-108] The self-biased ME behaviour is essentially caused by the unique properties of Ni whereby the Ni shows a lag effect in the magnetostriction, that is, when the external magnetic field is switched off the induced strain does not necessarily reach a minimum (**Figure 1.21a**). As a consequence, the α_{ME} displays a hysteresis loop with considerable ME output voltage even in the absence of magnetic stimulation (**Figure 1.21b**). This unique phenomenon is attributed to different crystallinity and domains in Ni, in contrast to Metglas, as evidenced by magnetic force microscopy (MFM) images (**Figure 1.21a**, inset). Due to the lack of grain boundaries in Metglas, its nanoscopic magnetic domains are easily

aligned to be along the orientation of the magnetic field, thus, leading to a low coercive field and high reversibility. For Ni, however, the presence of microscopic domains requires a high magnetic field to switch the orientation of the long range domains, resulting in hysteresis behaviour in the magnetostriction loop.[107] The advantage of Ni-based self-biased ME harvester is that it is extremely useful to harvest power from low frequency parasitic magnetic noise (~60 Hz) such as a power supply network that cannot be scavenged by conventional ME harvesters working in the high frequency range. A novel ME harvester based on a Ni plate combined with a $Pb(Mg_{1/3}Nb_{2/3})O_3$–$PbTiO_3$ (PMN–PT) PE layer can reach a high α_{ME} over 160 V cm^{-1} Oe^{-1} even without an applied dc magnetic field (**Figure 1.21c**). When induced by a weak ac magnetic field of 5-7 10^{-4} T at a low frequency of 60 Hz, the ME output voltage can reach up to 34 volts which is considered to be sufficient for powering low energy consuming devices (**Figure 1.21d**).[1]

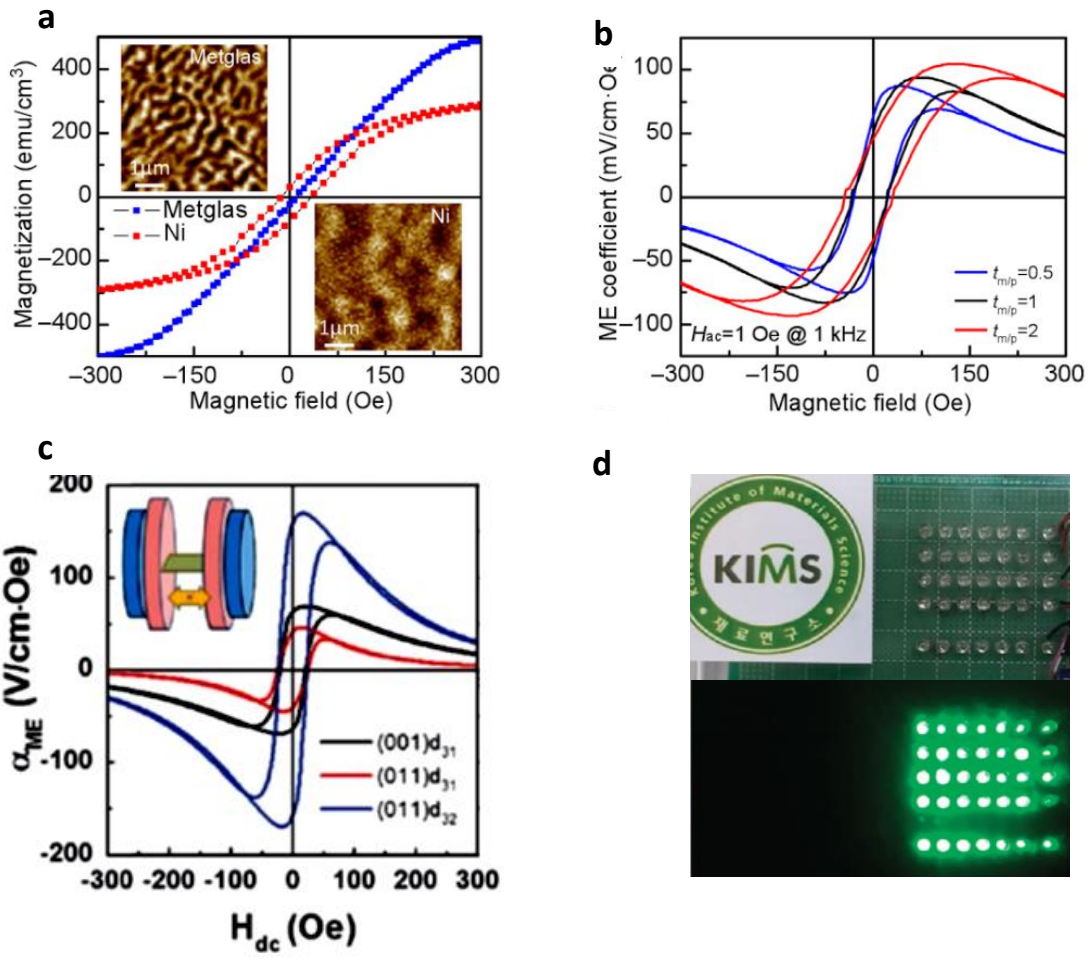

Figure 1.21. (a) Magnetostriction of Metgals and Ni, the inset section MFM images display the magnetic domains of the two materials. (b) ME hysteretic loops of Ni/PZT laminates with different magnetostictive/PE thickness ratio: $t_{m/p}$=0.5, 1 and 2.[107] (c) α_{ME} of Ni/PMN-PT laminate as a function of dc magnetic field. (d) Using Ni/PMN-PT laminate harvester as power source to turn on LED matrix.[1]

Although ME energy harvesters provide an additional power source to satisfy the increasing demand of portable devices, a noticeable problem is that the energy harvesting devices are typically based on ceramic ME composites. This has potential to hinder their use in modern flexible devices such as foldable screens for smart

phones. Instead, the use of PE polymers is attractive for the development of more flexible ME energy harvesters.

1.8.3. Biomedical Applications

The field of ME composites brings many exciting opportunities for advanced medical electronics, for example bionic devices that use implantable electrodes for electrical stimulation of cells and tissues. They can be developed as injectable and contactless electrodes with potential to enable localized electrical stimulation at the single cell level, or in tissue regions that are difficult to access in the body. For example, in the form of dispersible nano- or microparticles or soft gels, without the need for wire connections. **Figure 1.22** depicts the mechanism of ME nanoparticles for cell stimulation. Generally the stimulation is switchable by applying an external magnetic field **(Figure 1.22a),** and the stimulating process can be performed either outside the target cell using nanoparticles in body fluid or particles bound to the cell membranes **(Figure 1.22b)** or inside the target cell **(Figure 1.22b)**.[109]

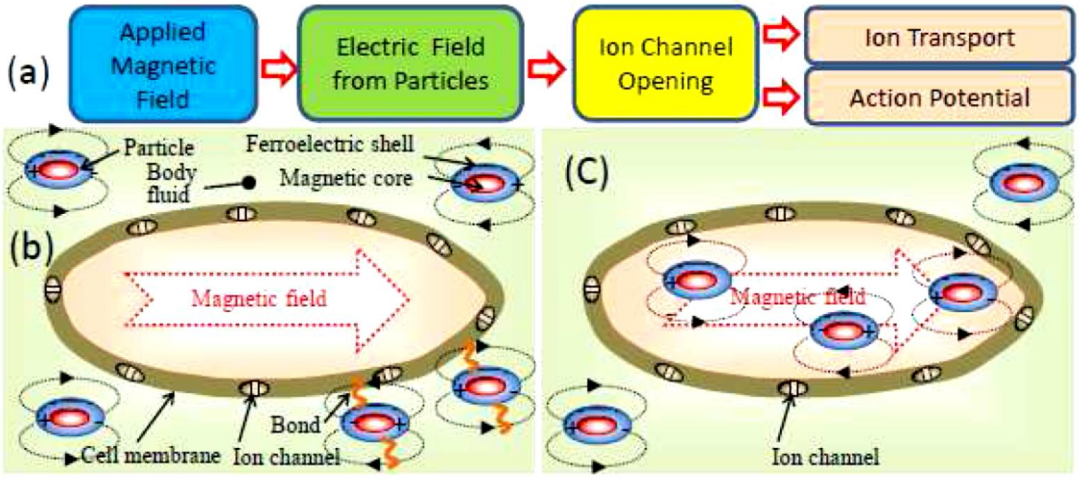

Figure 1.22. Illustration of possible mechanisms of ME nanoparticle stimulation on cell: (a) A chain of actions triggered by the applied magnetic field pulses. (b) External stimulation of the ion channels using nanoparticles in body fluid or particles bound to the cell membranes. (c) Internal stimulation of cells by uptaken nanoparticles.[109]

Theoretically, the potentials generated by micro or nanoparticles depend on the particle size. Nanoparticles as small as 50 nm with ME voltage coefficient of 5V cm^{-1} Oe^{-1} can generate a voltage of 25 mV when exposed to the field of 100 Oe (or 0.01 T). By increasing the size of the particles to 1 μm (which is still a small fraction of the cell size), the output voltage can be much higher by two orders of magnitude, which could be utilized to trigger action potential in nerves.[110] Voltages of at least ~ 15-30 mV are needed to trigger an action potential and signaling in neurons by driving the cell membrane resting potential (-65 mV) above its threshold value. Exogenous, electrical signals, as low as 5-10 mV mm^{-1}, are also important, particularly in tissue

development and regeneration. These processes provide a critical benchmark for determining the voltage ranges that must be delivered by the ME composites in order to electrically stimulate living cells. While the voltages produced by ME composites are small in comparison to those of conventional electrodes, they are ideal for electrical stimulation in the form of nanoparticles and colloids. The ability of nanoparticles to bind cell membranes, or specifically target and dock onto cell surface proteins, means that their close proximity only necessitates the use of small voltages to deliver highly localized electrical stimulation. This provides unprecedented capabilities for targeting of individual molecules, cells or a select group of cells, rather than whole tissues or organs, to enable precise control of neural function using voltages on the order of millivolts. The nanoparticles can be directed to a specific location, either through chemical functionalization of their surface or use of magnetic field gradients to guide them. A visual perspective of this is conveyed in **Figure 1.23** by showing an array of interacting nanoparticle electrodes in 3-dimensional space.[111]

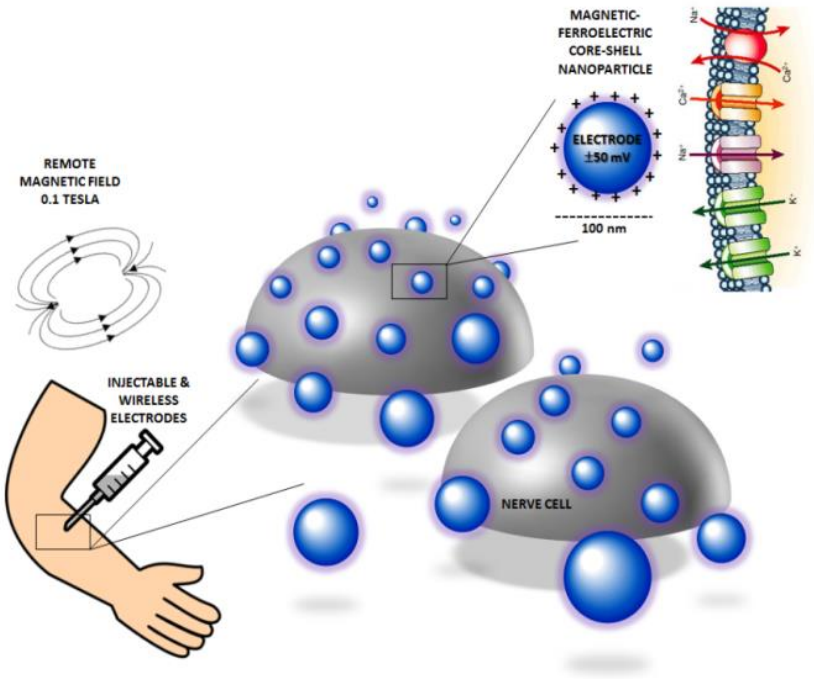

Figure 1.23. ME composite particles, consisting of ferroelectric and ferromagnetic phases, in the form of dispersible, injectable electrodes for targeting electrical stimulation at level of single cells and cell surface molecules.[111]

Motivated by the advances in ME composites, ceramic ME nanocomposites have been explored for biomedical applications such as wireless endoscopy, minimally invasive surgical tools,[112] and stimulation of functions of living cells.[110] The potential use of ME nanoparticles as carriers for on-demand drug release and to artificially stimulate the neural activity deep in the brain has also been suggested.[113,114] A breakthrough was made in targeted anticancer drug delivery where controlled release with $CoFe_2O_4$-$BaTiO_3$ nanoparticles was demonstrated in mice tumor.[115] Paclitaxel (PTX)-loaded ME nanoparticles (MEN) were administrated into the circulatory system through an *in vivo* injection. With the application of a specific dc magnetic

field, the particles were able to accumulate in the tumor region (**Figure 1.24a)**, and internalized by cancer cells (**Figure 1.24b).** As an ac magnetic field (100 Hz, 50 Oe) was turned on, PTX was released in targeted cells with retained anticancer activity.

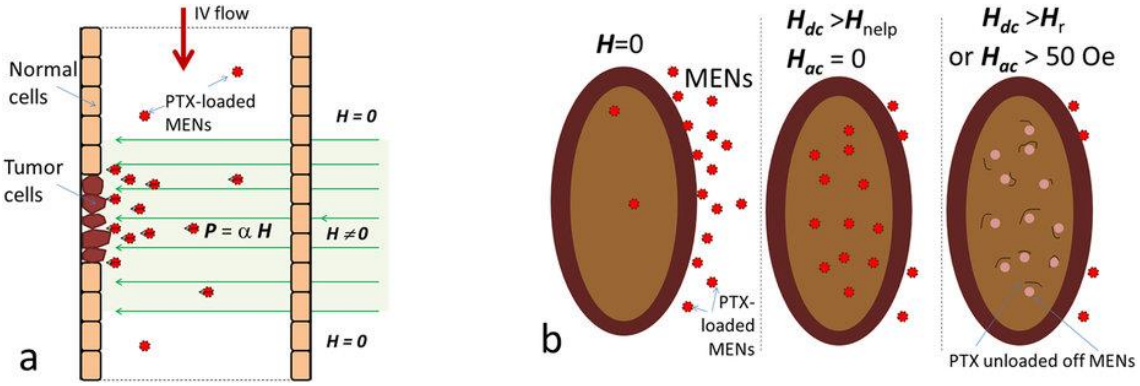

Figure 1.24. Illustration of a field-controlled targeted drug (PTX) delivery by MENs through a capillary.[115]

Very recently, $CoFe_2O_4$–$BaTiO_3$ 30-nm ME nanoparticles (**Figure 1.25a**) have been intravenously administration into the tail vein of mice, followed by their forced movement across the blood-brain barrier and into the brain by applying a dc field gradient of 3000 Oe m^{-1}.[116] A surgically attached two channel electroencephalography headmount was then able to directly measure the modulation of neural brain tissue activity induced by ME stimulation *via* the nanoparticles (**Figure 1.25b**). Low ac magnetic fields of 100 Oe with frequencies ranging from 0-20 Hz were applied, with the modulated signals reaching the strength comparable to that of the regular neural activity. This work is of significance, as it opens a pathway to use multifunctional

nanoparticles to control intrinsic fields deep in the brain, and the concept is further described in **Figure 1.25c**.

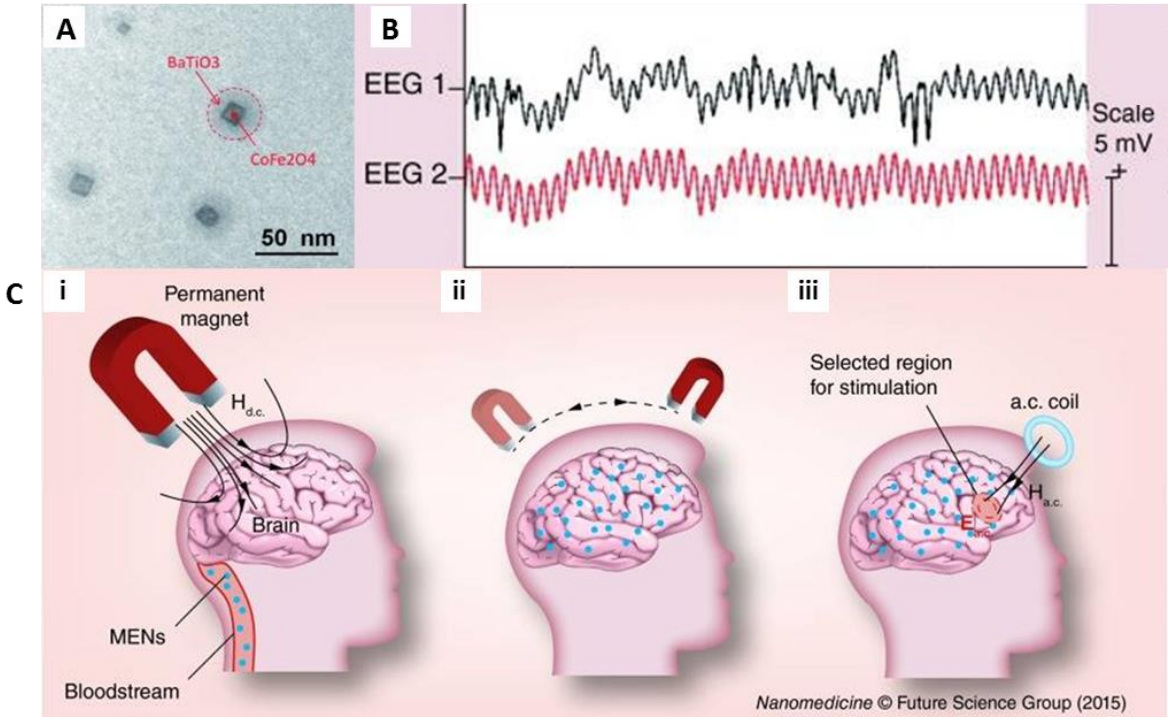

Figure 1.25. (a) TEM Image of core-shell ME nanoparticles (MENs). (b) EEG Waveforms from the two EEG channels with MENs in the brain under exposure to an external 100-Oe ac magnetic field at a frequency of 10 Hz. The vertical scale bar for the waveform signal is 5 mV. (c) Schematic illustration of the novel concept to use MENs for 'mapping' the brain for non-invasive electric field stimulation of selected regions deep in the brain.[116]

In addition to ceramic ME nanoparticles, polymer-based ME composite provides the unique prospect of incorporating PE biopolymers to harness their unexploited electrical properties. A very recent study conducts a novel approach for bone tissue engineering using P(VDF-TrFE)/Terfenol-D ME laminate to stimulate MC3T3-E1

pre-osteoblast cells. A dynamic magnetic field is applied to trigger an electrical field up to 0.115 mV under a dc magnetic field ~250 Oe, and the result indicate cell proliferation is enhanced by approximately 25 % in comparison to the control group of the static magnetic condition (**Figure 1.26**).[117] So far, different types of ME composite, from nanoparticles to laminates, have been employed for cell stimulation. Remote activation of the electrodes, without the need for onboard wireless circuits or power sources, can be performed *via* magnetic fields that are well-established in current FDA approved medical and clinical instrumentation.[111]

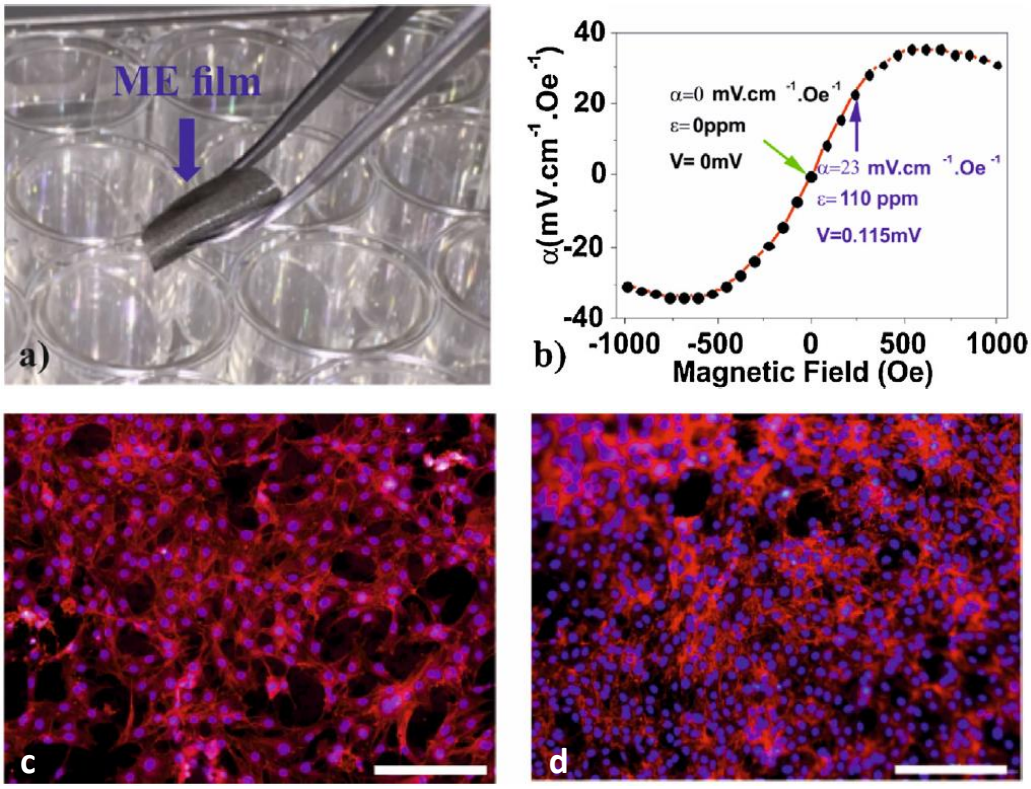

Figure 1.26. (a) P(VDF-TrFE)/Terfenol-D ME laminate. (b) Corresponding ME characterization with (ME coefficient), strain (ε) and voltage (V) values that will be generated during the dynamic cell culture. Representative images of pre-osteoblast culture after 72 h with (c) static and (d) dynamic conditions (nucleus stained with DAPI-blue and cytoskeleton stained with TRITC-red). Scale bar=200 μm.[117]

The above works on cell stimulation have mainly focused on ME composite consisting of PE ceramics or synthetic PE polymers but have not explored the use of PE biopolymers. Employing PE biopolymers in ME composites provides the possibility of fabricating biodegradable and bio-compatible devices for biomedical applications.

1.9. PE Biopolymers

1.9.1. Collagen, Polysaccharide and DNA

The PE effect is a common phenomenon in organic and biological tissues. Since Fukada first described the PE properties of wood,[118] piezoelectricity has been widely observed in various biomaterials, *e.g.* silk, bone and connective tissue.[40,119-121] Generally, most of the PE effects in naturally occurring materials are suggested to be associated with crystalline/semicrystalline bio-macromolecules.

Table 1.4. Distribution of Representatively PE Biopolymers in Nature: (a) Collagen, (b) Polysaccharide.

a

Collagen	Distribution(s)
Type I	Skin, Tendon, Bone
Type IV	Reticulate
Type V	Animal Cell surface, Skin, Placenta

b

Polysaccharide	Distribution(s)
Chitin	Carb, Shrimp
Chitosan	N/A[a]
Cellulose	Plant Cell Wall

Note: a. Chitosan is produced from chitin when the degree of deacetylation of chitin reaches about 50%.[122]

Table 1.5. PE coefficient of some naturally occurring polymers.

	d_{33}	d_{31}	d_{25}	d_{24}
Cellulose Nanocrystal[123]	N/A	N/A	21 pm V^{-1}	N/A
Collagen[124]	0.025 pC N^{-1}	0.033 pC N^{-1}	1 pC N^{-1}	0.525 pC N^{-1}

PE biopolymers are rich in nature and considered as an almost inexhaustible resource in industry. For example, as the main component of connective tissues in animals, collagen is the most abundant protein in mammals.[125] So far approximately 28 different types of collagen have been identified. They are widely distributed in hair, bone, placenta and many other tissues **(Table 1.4a)**, and their piezoelectricity arises from building blocks of polypeptides arranged to form dipole moments (**Figure 1.27a**).[121] In addition to collagen, polysaccharide is another family of biopolymers possessing piezoelectricity. PE polysaccharides include chitin, chitosan and cellulose **(Table 1.4b)** that exist as crystal/semi-crystal structures. These polymers contain dipolar monosaccharide units connected together with 1,4-glycosidic bonding that give rise to their PE properties.[40,122,126] PE effects have also been found in deoxyribonucleic acid (DNA). Oriented DNA films revealed the origin of the PE effect that is attributed to orientation of dipoles in phosphate and deoxyribose containing oxygen and asymmetric carbon atoms (**Figure 1.27b**).[127]

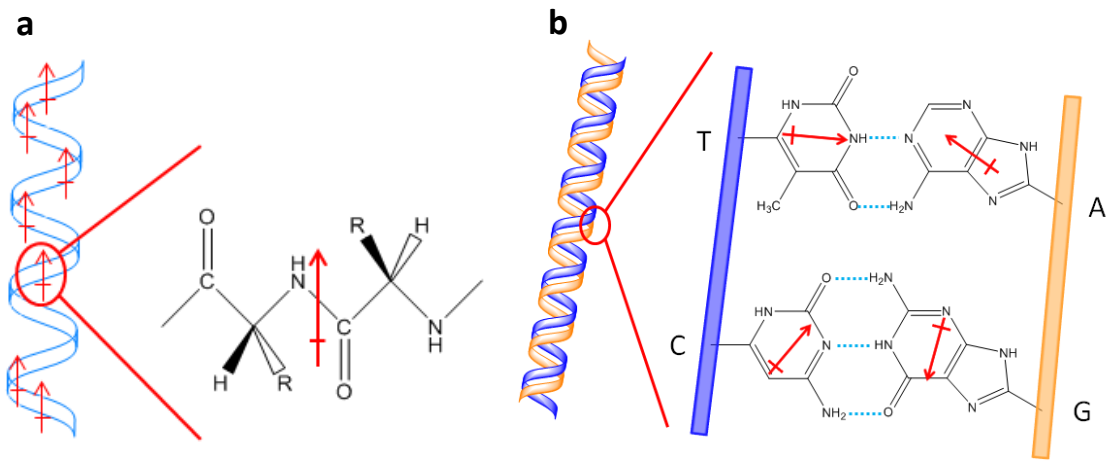

Figure 1.27. Illustration of uniaxially oriented dipole moments in PE biopolymers. (a) collagen and (b) DNA. The red arrows indicate the dipole direction of each moment.

1.9.2. Peptide and Living Organisms for Electronics

PE biopolymer-based PE devices have not been reported until recent years[128-130] , presumably due to their inherently weak PE coefficients that limit the output voltage. An effective way to improve the PE response of biopolymers involves optimizing the molecular orientations by aligning the dipolar moments.[131-133] For example, this was achieved using electronic poling to control the polarization of peptides during their self-assembly into a micro-rod layer, where each micro-rod is polarized at the same direction thus rendering the array good PE property.[129] The self-assembled micro-rod layer could then be fabricated as a power generator with gold coated silicon as electrodes on each side of the surfaces (**Figure 1.28a**). When a mechanical stress was applied vertically to the array layer (**Figure 1.28b**), the open circuit voltage (**Figure**

1.28 c) and the corresponding short-circuit current were measured as 1.4 V and 39.2 nA, respectively.

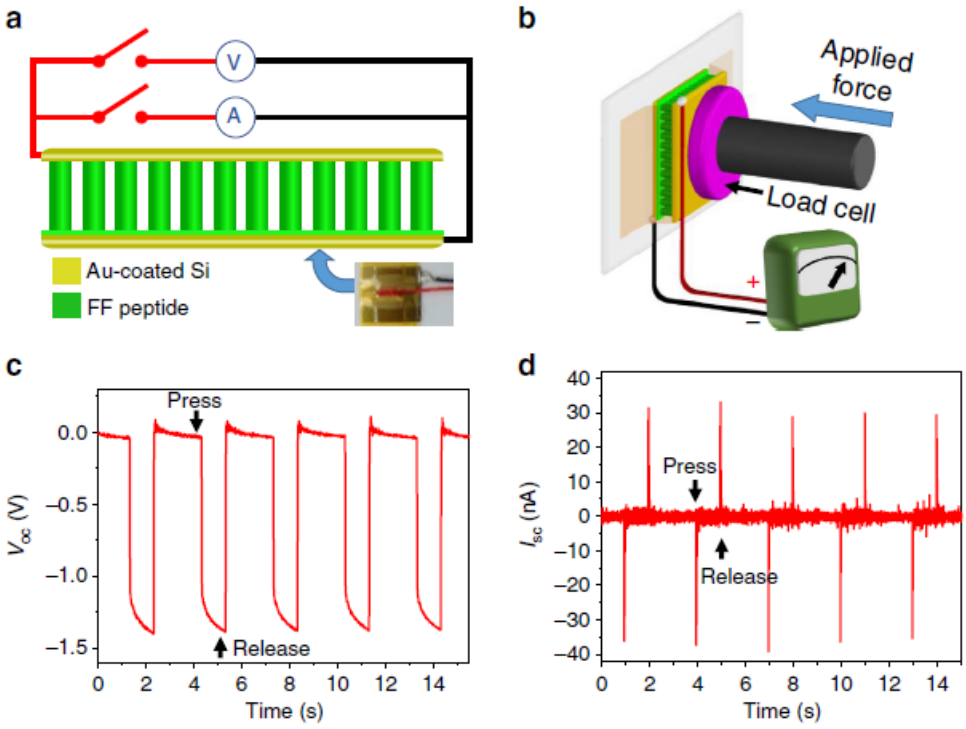

Figure 1.28. Schematic illustration of (a) the peptide based power generator: the peptide rods were grown vertically on a substrate and combined with Au electrodes on the surface and bottom. (b) The measurement set-up in which a linear motor pushes with controlled forces on the top electrode. (c) The open circuit voltage and (d) the short-circuit current conducted from the generator.[129]

The PE effect can be induced at molecular level but also exists in living organisms. Viral particles, for example M13 phages, have been fabricated as functional materials for tissue regeneration, energy storage and generation.[134-137] The piezoelectricity of M13 phage is rendered by its unique external wall structure; each of the phages

(**Figure 1.29a**) are covered by approximately 2700 copies major coat proteins (pVIII) which have an α-helical structure with a dipolar moment directed from the amino- to the carboxy-terminal orientation (**Figure 1.29b–d**). This results in the intrinsic PE properties of M13, as the aligned protein coat structure lacks the inversion symmetry. Individual M13 phages can be assembled either laterally or vertically to produce bio-PE devices that generate energy as high as 0.4 V and 6 nA, which is sufficient for liquid-crystal displays.[128,130]

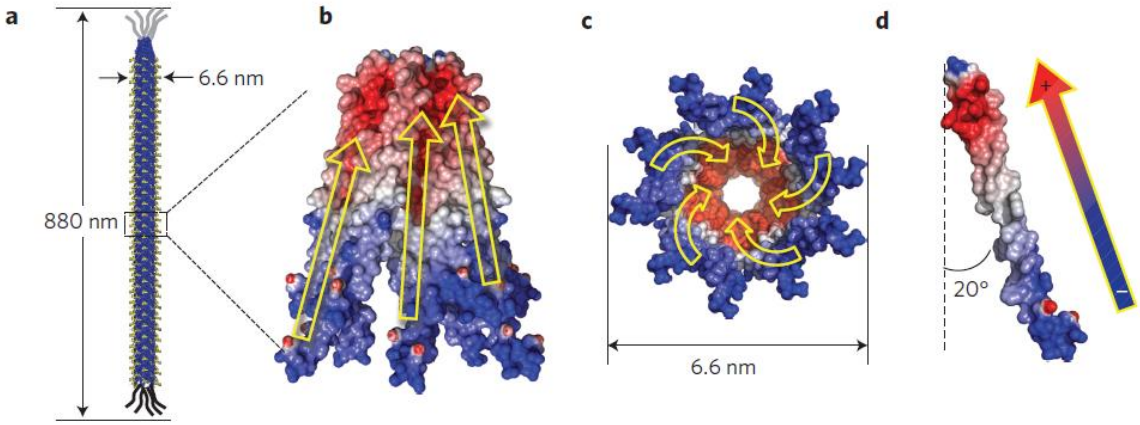

Figure 1.29. Schematic view of (a) rod like M13 pahge; (b) side of M13 phage, the yellow arrow shows the dipolar orientation; (c) cross-sectional view of M13 phage, which is covered by pVIII proteins with five-fold rotational and two-fold screw symmetry; (d) the dipolar moment of pVIII protein, which is generated from the N-terminus (blue) to the C-terminus (red) and has an 20˚ tilt angle with respect to the phage long axis.[128]

Although PE biopolymers are a widely distributed resource (**Table 1.4**), the limitation of using raw biomaterials lies in several aspects. One consideration is the poor

machinability, as most of them are not suitable to be industrially moulded to the desired form. Moreover, PE biopolymers usually co-exist with other constituents, therefore such variations arising from their different sources may hinder their extraction, isolation, refinement, specification and standardization in final products. The latter is particularly important before entering clinical applications. For example, the mechanical properties of wood vary from species to species and are highly depend on environmental parameters, *e.g.* temperature and humidity, and influence the PE effect of woods.[138-140]

1.9.3. Cellulose

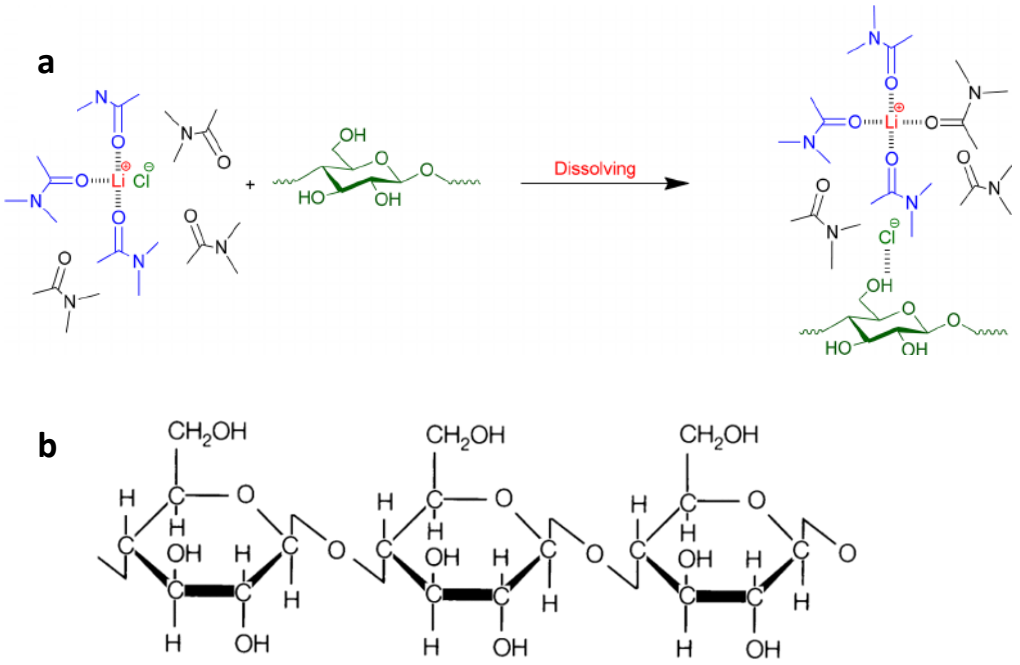

Scheme 1.2. (a) Schematic of the interaction among Li^+ cation, Cl^- anion, and DMAc when cellulose dissolves into the DMAc/LiCl system.[141] (b) Chemical structure of cellulose.

The use of regenerated products brings a supplementary source of PE polymers for different applications. Here, PE polymers can be extracted and purified through dissolution processes and the end-products made suitable for further industrial processes. One example is regenerated cellulose produced from solution processing with N,N-dimethylacetamide (DMAc)/LiCl (**Scheme 1.2a**) and subsequently used to produce 'electroactive' paper (EAPap).[142] The piezoelectricity of cellulose is due to the chemical polarity (-OH and $-CH_2OH$ groups) as well as their non-centrosymmetric structure (**Scheme 1.2b**).[143] Experimentally it was verified that the electric dipole of native cellulose is 4400 ± 400 Debye along the chain axis.[144]

The regenerated cellulose film can undergo mechanical deformation when an external electrical field is applied,[145] and has been configured to make electrical electric devices such as an actuator.[146,147] For example, to test the actuation performance EAPap was stimulated by a gold layer as surface electrode and a thin steel substrate as bottom electrode **(Figure 1.30a)**. Then a stimulating voltage with different frequencies was applied, and the corresponding displacement of the EAPap layers was recorded using a laser detector. It was found that the bias induced displacement shows a linear relationship according to the voltage over a wide range of frequencies, for example between 0.1 and 10 Hz **(Figure 1.30b and c)**. The best performance was observed in a 32-layer EAPap bound device of which the PE coefficient was as high as 150 pm V^{-1}. Such properties are regarded as promising for actuator application.[148] Since the piezoelectricity of cellulose mainly comes from its crystalline structure, the

application of mechanical forces or electrical poling can further increase the degree of crystallinity and enhance the PE properties.[149-151]

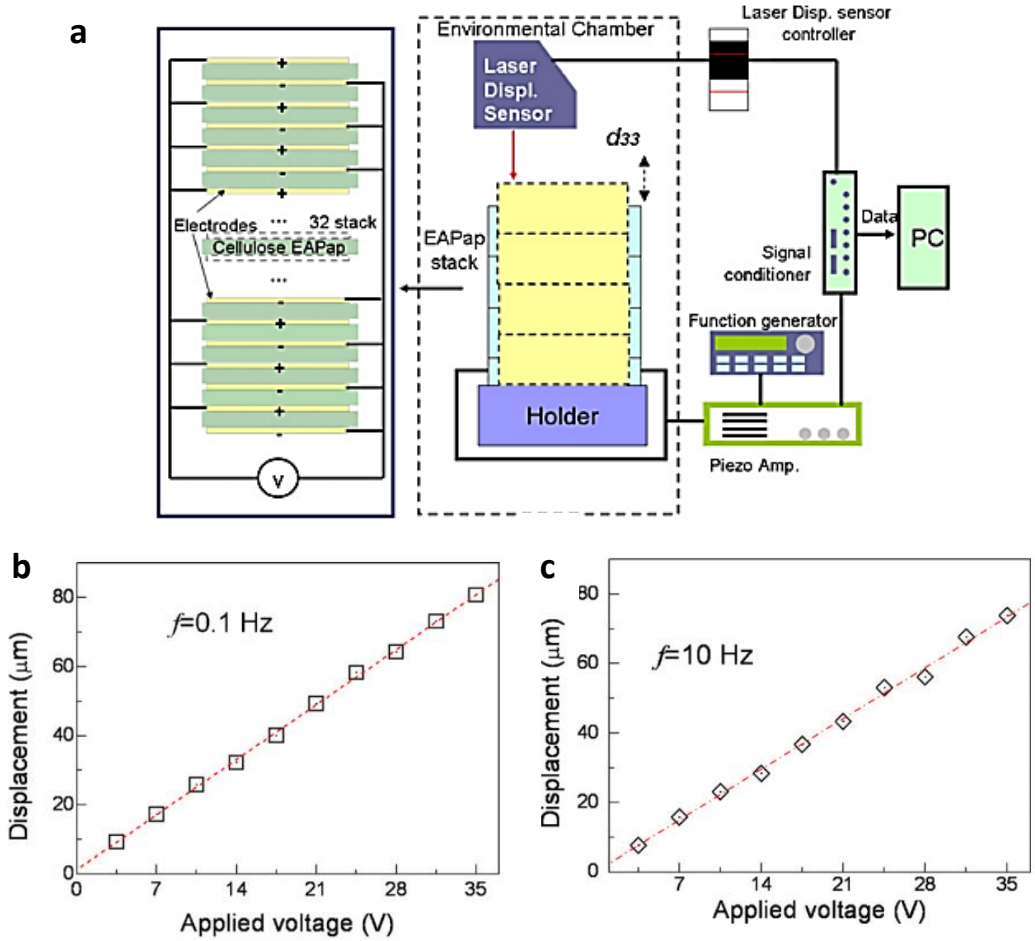

Figure 1.30. (a) Schematic view of stacked EAPap actuator: left part is the configuration of the stacked cellulose EAPap actuator and the right shows its performance test setup. (b,c) Bending displacement as a function of applied voltage at the frequencies of (b) f = 0.1 Hz and (c) f = 10 Hz.[148]

Besides regenerated cellulose, its highly purified form, cellulose nanocrystal (CNC), has generated significant interest due to its unique chemical, mechanical, optical, and

rheological properties.[152-157] CNC is primarily obtained from natural raw materials such as plants, algae, bacteria, and some sea animals.[158,159] Naturally occurring cellulose consists of ordered, highly crystalline domains along with disordered amorphous regions (**Figure 1.31a**) with different proportions.[160] The extraction of CNC from natural fibers involves acid hydrolysis to decompose the amorphous section and the formed CNC show a rod-like structure (**Figure 1.31b**) with high crystallinity degree. Compare to regenerated cellulose, the polymer chains in CNC maintain the well aligned structure before acid hydrolysis. This configuration is preferred to induce piezoelectricity and a considerable PE response at the nanoscopic level has been reported.[123]

As a very cheap, renewable, easily processable and degradable substrate, cellulose is developing rapidly as a supporting substrate for flexible and transparent electronics,[161,162] and is expected to have wider impact in biomedical applications. Hence, exploring novel ME composites based on naturally occurring PE biopolymers is of significant interest.

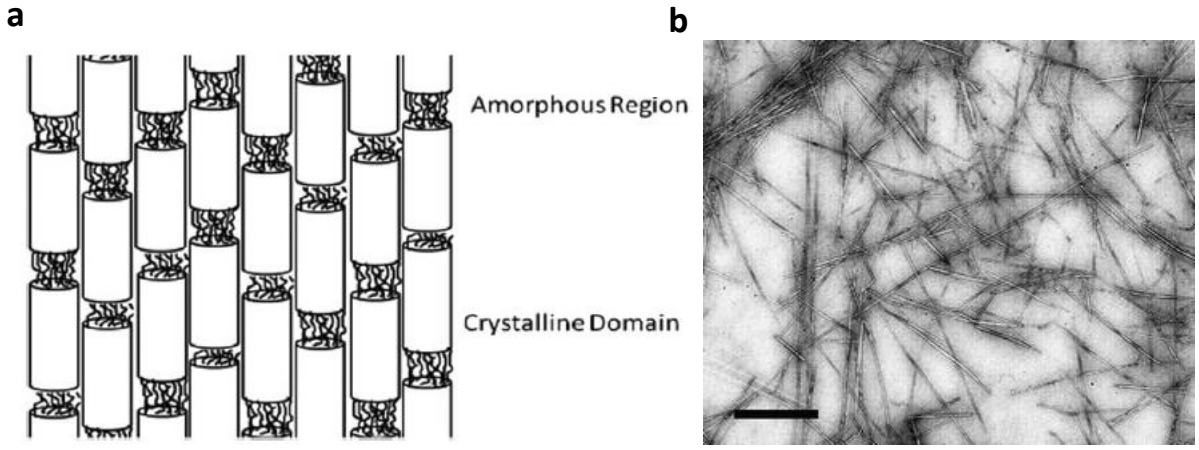

Figure 1.31. (a) Schematic view of crystalline and amorphous domains in naturally occurring cellulose.[163] (b) TEM image of CNC (scale bar=1 μm).[164]

1.10. Nanoscale Piezoelectricty & Piezoresponse Force Microscopy (PFM)

1.10.1. Basic Principles of PFM

For studying the PE effect, understanding the dynamics of the dielectric polarization process is mostly desired. This requires lateral nanoscale resolution to study local displacement on PE materials, which cannot be achieved using traditional bulk measurement methods such as a d_{33} meter.[118] By using scanning probe microscopy, specifically the technique of PFM, it is possible to elucidate the local, nanoscale lateral variation in the PE response combined with the PFM switching spectroscopy (PFM-SS) mode that has the ability to detect picometer displacements in response to

an applied voltage bias. The local displacement according to hysteresis loops of the phase response can reveal the dynamic process of polarization switching of dipolar moments.

PFM was first demonstrated by Guthner and Dransfeld to investigate poled domains on a ferroelectric polymer film.[165] Briefly, PE materials are bulk crystals consisting of several domains. In a PE material dipoles near each other tend to be aligned in regions called PE/Weiss domains (**Figure 1.32a**). Between the PE domains there exists a domain wall, referred to as a domain boundary. PFM is an effective technique to reveal the domains of PE materials by inducing local displacement towards different domain orientations. To perform the PFM measurements, a biased conductive tip is brought into contact with the sample surface while scanning and the PE response is measured as the first-harmonic of cantilever deflection:[166]

$$d = d_0 + A\cos(\omega t + \varphi) \qquad (1.7)$$

where d_0 is the equilibrium position of the tip; A is the amplitude and ω is the frequency of applied bias; φ is the phase yielded information on the polarization direction below the tip (**Figure 1.32b**).[167] The feedback signal corresponding to the PE response and polarization direction(s) are recorded in the amplitude and phase channels (**Figure 1.32c**), respectively.

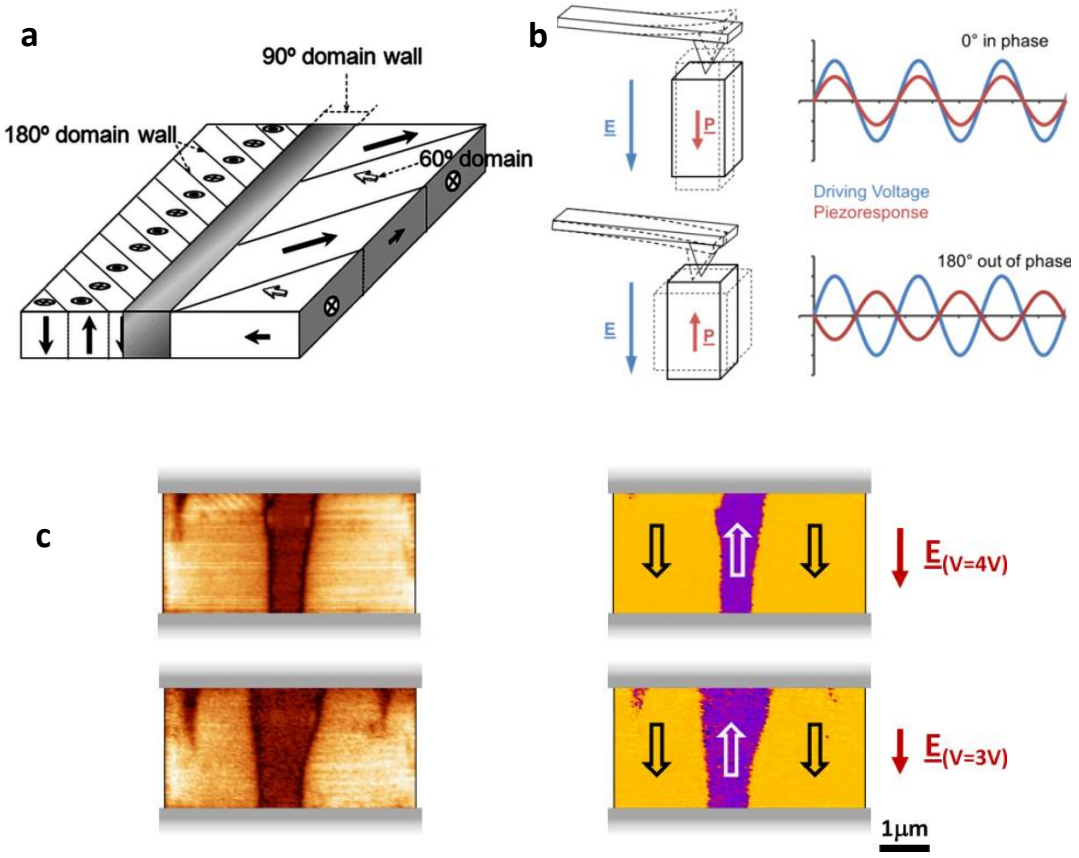

Figure 1.32. (a) Schematic illustration of 3D domain structure.[168] (b) Polarization direction resulted in phase (upper) and out of phase (bottom) piezoresponse detected by PFM (©Wikipedia).[167] (c) PFM amplitude (left) and phase (right) images of a $BaTiO_3$ as the bias field is progressively changed to induce reversal of polarization.[169]

1.10.2. Dual AC Resonance Tracking (DART) Mode

Since PFM scanning is operated in contact mode and the first harmonic (resonance frequency) is often used to enhance the small displacements, there is a problem known as mechanical crosstalk and this effect occurs when the scanning tip approaches the edge of a protrusion. For example, this causes tilting or lifting of AFM tip that convolutes the actual PE-induced displacement in the sample, changing the

resonance frequency and consequently leads to an error in feedback signal, as shown in **Figure 1.33a and b**. To overcome this, a dual AC resonance tracking (DART) technique was introduced whereby the amplitude and phase signals are monitored at two frequencies either higher or lower than the resonance frequency. The cantilever deflection was digitized and sent to two separated lock-in amplifiers, each referenced to one of the driving frequencies.[170] By measuring the change in amplitude at two different frequencies, it is possible to track the resonance frequency change caused by the crosstalk effect and eliminate the error, and therefore overcome the crosstalk effect and provide a quantitative description of the PE response. DART mode PFM provides the possibility for studying the local PE response of "non-flat" samples, which is extremely useful for natural biopolymers such as collagen fibrils (**Figure 1.33c-e**) or cell surfaces/interfaces with globular morphology.[166] The sensitivity of PFM image is related to the PE type of the materials and the orientation of the crystalline direction. For example, the aligned CNC nanowhiskers show a response approximately 45˚ in a band form according to the axial direction of nanowhiskers.[123]

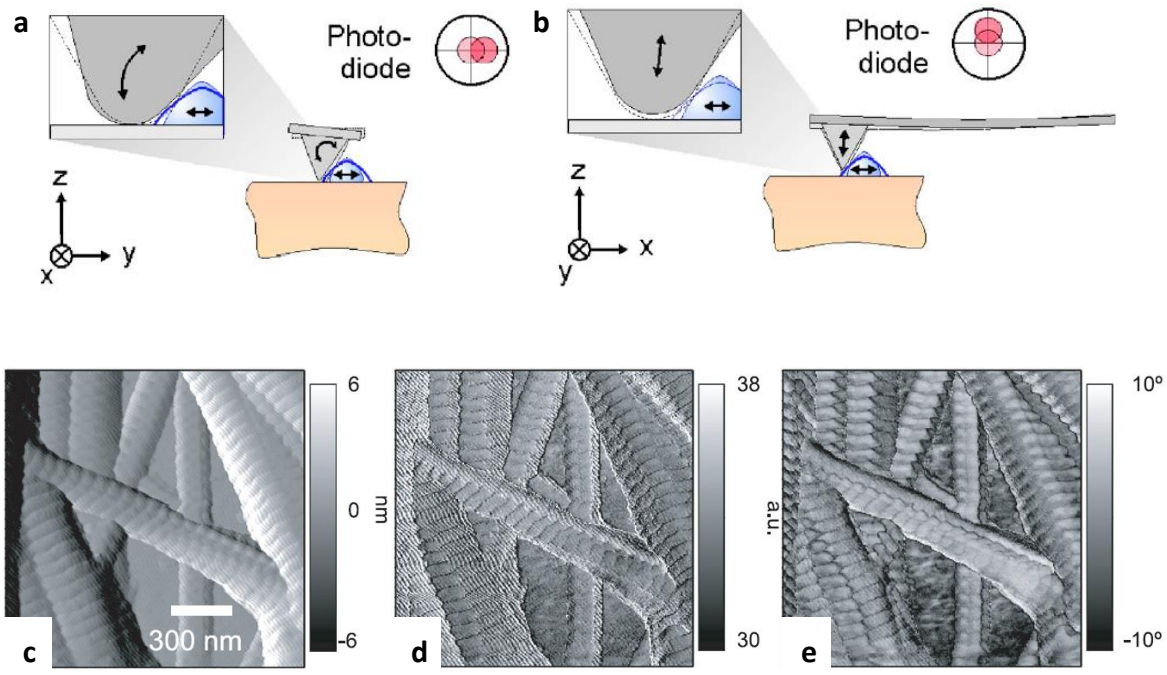

Figure 1.33. Schematic illustration of mechanical crosstalk effect when expansion of dipolar grain causes (a) tilting and (b) lifting of tip at the cantilever resonance frequency in contact mode. PFM images of mouse tail collagen in (c) topography, (d) amplitude and (e) phase channels.[170]

1.10.3. Switching Spectroscopy PFM (SS-PFM)

The switching spectroscopy PFM (SS-PFM) is a powerful tool to reveal the dynamic process of dipolarization by quantitatively study the local switching behaviour, including imprint voltages, coercive bias, and saturation responses.[171] During SS-PFM measurement, the conductive tip is brought into contact with a ferroelectric sample and a sequence of high (dc on) and low (dc off) dc voltages combined with a relatively small ac voltage are applied to induce the PE response (**Figure 1.14a**). The

corresponding hysteresis loops are obtained at the cantilever resonance frequency and yield both displacement and phase changes according to the real-time voltage in off-state of dc bias.[172] The hysteresis loops is associated with the displacement induced by the cyclic bias from the conductive tip, which is essentially related to the electromechanical property of PE materials, and some other factor such as surface charge can influence the shape of the hysteresis loop.[172] These hysteresis loops are employed for further analysis of the local switching behaviour and determine if a material possess piezo-responsive properties. If the phase loop shows a ~180˚ change and a butterfly shape is observed is the amplitude loop (**Figure 1.34b, c**), the behaviour is then regarded as a PE response which corresponds to the dipolarization process of a PE material. While the displacement loop displays a butterfly shape (**Figure 1.34c**), in which the two lowest points A and B, are correspond to the positions in the phase loops where the switching from ~0-180˚ begins. The voltages corresponding to the two lowest displacement points (A and B in **Figure 1.34c**) are the upper and bottom limits of the coercive bias, and the voltage corresponding to the highest displacement is known as the saturation response.

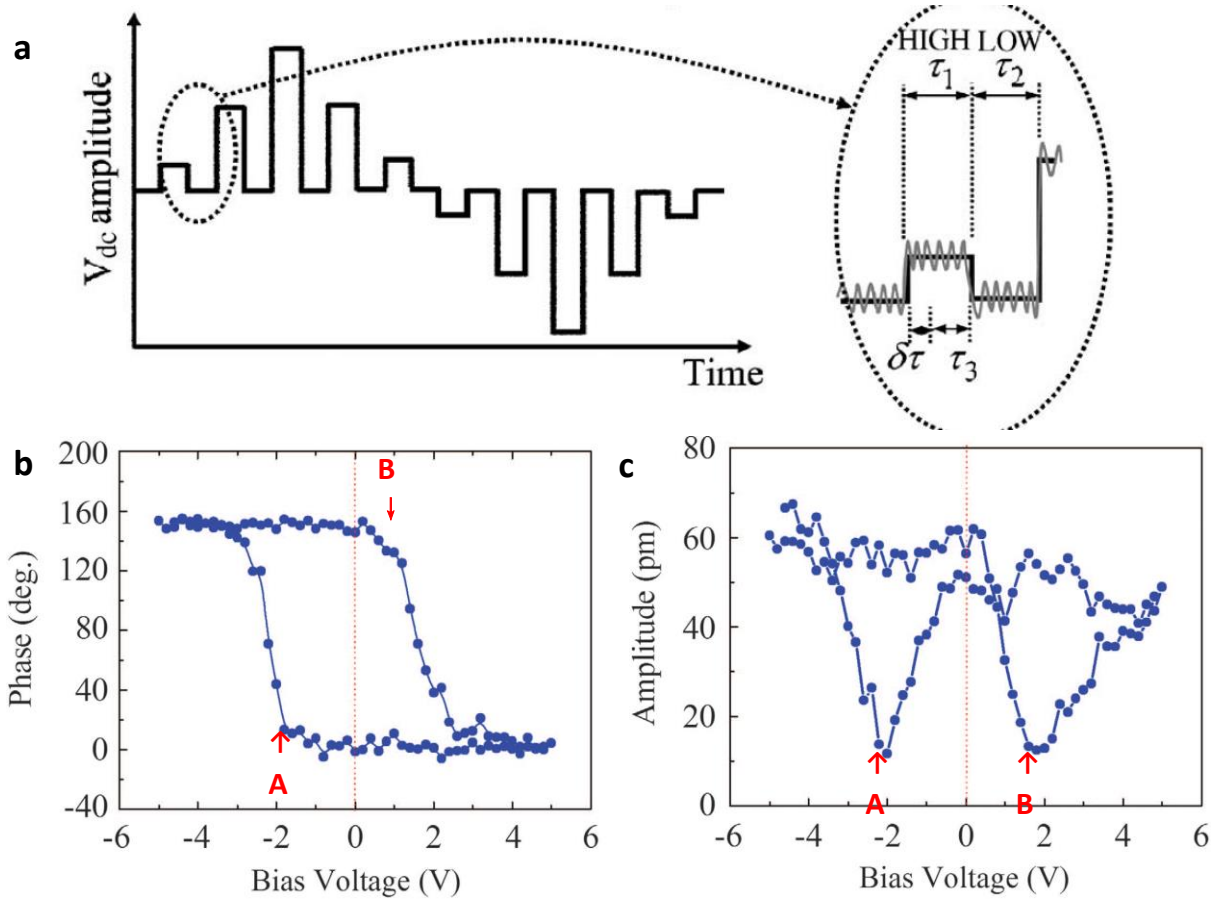

Figure 1.34. (a) The wave form of stimulating bias applied by SS-PFM.[172] The (b) phase and (c) amplitude/displacement butterfly hysteresis loops of a PE $YMnO_3$ film.[173] The hysteresis loops are obtained on off state when no dc bias is applied.

Note

Part of the text in **Chapter 1.** is published in a book chapter with citation as below:

Zheng, T.; **Zong, Y.**; Yue, Z.; Wallace, G. G.; Higgins, M. J. *Magnetoelectric Composites for Bionics Applications* in Magnetoelectric Polymer-Based Composites; Wiley-VCH Verlag GmbH & Co. KGaA: **2017**, p 171.

1.11. References

1 Ryu, J. *et al.* Ubiquitous magneto-mechano-electric generator. *Energy Environ. Sci.* **8**, 2402-2408, (2015).

2 Israel, C., Mathur, N. D. & Scott, J. F. A one-cent room-temperature magnetoelectric sensor. *Nat Mater* **7**, 93-94, (2008).

3 Heron, J. T. *et al.* Deterministic switching of ferromagnetism at room temperature using an electric field. *Nature* **516**, 370-373, (2014).

4 Spaldin, N. A. & Fiebig, M. The Renaissance of Magnetoelectric Multiferroics. *Science* **309**, 391-392, (2005).

5 Landau, L. D. *et al. Electrodynamics of continuous media*. Vol. 8 (elsevier, 1984).

6 Eerenstein, W., Mathur, N. D. & Scott, J. F. Multiferroic and magnetoelectric materials. *Nature* **442**, 759-765, (2006).

7 Astrov, D. Vol. 11 708-709 (AMER INST PHYSICS CIRCULATION FULFILLMENT DIV, 500 SUNNYSIDE BLVD, WOODBURY, NY 11797-2999, 1960).

8 Hill, N. A. Why Are There so Few Magnetic Ferroelectrics? *The Journal of Physical Chemistry B* **104**, 6694-6709, (2000).

9 Kimura, T. *et al.* Magnetic control of ferroelectric polarization. *Nature* **426**, 55-58, (2003).

10 Catalan, G. & Scott, J. F. Physics and Applications of Bismuth Ferrite. *Adv. Mater.* **21**, 2463-2485, (2009).

11 Lotey, G. S. & Verma, N. K. Magnetoelectric coupling in multiferroic BiFeO3 nanowires. *Chem. Phys. Lett.* **579**, 78-84, (2013).

12 Mundy, J. A. *et al.* Atomically engineered ferroic layers yield a room-temperature magnetoelectric multiferroic. *Nature* **537**, 523, (2016).

13 Kitagawa, Y. *et al.* Low-field magnetoelectric effect at room temperature. *Nat Mater* **9**, 797-802, (2010).

14 Matsubara, M. *et al.* Magnetoelectric domain control in multiferroic TbMnO₃. *Science* **348**, 1112-1115, (2015).

15 Suchtelen, J. v. *Philips Res. Rep.* **27**, 28-37, (1972).

16 Nan, C. W. MAGNETOELECTRIC EFFECT IN COMPOSITES OF PIEZOELECTRIC AND PIEZOMAGNETIC PHASES. *Physical Review B* **50**, 6082-6088, (1994).

17 Wang, Y., Hu, J., Lin, Y. & Nan, C.-W. Multiferroic magnetoelectric composite nanostructures. *NPG Asia Mater* **2**, 61-68, (2010).

18 Jayasimha, A. & Alison, B. F. A review of magnetostrictive iron–gallium alloys. *Smart Mater. Struct.* **20**, 043001, (2011).

19 Du Trémolet de Lacheisserie, E. & Peuzin, J. C. Magnetostriction and internal stresses in thin films: the cantilever method revisited. *J. Magn. Magn. Mater.* **136**, 189-196, (1994).
20 Jiles, D. C. Theory of the magnetomechanical effect. *J. Phys. D: Appl. Phys.* **28**, 1537, (1995).
21 Villari, E. Ueber die Aenderungen des magnetischen Moments, welche der Zug und das Hindurchleiten eines galvanischen Stroms in einem Stabe von Stahl oder Eisen hervorbringen. *Annalen der Physik* **202**, 87-122, (1865).
22 Kim, Y. Y. & Kwon, Y. E. Review of magnetostrictive patch transducers and applications in ultrasonic nondestructive testing of waveguides. *Ultrasonics* **62**, 3-19, (2015).
23 Wohlfarth, E. P. *Ferromagnetic Materials: A Handbook on the Properties of Magnetically Ordered Substances*. (North-Holland, 1980).
24 J. Dapino, M. *On magnetostrictive materials and their use in adaptive structures*. Vol. 17 (2004).
25 Clark, A. E., DeSavage, B. F. & Bozorth, R. Anomalous Thermal Expansion and Magnetostriction of Single-Crystal Dysprosium. *Phys. Rev.* **138**, A216-A224, (1965).
26 Engdahl, G. & Mayergoyz, I. D. *Handbook of Giant Magnetostrictive Materials*. (Elsevier Science, 1999).
27 Cady, W. G. *Piezoelectricity: an introduction to the theory and applications of electromechanical phenomena in crystals*. (Dover Publications, 1964).
28 Kokkinopoulos, A., Vokas, G. & Papageorgas, P. Energy Harvesting Implementing Embedded Piezoelectric Generators – The Potential for the Attiki Odos Traffic Grid. *Energy Procedia* **50**, 1070-1085, (2014).
29 Fukada, E. History and recent progress in piezoelectric polymers. *IEEE Trans. Ultrason., Ferroelect., Freq. Control.* **47**, 1277-1290, (2000).
30 Mazurek, B., Różecki, S., Kowalczyk, D. & Janiczek, T. Influence of piezoelectric cable processing steps on PVDF beta phase content. *J. Electrostatics* **51-52**, 180-185, (2001).
31 Khaled, S. R., Sameoto, D. & Evoy, S. A review of piezoelectric polymers as functional materials for electromechanical transducers. *Smart Mater. Struct.* **23**, 033001, (2014).
32 Katsouras, I. *et al.* The negative piezoelectric effect of the ferroelectric polymer poly(vinylidene fluoride). *Nat Mater* **15**, 78-84, (2016).
33 Wietzke, S. *et al.* Thermomorphological study of the terahertz lattice modes in polyvinylidene fluoride and high-density polyethylene. *Appl. Phys. Lett.* **97**, 022901, (2010).
34 Martins, P., Lopes, A. C. & Lanceros-Mendez, S. Electroactive phases of poly(vinylidene fluoride): Determination, processing and applications. *Progress in Polymer Science* **39**, 683-706, (2014).
35 Jaffe, B. *Piezoelectric Ceramics*. (Elsevier Science, 2012).

36 Roberts, S. Dielectric and Piezoelectric Properties of Barium Titanate. *Phys. Rev.* **71**, 890-895, (1947).
37 Shubnikov, A. Piezoelectric textures. *Izd. Akad. Nauk USSR, Moskva*, (1946).
38 Nye, J. F. *Physical properties of crystals: their representation by tensors and matrices*. (Oxford university press, 1985).
39 Lang, S. B. Pyroelectric Effect in Bone and Tendon. *Nature* **212**, 704-705, (1966).
40 Fukada, E. Piezoelectric properties of biological polymers. *Quarterly Reviews of Biophysics* **16**, 59-87, (1983).
41 Furukawa, T. Piezoelectricity and pyroelectricity in polymers. *IEEE Transactions on Electrical Insulation* **24**, 375-394, (1989).
42 Scheinbeim, J. I. & Gao, Q. (Google Patents, 2002).
43 Singh, R. S., Bhimasankaram, T., Kumar, G. S. & Suryanarayana, S. V. DIELECTRIC AND MAGNETOELECTRIC PROPERTIES OF BI5FETI3O15. *Solid State Communications* **91**, 567-569, (1994).
44 Rivera, J. P. On definitions, units, measurements, tensor forms of the linear magnetoelectric effect and on a new dynamic method applied to Cr-Cl boracite. *Ferroelectrics* **161**, 165, (1994).
45 Duong, G. V., Groessinger, R., Schoenhart, M. & Bueno-Basques, D. The lock-in technique for studying magnetoelectric effect. *Journal of Magnetism and Magnetic Materials* **316**, 390-393, (2007).
46 Dinesh Kumar, S., Ramesh, G. & Subramanian, V. Enhanced self-biased direct and converse magnetoelectric effect in Pb(In1/2Nb1/2)O3–PbTiO3/NiFe2O4 bi-layer laminate composite. *Journal of Materials Science: Materials in Electronics* **26**, 2682-2687, (2015).
47 Reis, S. *et al.* Electronic optimization for an energy harvesting system based on magnetoelectric Metglas/poly(vinylidene fluoride)/Metglas composites. *Smart Mater. Struct.* **25**, 085028, (2016).
48 Jin, J. *et al.* Multiferroic Polymer Composites with Greatly Enhanced Magnetoelectric Effect under a Low Magnetic Bias. *Advanced Materials* **23**, 3853-+, (2011).
49 Srinivasan, G. Magnetoelectric Composites. *Annu. Rev. Mater. Res.* **40**, 153-178, (2010).
50 Zhai, J., Xing, Z., Dong, S., Li, J. & Viehland, D. Magnetoelectric Laminate Composites: An Overview. *J. Am. Ceram. Soc.* **91**, 351-358, (2008).
51 Ma, J., Hu, J., Li, Z. & Nan, C.-W. Recent Progress in Multiferroic Magnetoelectric Composites: from Bulk to Thin Films. *Adv. Mater.* **23**, 1062-1087, (2011).
52 Srinivasan, G., DeVreugd, C. P., Flattery, C. S., Laletsin, V. M. & Paddubnaya, N. Magnetoelectric interactions in hot-pressed nickel zinc ferrite and lead zirconante titanate composites. *Applied Physics Letters* **85**, 2550-2552, (2004).

53 Agrawal, S. *et al.* Magnetoelectric properties of microwave sintered particulate composites. *Materials Letters* **63**, 2198-2200, (2009).

54 Jiang, Q. H., Shen, Z. J., Zhou, J. P., Shi, Z. & Nan, C.-W. Magnetoelectric composites of nickel ferrite and lead zirconnate titanate prepared by spark plasma sintering. *Journal of the European Ceramic Society* **27**, 279-284, (2007).

55 Zhou, J.-p., He, H.-c., Shi, Z., Liu, G. & Nan, C.-W. Dielectric, magnetic, and magnetoelectric properties of laminated PbZr0.52Ti0.48O3/CoFe2O4 composite ceramics. *Journal of Applied Physics* **100**, (2006).

56 Islam, R. A., Ni, Y., Khachaturyan, A. G. & Priya, S. Giant magnetoelectric effect in sintered multilayered composite structures. *J. Appl. Phys.* **104**, 044103, (2008).

57 Wang, J., Zhang, Y., Ma, J., Lin, Y. & Nan, C. W. Magnetoelectric behavior of BaTiO(3) films directly grown on CoFe(2)O(4) ceramics. *Journal of Applied Physics* **104**, (2008).

58 Wang, J. *et al.* Substrate Effect on the Magnetoelectric Behavior of Pb(Zr0.52Ti0.48)O-3 Film-On-CoFe2O4 Bulk Ceramic Composites Prepared by Direct Solution Spin Coating. *Journal of the American Ceramic Society* **92**, 2654-2660, (2009).

59 Zheng, H. *et al.* Multiferroic BaTiO3-CoFe2O4 nanostructures. *Science* **303**, 661-663, (2004).

60 Zheng, H. *et al.* Three-dimensional heteroepitaxy in self-assembled BaTiO3-CoFe2O4 nanostructures. *Applied Physics Letters* **85**, 2035-2037, (2004).

61 Zhang, Y., Deng, C., Ma, J., Lin, Y. & Nan, C.-W. Enhancement in magnetoelectric response in CoFe2O4–BaTiO3 heterostructure. *Appl. Phys. Lett.* **92**, 062911, (2008).

62 Nan, C. W., Li, M. & Huang, J. H. Calculations of giant magnetoelectric effects in ferroic composites of rare-earth\char21{}iron alloys and ferroelectric polymers. *Phys. Rev. B* **63**, 144415, (2001).

63 Ryu, J., Priya, S., Carazo, A. V., Uchino, K. & Kim, H.-E. Effect of the Magnetostrictive Layer on Magnetoelectric Properties in Lead Zirconate Titanate/Terfenol-D Laminate Composites. *J. Am. Ceram. Soc.* **84**, 2905-2908, (2001).

64 Dong, S., Cheng, J., Li, J. F. & Viehland, D. Enhanced magnetoelectric effects in laminate composites of Terfenol-D/Pb(Zr,Ti)O3 under resonant drive. *Appl. Phys. Lett.* **83**, 4812-4814, (2003).

65 Zhai, J., Xing, Z., Dong, S., Li, J. & Viehland, D. Detection of pico-Tesla magnetic fields using magneto-electric sensors at room temperature. *Appl. Phys. Lett.* **88**, 062510, (2006).

66 Dai, X., Wen, Y., Li, P., Yang, J. & Zhang, G. Modeling, characterization and fabrication of vibration energy harvester using Terfenol-D/PZT/Terfenol-D

composite transducer. *Sensors and Actuators A: Physical* **156**, 350-358, (2009).

67 Xuan, H. C. *et al.* Large converse magnetoelectric effect in ferromagnetic shape memory alloy Ni49Fe18Ga27Co6 and Pb(Zr0.52Ti0.48)O3 laminates. *Journal of Alloys and Compounds* **519**, 97-100, (2012).

68 Jia, Y., Luo, H., Zhao, X. & Wang, F. Giant Magnetoelectric Response from a Piezoelectric/Magnetostrictive Laminated Composite Combined with a Piezoelectric Transformer. *Adv. Mater.* **20**, 4776-4779, (2008).

69 Grössinger, R., Turtelli, R. S. & Mehmood, N. Materials with high magnetostriction. *IOP Conference Series: Materials Science and Engineering* **60**, 012002, (2014).

70 Sandlund, L. *et al.* Magnetostriction, elastic moduli, and coupling factors of composite Terfenol-D. *J. Appl. Phys.* **75**, 5656-5658, (1994).

71 Liebermann, H. H. & Graham, C. D. Production of amorphous alloy ribbons and effects of apparatus parameters on ribbon dimensions. *Magnetics, IEEE Transactions on* **12**, 921-923, (1976).

72 Zhai, J., Dong, S., Xing, Z., Li, J. & Viehland, D. Giant magnetoelectric effect in Metglas/polyvinylidene-fluoride laminates. (2006).

73 Dong, S., Zhai, J., Li, J. & Viehland, D. Near-ideal magnetoelectricity in high-permeability magnetostrictive/piezofiber laminates with a (2-1) connectivity. *Appl. Phys. Lett.* **89**, 252904, (2006).

74 Zhai, J., Dong, S., Xing, Z., Li, J. & Viehland, D. Giant magnetoelectric effect in Metglas/polyvinylidene-fluoride laminates. *Appl. Phys. Lett.* **89**, 083507, (2006).

75 Wang, Y. *et al.* Equivalent magnetic noise in magnetoelectric Metglas/Pb(Mg1/3Nb2/3)O3-PbTiO3 laminate composites. *physica status solidi (RRL) – Rapid Research Letters* **5**, 232-234, (2011).

76 Li, M., Wang, Y., Gao, J., Li, J. & Viehland, D. Enhanced magnetoelectric effect in self-stressed multi-push-pull mode Metglas/Pb(Zr,Ti)O3/Metglas laminates. *Appl. Phys. Lett.* **101**, 022908, (2012).

77 Zhai, J., Dong, S., Xing, Z., Li, J. & Viehland, D. Geomagnetic sensor based on giant magnetoelectric effect. *Appl. Phys. Lett.* **91**, 123513, (2007).

78 Fang, Z. *Ultra sensitive magnetic sensors integrating the giant magnetoelectric effect with advanced microelectronics*. (2011).

79 Martins, P. & Lanceros-Méndez, S. Polymer-Based Magnetoelectric Materials. *Adv. Funct. Mater.* **23**, 3371-3385, (2013).

80 Zhang, J. X. *et al.* The effect of magnetic nanoparticles on the morphology, ferroelectric, and magnetoelectric behaviors of CFO/P(VDF-TrFE) 0–3 nanocomposites. *J. Appl. Phys.* **105**, 054102, (2009).

81 Guo, Y. *et al.* Giant Magnetodielectric Effect in 0−3 Ni0.5Zn0.5Fe2O4-Poly(vinylidene-fluoride) Nanocomposite Films. *The Journal of Physical Chemistry C* **114**, 13861-13866, (2010).

82 Nan, C. W. *et al.* A three-phase magnetoelectric composite of piezoelectric ceramics, rare-earth iron alloys, and polymer. *Applied Physics Letters* **81**, 3831-3833, (2002).

83 Hilding, J., Grulke, E. A., Zhang, Z. G. & Lockwood, F. Dispersion of carbon nanotubes in liquids. *Journal of Dispersion Science and Technology* **24**, 1-41, (2003).

84 Pyun, J. Nanocomposite materials from functional polymers and magnetic colloids. *Polymer Reviews* **47**, 231-263, (2007).

85 Jin, J. *et al.* Multiferroic Polymer Laminate Composites Exhibiting High Magnetoelectric Response Induced by Hydrogen-Bonding Interactions. *Adv. Funct. Mater.* **24**, 1067-1073, (2014).

86 Ortega, N., Ashok, K., Scott, J. F. & Ram, S. K. Multifunctional magnetoelectric materials for device applications. *J. Phys.: Condens. Matter* **27**, 504002, (2015).

87 Reis, S., Silva, M., Martins, P. & Lanceros-Méndez, S. *Applications of Polymer-Based Magnetoelectric Materials: Fundamentals and Applications*. (2017).

88 Ortega, N., Kumar, A., Scott, J. F. & Katiyar, R. S. Multifunctional Magnetoelectric Materials for Device Applications. *Journal of Physics: Condensed Matter* **27**, 504002-504002, (2015).

89 Wang, Y. *et al.* An Extremely Low Equivalent Magnetic Noise Magnetoelectric Sensor. *Adv. Mater.* **23**, 4111-4114, (2011).

90 Bichurin, M. I. *et al.* Magnetoelectric Sensor of Magnetic Field. *Ferroelectrics* **280**, 199-202, (2002).

91 Giang, D. T. H. & Duc, N. H. Magnetoelectric sensor for microtesla magnetic-fields based on (Fe80Co20)78Si12B10/PZT laminates. *Sensors and Actuators A: Physical* **149**, 229-232, (2009).

92 Fang, Z., Mokhariwale, N., Li, F., Datta, S. & Zhang, Q. M. Magnetoelectric Sensors With Directly Integrated Charge Sensitive Readout Circuit—Improved Field Sensitivity and Signal-to-Noise Ratio. *IEEE Sens. J.* **11**, 2260-2265, (2011).

93 Dong, X. W., Wang, B., Wang, K. F., Wan, J. G. & Liu, J. M. Ultra-sensitive detection of magnetic field and its direction using bilayer PVDF/Metglas laminate. *Sensors and Actuators A: Physical* **153**, 64-68, (2009).

94 Reis, S. *et al.* Fabrication and Characterization of High-Performance Polymer-Based Magnetoelectric DC Magnetic Field Sensors Devices. *IEEE Transactions on Industrial Electronics* **64**, 4928-4934, (2017).

95 Busatto, G., La Capruccia, R., Iannuzzo, F., Velardi, F. & Roncella, R. MAGFET based current sensing for power integrated circuit. *Microelectronics Reliability* **43**, 577-583, (2003).

96 Bai, J. G., Lu, G.-Q. & Lin, T. Magneto-optical current sensing for applications in integrated power electronics modules. *Sensors and Actuators A: Physical* **109**, 9-16, (2003).

97 Senapati, K., Chakrabarty, S., Sahoo, L. K. & Budhani, R. C. Miniature Hall sensor based ac susceptometer for measurements of vortex and superfluid dynamics in superconducting films. *Rev. Sci. Instrum.* **75**, 141-145, (2003).

98 Dong, S., Li, J.-F. & Viehland, D. Vortex magnetic field sensor based on ring-type magnetoelectric laminate. *Appl. Phys. Lett.* **85**, 2307-2309, (2004).

99 Martins, P. *et al.* Novel Anisotropic Magnetoelectric Effect on δ-FeO(OH)/P(VDF-TrFE) Multiferroic Composites. *ACS Appl. Mater. Interfaces.* **7**, 11224-11229, (2015).

100 Gonçalves, R. *et al.* Synthesis of highly magnetostrictive nanostructures and their application in a polymer-based magnetoelectric sensing device. *Eur. Polym. J.* **84**, 685-692, (2016).

101 Li, P., Wen, Y., Liu, P., Li, X. & Jia, C. A magnetoelectric energy harvester and management circuit for wireless sensor network. *Sensors and Actuators A: Physical* **157**, 100-106, (2010).

102 Gao, J. *et al.* Giant resonant magnetoelectric effect in bi-layered Metglas/Pb(Zr,Ti)O3 composites. *J. Appl. Phys.* **112**, 104101, (2012).

103 Dong, S., Zhai, J., Li, J. F., Viehland, D. & Priya, S. Multimodal system for harvesting magnetic and mechanical energy. *Appl. Phys. Lett.* **93**, 103511, (2008).

104 Srinivasan, G., Priya, S. & Sun, N. *Composite Magnetoelectrics: Materials, Structures, and Applications*. (Elsevier Science, 2015).

105 Kambale, R. C. *et al.* Magnetoelectric properties and magnetomechanical energy harvesting from stray vibration and electromagnetic wave by Pb(Mg1/3Nb2/3)O3-Pb(Zr,Ti)O3 single crystal/Ni cantilever. *J. Appl. Phys.* **113**, 204108, (2013).

106 Zhou, Y., Apo, D. J. & Priya, S. Dual-phase self-biased magnetoelectric energy harvester. *Appl. Phys. Lett.* **103**, 192909, (2013).

107 Zhou, Y., Chul Yang, S., Apo, D. J., Maurya, D. & Priya, S. Tunable self-biased magnetoelectric response in homogenous laminates. *Appl. Phys. Lett.* **101**, 232905, (2012).

108 Patil, D. R. *et al.* Anisotropic self-biased dual-phase low frequency magneto-mechano-electric energy harvesters with giant power densities. *APL Materials* **2**, 046102, (2014).

109 Kargol, A., Malkinski, L. & Caruntu, G. in *Advanced Magnetic Materials* (Intech, 2012).

110 Kargol, A. M., L.; Caruntu, G. Biomedical applications of multiferroic nanoparticles. *In Advanced Magnetic Materials; Dr Malkinski, L., (Ed.) InTech: Rijeka, Croatia,*, 89-118, (2012).

111 Zheng, T., Zong, Y., Yue, Z., Wallace, G. G. & Higgins, M. J. in *Magnetoelectric Polymer-Based Composites* 171-195 (Wiley-VCH Verlag GmbH & Co. KGaA, 2017).

112 Paluszek, M. A., D.; Zhou, Y.; Kundu, S.; Chopra, A.; Montague, R.; Priya, S. Magnetoelectric composites for medical application. *In Composite*

Magnetoelectrics, Srinivasan, G., Priya, S., Sun, N. X., Eds.; Woodhead Publishing: Cambridge, UK,, 297-327, (2015).

113 Yue, K. *et al.* Magneto-Electric Nano-Particles for Non-Invasive Brain Stimulation. *Plos One* **7**, (2012).

114 Guduru, R. *et al.* Magneto-electric Nanoparticles to Enable Field-controlled High-Specificity Drug Delivery to Eradicate Ovarian Cancer Cells. *Scientific reports* **3**, (2013).

115 Rodzinski, A. *et al.* Targeted and controlled anticancer drug delivery and release with magnetoelectric nanoparticles. *Scientific reports* **6**, (2016).

116 Guduru, R. *et al.* Magnetoelectric 'spin' on stimulating the brain. *Nanomedicine* **10**, 2051-2061, (2015).

117 Ribeiro, C., Correia, V., Martins, P., Gama, F. M. & Lanceros-Mendez, S. Proving the suitability of magnetoelectric stimuli for tissue engineering applications. *Colloids and Surfaces B: Biointerfaces* **140**, 430-436, (2016).

118 Fukada, E. Piezoelectricity of Wood. *J. Phys. Soc. Jpn.* **10**, 149-154, (1955).

119 Fukada, E. On the piezoelectric effect of silk fibers. *J. Phys. Soc. Jpn.* **11**, 1301, (1956).

120 Fukada, E. & Yasuda, I. On the piezoelectric effect of bone. *J. Phys. Soc. Jpn.* **12**, 1158-1162, (1957).

121 Eiichi, F. & Iwao, Y. Piezoelectric Effects in Collagen. *Japanese Journal of Applied Physics* **3**, 117, (1964).

122 Rinaudo, M. Chitin and chitosan: Properties and applications. *Progress in Polymer Science* **31**, 603-632, (2006).

123 Csoka, L. *et al.* Piezoelectric Effect of Cellulose Nanocrystals Thin Films. *ACS Macro Lett.* **1**, 867-870, (2012).

124 Fukada, E. & Yasuda, I. *Piezoelectric Effects in Collagen*. Vol. 3 (1964).

125 Di Lullo, G. A., Sweeney, S. M., Körkkö, J., Ala-Kokko, L. & San Antonio, J. D. Mapping the Ligand-binding Sites and Disease-associated Mutations on the Most Abundant Protein in the Human, Type I Collagen. *Journal of Biological Chemistry* **277**, 4223-4231, (2002).

126 Moon, R. J., Martini, A., Nairn, J., Simonsen, J. & Youngblood, J. Cellulose nanomaterials review: structure, properties and nanocomposites. *Chemical Society Reviews* **40**, 3941-3994, (2011).

127 Ando, Y. & Fukada, E. Piezoelectric properties of oriented deoxyribonucleate films. *Journal of Polymer Science: Polymer Physics Edition* **14**, 63-79, (1976).

128 Lee, B. Y. *et al.* Virus-based piezoelectric energy generation. *Nat Nano* **7**, 351-356, (2012).

129 Nguyen, V., Zhu, R., Jenkins, K. & Yang, R. Self-assembly of diphenylalanine peptide with controlled polarization for power generation. *Nature Communications* **7**, 13566, (2016).

130 Shin, D.-M. *et al.* Bioinspired piezoelectric nanogenerators based on vertically aligned phage nanopillars. *Energy Environ. Sci.* **8**, 3198-3203, (2015).

131 Reches, M. & Gazit, E. Controlled patterning of aligned self-assembled peptide nanotubes. *Nat Nano* **1**, 195-200, (2006).
132 Zhang, S. Fabrication of novel biomaterials through molecular self-assembly. *Nat Biotech* **21**, 1171-1178, (2003).
133 Mata, A. *et al.* Micropatterning of bioactive self-assembling gels. *Soft Matter* **5**, 1228-1236, (2009).
134 Merzlyak, A., Indrakanti, S. & Lee, S.-W. Genetically Engineered Nanofiber-Like Viruses For Tissue Regenerating Materials. *Nano Lett.* **9**, 846-852, (2009).
135 Rong, J. *et al.* Oriented cell growth on self-assembled bacteriophage M13 thin films. *Chem. Commun.*, 5185-5187, (2008).
136 Nam, Y. S. *et al.* Biologically templated photocatalytic nanostructures for sustained light-driven water oxidation. *Nat Nano* **5**, 340-344, (2010).
137 Lee, Y. J. *et al.* Fabricating Genetically Engineered High-Power Lithium-Ion Batteries Using Multiple Virus Genes. *Science* **324**, 1051-1055, (2009).
138 Fukada, E. Vibrational study of the wood used for the sound boards of pianos. *Nature, London* **166**, 772-773, (1950).
139 Fukada, E., Date, M. & Hirai, N. Effect of temperature on piezoelectricity in wood. *Journal of Polymer Science Part C: Polymer Symposia* **23**, 509-517, (1968).
140 Maeda, H. & Fukada, E. Effect of bound water on piezoelectric, dielectric, and elastic properties of wood. *J. Appl. Polym. Sci.* **33**, 1187-1198, (1987).
141 Zhang, C. *et al.* Dissolution Mechanism of Cellulose in N,N-Dimethylacetamide/Lithium Chloride: Revisiting through Molecular Interactions. *The Journal of Physical Chemistry B* **118**, 9507-9514, (2014).
142 Kim, J., Yun, S. & Ounaies, Z. Discovery of Cellulose as a Smart Material. *Macromolecules* **39**, 4202-4206, (2006).
143 Nishiyama, Y., Langan, P. & Chanzy, H. Crystal Structure and Hydrogen-Bonding System in Cellulose Iβ from Synchrotron X-ray and Neutron Fiber Diffraction. *J. Am. Chem. Soc.* **124**, 9074-9082, (2002).
144 Bruno, F.-P., Bruno, J. & Laurent, H. First experimental evidence of a giant permanent electric-dipole moment in cellulose nanocrystals. *EPL (Europhysics Letters)* **107**, 28006, (2014).
145 Kim, J., Kang, Y. & Yun, S. Blocked force measurement of electro-active paper actuator by micro-balance. *Sensors and Actuators A: Physical* **133**, 401-406, (2007).
146 Jaehwan, K. & Yung, B. S. Electro-active paper actuators. *Smart Mater. Struct.* **11**, 355, (2002).
147 Yun, G. Y., Kim, H. S., Kim, J., Kim, K. & Yang, C. Effect of aligned cellulose film to the performance of electro-active paper actuator. *Sensors and Actuators A: Physical* **141**, 530-535, (2008).

148 Yun, G.-Y., Kim, J., Kim, J.-H. & Kim, S.-Y. Fabrication and testing of cellulose EAPap actuators for haptic application. *Sensors and Actuators A: Physical* **164**, 68-73, (2010).
149 Yun, S., Kim, J. H., Li, Y. & Kim, J. Alignment of cellulose chains of regenerated cellulose by corona poling and its piezoelectricity. *J. Appl. Phys.* **103**, 083301, (2008).
150 Sungryul, Y., Sangdong, J., Gyu-Young, Y. & Jaehwan, K. Electrically aligned cellulose film for electro-active paper and its piezoelectricity. *Smart Mater. Struct.* **18**, 117001, (2009).
151 Yang, C., Kim, J.-H., Kim, J.-H., Kim, J. & Kim, H. S. Piezoelectricity of wet drawn cellulose electro-active paper. *Sensors and Actuators A: Physical* **154**, 117-122, (2009).
152 Ureña-Benavides, E. E., Ao, G., Davis, V. A. & Kitchens, C. L. Rheology and Phase Behavior of Lyotropic Cellulose Nanocrystal Suspensions. *Macromolecules* **44**, 8990-8998, (2011).
153 Liu, D., Chen, X., Yue, Y., Chen, M. & Wu, Q. Structure and rheology of nanocrystalline cellulose. *Carbohydr. Polym.* **84**, 316-322, (2011).
154 Pei, A., Zhou, Q. & Berglund, L. A. Functionalized cellulose nanocrystals as biobased nucleation agents in poly(l-lactide) (PLLA) – Crystallization and mechanical property effects. *Composites Science and Technology* **70**, 815-821, (2010).
155 Wang, B. & Walther, A. Self-Assembled, Iridescent, Crustacean-Mimetic Nanocomposites with Tailored Periodicity and Layered Cuticular Structure. *ACS Nano* **9**, 10637-10646, (2015).
156 Siqueira, G., Bras, J. & Dufresne, A. Cellulose Whiskers versus Microfibrils: Influence of the Nature of the Nanoparticle and its Surface Functionalization on the Thermal and Mechanical Properties of Nanocomposites. *Biomacromolecules* **10**, 425-432, (2009).
157 Cranston, E. D. & Gray, D. G. Morphological and Optical Characterization of Polyelectrolyte Multilayers Incorporating Nanocrystalline Cellulose. *Biomacromolecules* **7**, 2522-2530, (2006).
158 Habibi, Y., Lucia, L. A. & Rojas, O. J. Cellulose Nanocrystals: Chemistry, Self-Assembly, and Applications. *Chemical Reviews* **110**, 3479-3500, (2010).
159 George, J. & Sabapathi, S. N. Cellulose nanocrystals: synthesis, functional properties, and applications. *Nanotechnology, Science and Applications* **8**, 45-54, (2015).
160 Newman, R. H. & Hemmingson, J. A. Carbon-13 NMR distinction between categories of molecular order and disorder in cellulose. *Cellulose* **2**, 95-110, (1995).
161 Nogi, M. & Yano, H. Transparent Nanocomposites Based on Cellulose Produced by Bacteria Offer Potential Innovation in the Electronics Device Industry. *Adv. Mater.* **20**, 1849-1852, (2008).

162 Zhu, H. *et al.* Biodegradable transparent substrates for flexible organic-light-emitting diodes. *Energy Environ. Sci.* **6**, 2105-2111, (2013).
163 Mariano, M., El Kissi, N. & Dufresne, A. Cellulose nanocrystals and related nanocomposites: Review of some properties and challenges. *J. Polym. Sci., Part B: Polym. Phys.* **52**, 791-806, (2014).
164 Gawryla, M. D., van den Berg, O., Weder, C. & Schiraldi, D. A. Clay aerogel/cellulose whisker nanocomposites: a nanoscale wattle and daub. *J. Mater. Chem.* **19**, 2118-2124, (2009).
165 Güthner, P. & Dransfeld, K. Local poling of ferroelectric polymers by scanning force microscopy. *Appl. Phys. Lett.* **61**, 1137-1139, (1992).
166 Kalinin, S. V. & Bonnell, D. A. Imaging mechanism of piezoresponse force microscopy of ferroelectric surfaces. *Physical Review B* **65**, 125408, (2002).
167 (ed File: Piezorespone of parallel and antiparallel domains.png) (Wikimedia Commons).
168 Alikin, D., Turygin, A., Kholkin, A. & Shur, V. Ferroelectric Domain Structure and Local Piezoelectric Properties of Lead-Free (Ka0.5Na0.5)NbO3 and BiFeO3-Based Piezoelectric Ceramics. *Materials* **10**, 47, (2017).
169 McQuaid, R. G. P., McMillen, M., Chang, L. W., Gruverman, A. & Gregg, J. M. Domain wall propagation in meso- and nanoscale ferroelectrics. *J. Phys.: Condens. Matter* **24**, 024204, (2012).
170 Rodriguez, B. J., Callahan, C., Kalinin, S. V. & Proksch, R. Dual-frequency resonance-tracking atomic force microscopy. *Nanotechnology* **18**, 475504, (2007).
171 Bintachitt, P., Trolier-McKinstry, S., Seal, K., Jesse, S. & Kalinin, S. V. Switching spectroscopy piezoresponse force microscopy of polycrystalline capacitor structures. *Applied Physics Letters* **94**, 042906, (2009).
172 Jesse, S., Baddorf, A. P. & Kalinin, S. V. Switching spectroscopy piezoresponse force microscopy of ferroelectric materials. *Appl. Phys. Lett.* **88**, 062908, (2006).
173 Pang, H. *et al.* Preparation of epitaxial hexagonal YMnO3 thin films and observation of ferroelectric vortex domains. *npj Quantum Materials* **1**, 16015, (2016).

Chapter 2: Regenerated Cellulose-Based Magnetoelectric Composites

2.1. Introduction

Compared to rare single phase ME crystals (*e.g.* Cr_2O_3),[1] ME composites are attractive for their ease of processing and, importantly, superior ME response at room temperature[2,3] to enable practical devices such as sensors for ultralow magnetic field detection[4]. ME composites consist of both piezoelectric (PE) and magnetostrictive (MS) components, and the ME effect of the composite is not the natural property *per se*, but is actually the result of tensor properties.[5] That is, when an external magnetic field is applied to the composite, the magnetic component changes its shape magnetostrictively to induce strain on the PE component, causing dielectric polarization. This uniquely indirect two-phase strain coupling provides the flexibility of optimizing both the PE and MS phases and their interface to enhance the ME response[6].

Generally, the use of MS materials with high magnetic permeability and low field saturation, such as Metglas[7,8], provides the possibility of inducing fast mechanical deformation under relatively weak magnetic fields. Combining Metglas with the highest piezoresponsive polymers, such as PVDF[9], gives rise to significant strain transfer and the highest ME voltage outputs. As such, PVDF and its copolymers have

been exclusively studied since the first ME polymer composite consisting of PVDF was demonstrated in 2001 and expected developments in exploring other types of PE polymers have not been forthcoming.[10] This has led to the emergence of a central dogma where PVDF is viewed as the "material of merit", despite the enormous potential for other polymers to bring significant added value properties and function to ME composite devices.

Actually in nature, there are numerous biomolecules possessing piezoelectricity.[11-14] Exploring advances in harnessing the unique structures and properties of naturally occurring PE biopolymers will transpose the aforementioned central dogma and broaden the application base for ME composites. In particular, cellulose is the most substantial organic substance in nature[15] and the origin of its PE response, discovered early in wood[16], comes from inherent crystallinity (**Figure 2.1a**) [17]. As a very cheap and renewable material, it is developing rapidly as a supporting substrate for flexible and transparent electronics[18,19], and recently fabricated as PE paper for actuation, energy harvesting and acoustic applications[20].

The primary aim of this chapter is to verify the processibility of developing ME composites based on the natural biopolymer, cellulose. In regenerated cellulose, the degree of crystallinity is usually at a low level and improving the alignment of cellulose fibrils, *e.g.* either through stretching or heat, is an effective method to enhance piezoelectricity, as the ordered structure (**Figure 2.1b**) is preferred for crystalline generation[20,21]. To fabricate the cellulose-based ME composites, laminate

(bilayer) structures comprising Metglas and regenerated cellulose films were employed, enabling two-phase strain coupling for an enhanced ME response[22]. Cellulose films were obtained from regular solution processing methods and the pristine wet film was air-dried at room temperature or alternatively hot-pressed to assess the effect of heat treatment on the cellulose crystallinity and overall ME response. The final laminate composite (**Figure 2.1c**) was tested using a dynamic method (**Figure 2.1d**) to quantify the ME frequency response and the influencing factors, such as the laminate length and residual water in cellulose, on ME output voltage.

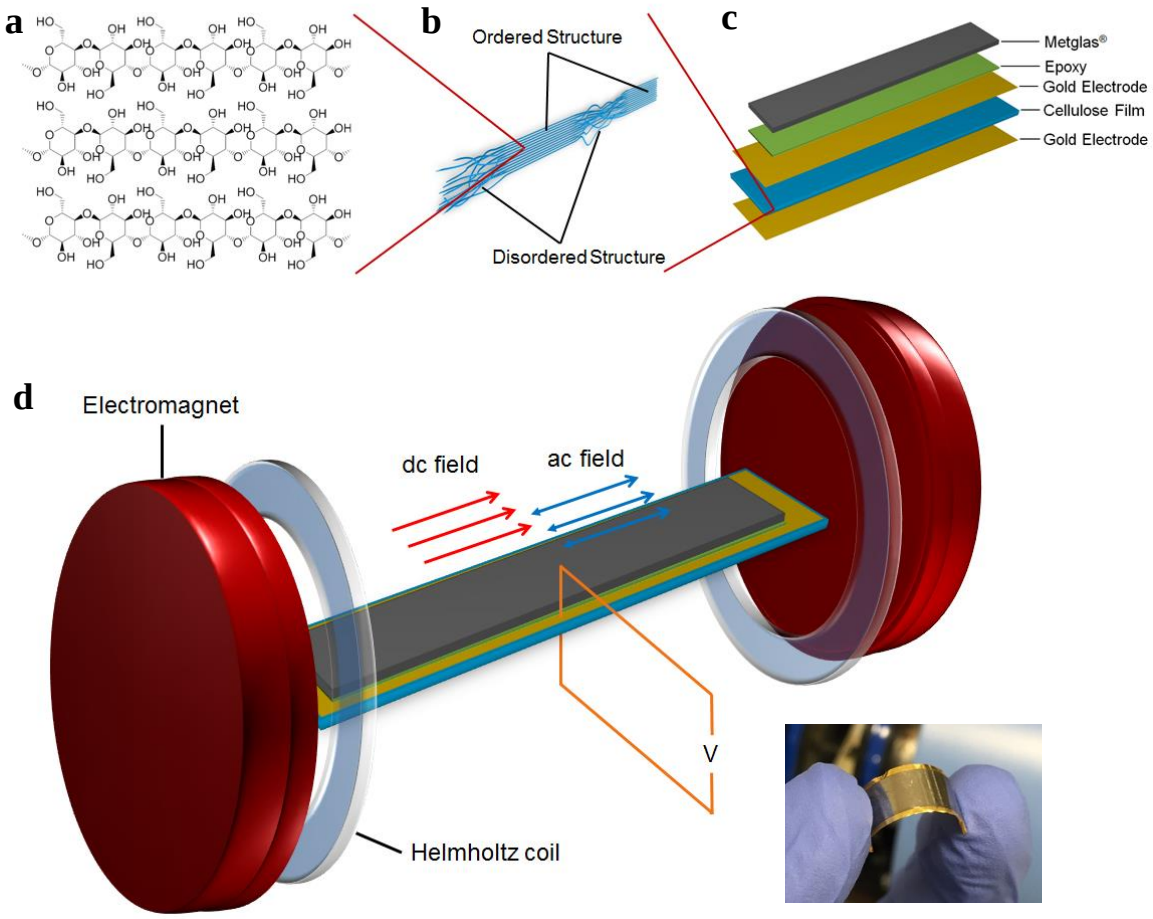

Figure 2.1. (a) Scheme of cellulose crystal II, the most common crystalline type in regenerated cellulose materials. The saccharide unit provides dipolar segments along the aligned fibril thus rendering the PE nature. (b) Illustration of cellulose fibril alignment at the cross-section of cellulose film. Part of the ordered structure provides crystalline properties. (c) Schematic of cellulose based ME laminate structure. (d) Schematic view of the bulk system for ME voltage measurement. The inset below shows the picture of the final cellulose ME laminate used in the measurements.

2.2. Experimental Methods

Cellulose Films Preparation: Cellulose solution was prepared using anhydrous DMAc (Sigma-Aldrich 271012)/LiCl (Sigma-Aldrich 746460) solvent system and heated to 80 ℃ with constant stirring. The w.t. % of cellulose, DAMc and LiCl are 1%, 9%, 90%, respectively. In order to increase the solubility, α-cellulose (Sigma-Aldrich C8002) was first processed with a pre-solution exchange method[23]. Briefly, the cellulose powder (**Figure 2.2a**) was suspended in DI water over night and then moved to methanol for 1 hr. After filtration, the cellulose was exchanged alternately in methanol and DMAc for 4 cycles and the resulting mixture of cellulose and anhydrous DMAc stored under nitrogen prior to further use. Cellulose films were fabricated *via* a regular film casting. 1.6 g (~1 mL) of cellulose solution (**Figure 2.2b**) was spread onto microscope glass slide and the pre-film solution was evaporated in a fume hood overnight. The cast gels (**Figure 2.2c**) were washed in a solution of DI water/isopropanol (3:1 in volume) and then immersed in DI water for 3 days with frequent exchange of fresh DI water changing in order to remove the residual solvent. The cleaned gel-like films were air-dried at room temperature (control film) or hot-pressed by clamping between hexamethyldisilazane (HDMS) treated hydrophobic glass slides in a vacuum oven at 60 ℃ (hot-pressed film). The thickness of the hot-pressed and control film was 19 ± 2 μm and 27 ± 3 μm, respectively, as measured using a micrometer calliper.

Figure 2.2 Cellulose in different forms: (a) α-cellulose powder; (b) Cellulose solution in DMAc/LiCl solvent system and (c) regenerated cellulose film in gel condition.

ME Laminate Composite Fabrication: The cellulose films were sputter coated with 50 nm gold layers on both sides (**Figure 2.1c**) and then cut into a 40 mm × 8 mm rectangular using a scalpel. To fabricate the ME laminate composites, a 36 mm × 6 mm Metglas 2605 SA1 tape was glued on the central part of the cellulose film using commercial Devcon epoxy (**Figure 2.1c**). To ensure even distribution, the Epoxy was pre-heated to 60 ℃ to improve the liquidity.

Bulk ME Effect Measurement: A Helmholtz coil was used to apply ac magnetic fields in the frequency range of 20.1 - 92.1 KHz and an electromagnet was used to generate dc magnetic field with various strength. Both the ac and dc fields were applied simultaneously along the length direction of the ME laminate composites (**Figure 2.1d**) and the induced output voltage across the top and bottom electrodes was recorded using a model SR8 10 DSP lock-in amplifier. This is the dynamic

method used for ME effect measurement and the details can be found in Chapter 1, Figure 1.10.[24]

Piezoresponse Force Microscopy: The local PE response of the cellulose films was quantified using an Asylum MFP-3D Atomic Force Microscope (Asylum Research, Santa Barbara, US) in the Piezoresponse Force Microscopy (PFM) mode, as described above in chapter 1 (**see page 49**). A conductive tip (EFM-50, Nanosensors) with Pt/Ir coating), resonant frequency of 68 kHz and spring constant of 2.8 N m^{-1} was used for the PFM measurements. The sensitivity of the tip was calibrated on a glass slide based on a force curve measurement. Height, amplitude and phase images were specifically obtained in Dual AC Response Tracking (DART) mode[25], with contact resonant frequency of ~ 320 kHz. The PE response was measured as the first-harmonic of bias-induced tip deflection, $d = d_0 + A\cos(\omega t + \varphi)$, where d_0 is the equilibrium position of the tip; A is the amplitude and ω is the frequency of applied bias; φ is the phase yielded information on the polarization direction below the tip. To study the polarization switching dynamics, the Switching Spectroscopy-PFM (SS-PFM) technique was used to obtain local PE hysteresis loops. For each sample, spectroscopy measurements were acquired by applying a bias voltage in a matrix of 7×8 points across a 3×3 μm^2 area. The applied voltage during the SS-PFM measurement was in the range of ± 25 V, with the frequency of 1Hz. In particular, the AFM was modified by connecting an external amplifier to increase the applied voltage to enable a fully saturated switching dynamic. All SS-PFM loops were acquired in off-state and a

driving amplitude of 200 mV was used for all measurements. Note: the applied voltage mentioned above is the bias on the tip to induce PE response, and the driving amplitude is used to oscillate the tip for measurement.

Differential Scanning Calorimetry (DSC): Thermograms of hot-pressed and control cellulose films were obtained by using a TA Instrument Q100 DSC in the range of 25-450 ℃, with a heating rate of 10 ℃ min^{-1}.

Thermogravimetric analysis (TGA): TA Instrument SDT Q600 thermal analysis system was employed for thermogravimetric analyses. The measurements were run under an atmosphere with flowing 9:1 oxygen/nitrogen from 25℃ to 425 ℃ at a ramping rate of 10 ℃ min^{-1}.

Scanning Electron Microscopy (SEM): The samples were firstly fixed onto a SEM specimen holder and sputter coated with 50 nm thick gold layer. Cross-section morphology of air-dried and hot-pressed cellulose films were imaged using SEM (JEOL JSM-7500FA), with an accelerating voltage of 5.0 kV and emission current of 10 mA.

2.3. Results and Discussion

2.3.1 ME Response of Regenerated Cellulose Based Composites

To measure the ME response and coefficient (α_{ME}), the applied H_{dc} and H_{ac} strengths were fixed and α_{ME} was recorded as a function of the H_{ac} frequency. For both the air-dried and hot-pressed cellulose ME laminates, a significant increase in α_{ME} was observed with a peak maximum at a H_{ac} frequency of ~56.1 kHz (**Figure 2.3a and b**), indicating a resonance enhancement effect that is characteristic of an ME response in laminate structures[22]. In this case, once the H_{ac} frequency coincided with the resonant frequency of the MS structure (*i.e.* Metglas film), the mechanical strain was amplified, thus causing a significant enhancement in the α_{ME}. The resonant frequency (f_r) of the MS layer, if oscillating with a free end, depends on its density (ρ), Young's modulus (E) and the length (L) along the magnetic field[26], and is given by:

$$f_r = 1/2L \times \sqrt{E/\rho} \qquad (2.1)$$

For Metglas, E=100~110 GPa and ρ= 7.18×10^3 kg/m^3. In our case, L=36 mm, thus the calculated theoretical f_r of 51.8~54.4 kHz is very close to the experimental α_{ME} resonance peak values in **Figure 2.3a, b**. For **Figures 2.3a, b**, ME responses are specifically shown for different applied H_{dc} of 10.8 Oe and 5.9 Oe for the hot-pressed and air-dried samples, respectively, because these H_{dc} produce a symmetrical Lorentzian resonance profile as opposed to a non-symmetrical profile, which is discussed later in **Section 2.4.2**. Displayed in **Figure 2.3c** is the actual resonant α_{ME}

under different H_{ac} strength while the H_{dc} strength was fixed at the respective values given in **Figures 2.3a, b**. Under these H_{dc} strengths, the α_{ME} of the air-dried sample was slightly higher than the hot-pressed sample. Furthermore, the linear increase in the α_{ME} as a function of H_{ac} for both samples confirmed the existence of an ME effect (**Figure 2.3c**). Despite the air-dried samples having higher α_{ME} for the symmetrical Lorentzian resonance condition, the hot-pressed samples gave significantly higher α_{ME} at all other H_{dc} strengths (**Figure 2.3d**). More specifically, **Figure 2.3d** shows the resonance α_{ME} as a function of H_{dc} strength. The hot-pressed samples showed a maximum α_{ME} at H_{dc}=4.2 Oe, as high as 1.41 V cm^{-1} Oe^{-1}, which is importantly considered to be in a practically useful range.[9] Comparatively, the air-dried sample showed a similar H_{dc} dependent behaviour, with significantly less maximum α_{ME} of 0.59 V cm^{-1} Oe^{-1} occurring at H_{dc}=3.9 Oe. Furthermore, it is expected that the maximum ME output voltage can be further enhanced by increasing H_{ac}, as given by the linear relationship (*i.e.* 1.48 mV Oe^{-1} for the hot-pressed sample when H_{ac}=2.0 Oe) in **Figure 2.3c**.[27,28]

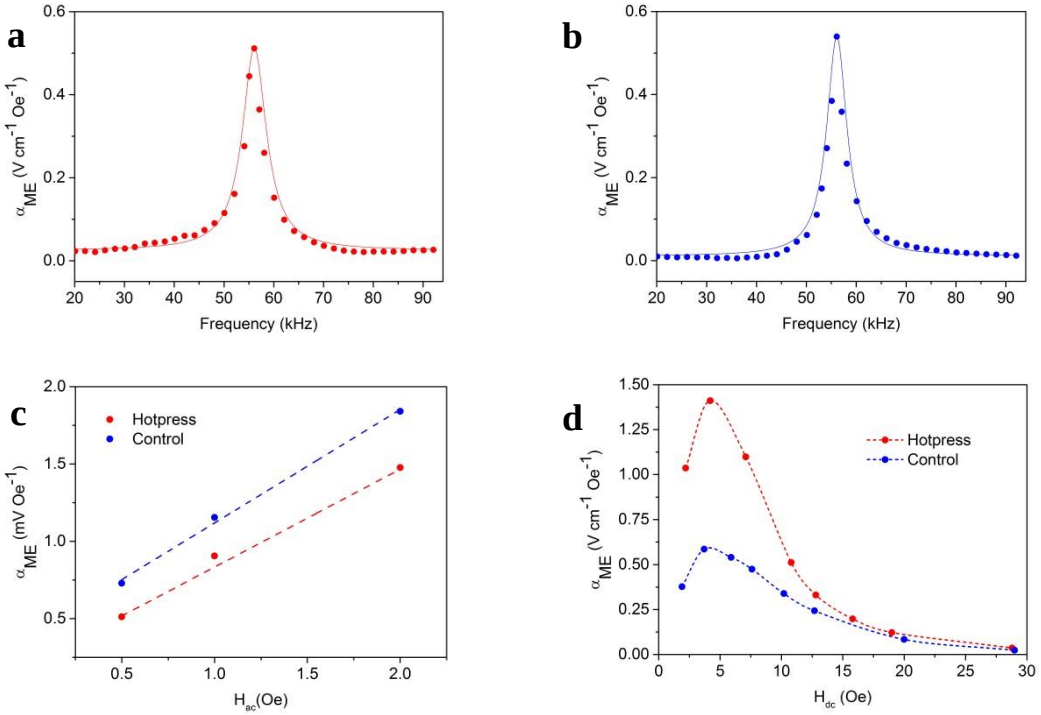

Figure 2.3. (a,b) ME voltage coefficient as a function of H_{ac} frequency when (a) H_{dc}=10.8 Oe for hot-pressed sample and (b) H_{dc}=5.9 Oe for the control sample. The experimental data points were fitted to a Lorentzian resonance model (the solid line) using equation: $y = y_0 + \frac{2A}{\pi} \times \frac{w}{4(x-x_c)^2+w^2}$, where y_0 is the baseline, A is the area of the peak, w is the peak width and x_c is the frequency of peak center. The resonance of peaks (x_c) was found at 56.1 kHz. (c) The resonant ME output voltage as a function of applied H_{dc} strength. The ME laminates were induced by H_{dc}=10.8 Oe for hot-pressed sample and H_{dc}=5.9 Oe for the control sample at which a Lorentzian resonance profile has been observed. (d) Resonance enhanced α_{ME} as a function of H_{dc} for hot-pressed (red dot-line) and control (blue dot-line). All data is obtained under H_{ac}=0.5 Oe.

The α_{ME} was also derived from a ME equivalent circuit method[29], which is expressed as[7]:

$$\alpha_{ME} = \frac{n d_{33,m} d_{31,p}}{n\varepsilon_0 \varepsilon_{33}^S s_{11}^E + (1-n) s_{33}^H (\varepsilon_0 \varepsilon_{33}^S + d_{31,p}^2 / s_{11}^E)} \quad (2.2)$$

where n is the magnetic phase thickness ratio; s_{11}^{E} and ε_{33}^{S} are the elastic compliances of the PE and MS layers; ε_0 and ε_{33}^{S} are the vacuum permittivity and the dielectric constant of PE layer at constant strain; $d_{33,m}$ and $d_{31,p}$ are the longitudinal piezomagnetic and transverse PE coefficients, respectively. According to the measured α_{ME}, elastic moduli (**Figure 2.4**)[30] and dielectric constant[31] of regenerated cellulose films, and the MS coefficient of Metglas SA1[7], the effective $d_{31,p}$ was estimated as 5.95 and 1.55 pC.N^{-1} for hot-pressed and air-dried cellulose films, respectively. These values are similar to early reported results of pristine and electrically aligned cellulose films[32] but are significantly lower than those of optimized PVDF copolymers (the highest d_{31} can reach up to 28.6 pC N^{-1}). Since the Young's modulus was measured to be 3.95 GPa for both types of cellulose films, it is suggested that the ME response mainly depends on the degree of crystallinity in the regenerated cellulose. Thus, it is reasonable to assume that optimization of cellulose crystallinity could be an effective way to enhance the PE effect and further improve the α_{ME} of the cellulose-based ME composite.

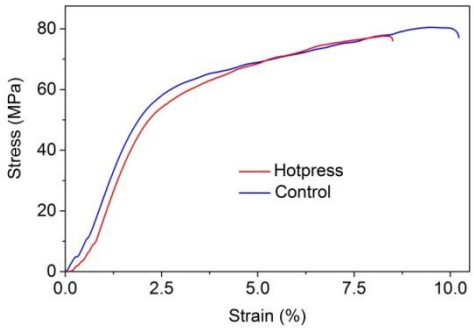

Figure 2.4 Tensile tests of the aired control film and the hot-pressed (60 ℃) film. The Young's modulus is calculated as 3.95 GPa for both two films**.**

2.3.2 Fano-Resonance of the Magnetoelectric Effect

Remarkably, a Fano-resonance effect was observed to accompany the ME resonance enhancement (**Figure 2.5**). Firstly, the hot-pressed showed a symmetrical Lorentzian resonance profile at an applied H_{dc}=10.8 Oe (**Figure 2.5b**), as given earlier in **Figure 2.3a**. However, a Fano-like resonance, featuring an anti-resonance peak, appears when the H_{dc} was below (**Figure 2.5a**) and above (**Figure 2.5c**) the H_{dc} of 10.8 Oe. At a H_{dc}<10.8 Oe, the anti-resonance peak occurs at a frequency value that was higher than the resonant peak (**Figure 2.5a**), while if H_{dc}>10.8 Oe the anti-resonance damping peak occured at lower frequencies (**Figure 2.5c**). Similarly, the air-dried sample showed a Fano-like resonance, with a shift in the anti-resonance occurring at H_{dc} above and below the H_{dc} (5.9 Oe) for the symmetrical Lorentzian resonance (**Figure 2.5d-f**).

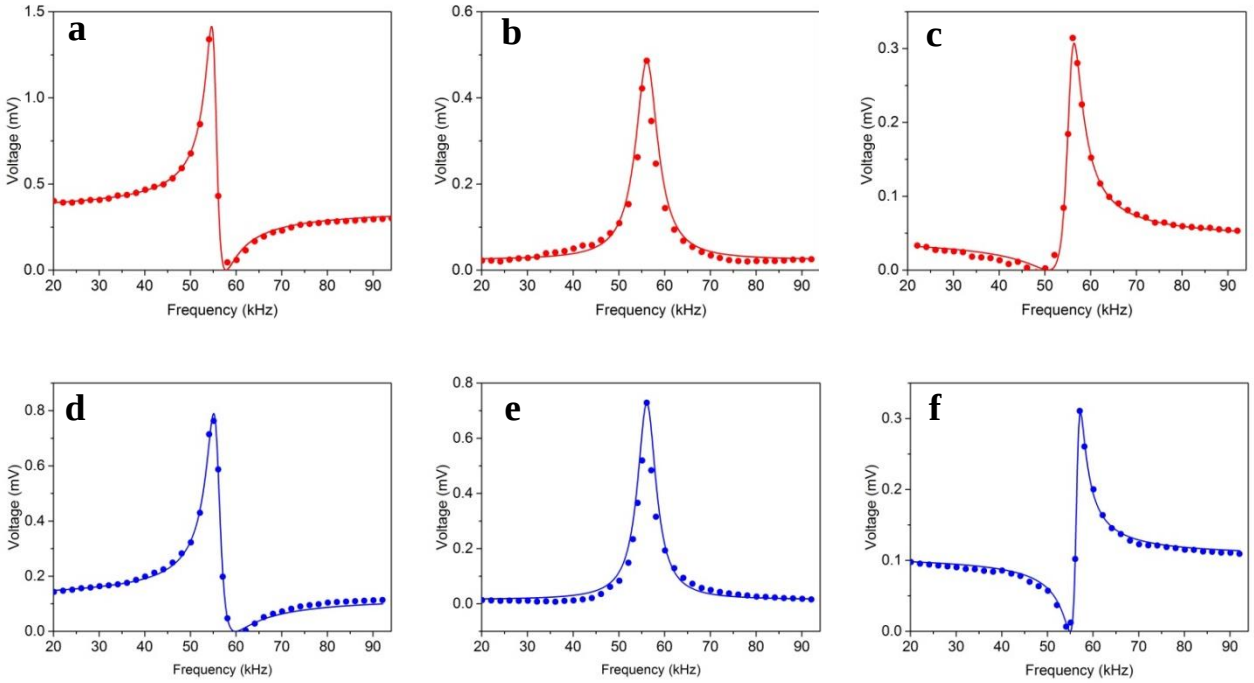

Figure 2.5. (a-c) ME output voltage of hot-pressed sample as a function of H_{ac} frequency under (a) H_{dc}=4.2 Oe, (b) H_{dc}=10.8 Oe and (c) H_{dc}=12.8 Oe. (d-f) ME output voltage of air-dried sample as a function of H_{ac} frequency under (a) H_{dc}=3.9 Oe, (b) H_{dc}=5.9 Oe and (c) H_{dc}=12.7 Oe. The experimental data (dots) are fitted to a modified Lorentzian equation (2.3) (shown as solid lines).

To assess the Fano-resonance profile, the α_{ME} output voltage curves measured as a function of H_{dc} were fitted to a modified Maxwell equation:

$$V(\omega) = A\left|\frac{\omega^2 - 2i\delta_a\omega_a\omega - \omega_a^2}{\omega^2 - 2i\delta_r\omega_r\omega - \omega_r^2}\right| + a\omega + b \qquad (2.3)$$

where A is the amplitude constant; $\omega_r = 2\pi f_r$ is the resonance frequency and $\omega_a = 2\pi f_a$ is the anti-resonance frequency; δ_r and δ_a are the damping constants for the resonance and anti-resonance, respectively; a is the constant corresponding to a linear

background voltage and b is the factor fitting the imaginary section to experimental data. The background noise was subtracted and only the actual ME output voltage was shown. Fits to the data (solid line) are given in **Figure 2.5** and all fitting parameters are summarized for the hot-pressed and air-dried samples in **Tables 1 and 2**.

Table 1. Fitting parameters (imaginary section) of equation (2.3) for anti-resonance frequency effect of hot-pressed cellulose ME laminate under different H_{dc} strength.

H_{dc} (Oe)	A (mV)	f_r (kHz)	f_a (kHz)	δ_r	δ_a
2.2	0.3881	54.8121	56.0363	-0.0240	0.0308
4.2	0.5125	55.4388	57.2276	-0.0246	0.0330
7.1	0.3653	55.7093	58.2671	-0.0257	0.0253
12.8	0.1077	55.6533	51.3223	0.0349	-0.0363
15.8	0.0655	56.1777	54.6733	0.0285	-0.0538
19	0.0512	56.7783	56.6211	0.0263	-0.0343
28.8	0.0049	57.3357	61.6959	0.0277	-0.1483

Table 2. Fitting parameters (imaginary section) of equation (2.3) for anti-resonance frequency effect of air-dried cellulose ME laminate under different H_{dc} strength.

H_{dc} (Oe)	A (mV)	f_r (kHz)	f_a (kHz)	δ_r	δ_a
1.9	0.2039	55.5821	58.0353	-0.0336	0.0523
3.9	0.2102	55.8666	57.2276	-0.0312	0.0504
7.6	0.1414	55.6457	49.5998	0.0308	-0.0362
10.2	0.1027	56.2105	51.3223	0.0275	-0.0660
12.7	0.0682	56.4616	54.8179	0.0191	-0.0646
20	0.0512	56.2052	56.1057	0.0315	-0.0402
29	0.0232	58.1695	57.9086	0.0411	-0.0167

Fano-resonances were widely observed in different fields of physics, *e.g.* photonic materials and crystals[33], and recently reviewed for plasmonic nanoparticles and metamaterials[34]. They were also seen in electromechanical coupling of PE materials, for example, in impedance measurements of common lead zirconate titanate (PZT)[35] and generally described as occurring due the interference between continuum and discrete states. However, the Fano-resonances of PE materials have shown not to impose on the frequency line shape of ME responses[35] and therefore until now have not yet been experimentally observed in ME composites, including both polymer (*i.e.* PVDF) and surprisingly ceramic-based composites that were first established more than 4 decades ago. Theoretical modelling has predicted Fano-resonances either as a conductivity change[36] or the interference of two excitation pathways of ME laminate cantilever structures[37], or those oscillating with free ends[38]. Though despite these models, the lack of experimental evidence suggests that cellulose as a PE material

within ME composites possess unique PE mechanisms, mechanical properties and coupling that contribute to the occurrence of a Fano-resonance.

To further understand the origin of the Fano-resonance, the possible role that water may play was investigated by assessing cellulose with varying degrees of water content. Compared to the ME frequency response of cellulose films prepared at room temperature and with hot-presseding under 60 ℃ (**Figures 2.3 and 2.5**), cellulose films hot-pressed at higher temperatures of 100 ℃ to remove most of the residue water also showed a Fano-resonance effect with the frequency peak of the symmetric Lorentz profile occurring at significantly higher H_{dc} field (**Figure 2.6a-c**). More specifically, the resonance peak shifted from 5.9 Oe in air-dried sample and 10.8 Oe in the 60 ℃ hot-pressed samples up to 13.1 Oe in the 100 ℃ hot-pressed sample (**Figure 2.6d**). Shifts in the frequency values of the anti-resonance, either positioned above or below the resonance peak, also occured due to variations in the water content and are qualitatively related to changes in the quality factor, *i.e.* damping of the ME frequency response. That is, with less water content the resonance and anti-resonance peaks become broader (**Figure 2.6a-c**, hot-pressed 100 ℃) as opposed to being narrower if the water content was increased (**Figure 2.5a-c**, hot-pressed 60 ℃). A further increase in water content gave the narrowest resonance peak, or highest quality factor, in the air-dried films (**Figure 2.5d-f**, air-dried). Thus, this directly influences the distance between the anti-resonance and resonance peaks (**Figure 2.6e**). These changes in the frequency profile indicate that water had a

significant effect on the ME response, including the Fano-resonance which still persists when removal of most water is expected.

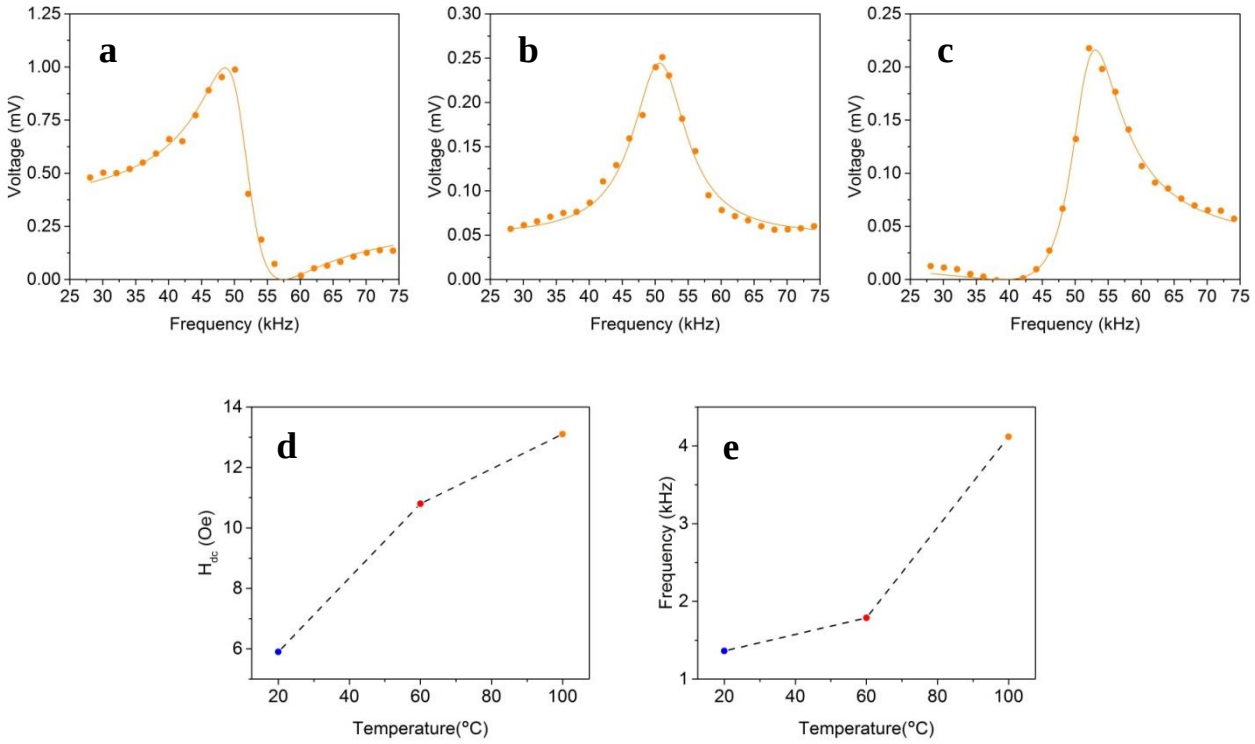

Figure 2.6 (a-c) ME output voltage of hot-pressed sample at 100 ℃ as a function of H_{ac} frequency under (a) H_{dc}=4.2 Oe, (b) H_{dc}=13.1 Oe and (c) H_{dc}=19.0 Oe. The experimental data (dots) were fitted to a modified Maxwell equation (2.3) or Lorentzian function mentioned in Figure 2.3 (shown as solid lines). (d,e) The effect of water content on (d) the occurring H_{dc} strength of symmetric Lorentz resonance peak and (e) the frequency difference between the anti-resonance (f_a) and the resonance (f_r) peak under optimum H_{dc} strength. Note: the air-dried sample is corresponding to 20 ℃ and the two hot-pressed samples are corresponding to 60 and 100 ℃.

In an attempt to completely eliminate the effects of water and to produce highly homogenous crystalline cellulose, without the amorphous regions found in regenerated cellulose, ME laminate composites was prepared based on nanocrystalline cellulose (see details of preparation in **Chapter 3. Experimental Section**) to further elucidate the Fano-resonance. In this case, the highly crystalline form had almost no porous structure, thus minimizing the effect of residual water and heterogeneity (*i.e.* crystalline *vs* amorphous regions) in the PE layer. From these ME composites using the similar configuration and dimensions, a Fano-resonance was present although the anti-resonance only occurs at frequencies below the resonance and extraordinarily no symmetrical resonance profile was observed at any applied H_{dc} field (**Figure 2.7**). Collectively, water played an ostensible role in the ME response however experiments using nanocrystalline cellulose suggest that it is the unique and inherent chemical structure of cellulose that gives rise to the Fano-resonance effect.

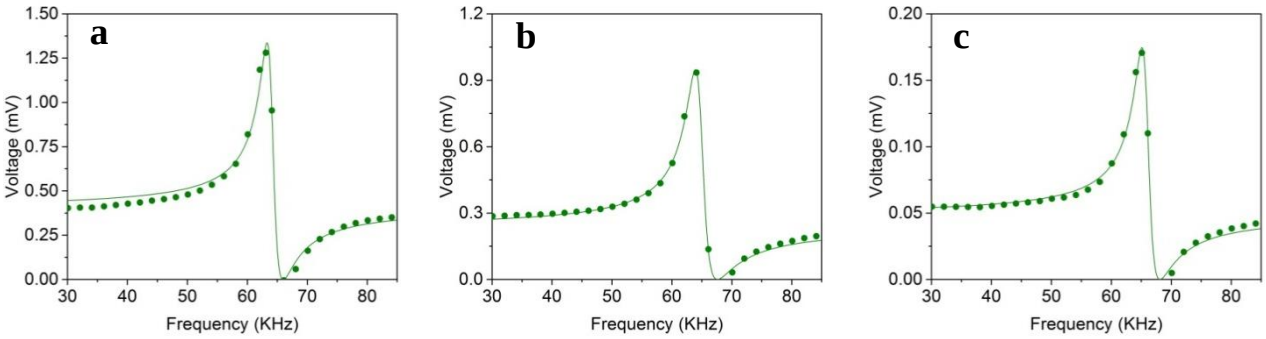

Figure 2.7 ME output voltage of cellulose nanocrystal based ME laminate at as a function of H_{ac} frequency under (a) H_{dc}=2.3 Oe, (b) H_{dc}=12.2 Oe and (c) H_{dc}=23.6 Oe. The experimental data (dots) are fitted to a modified Maxwell equation (2.3) (shown as solid lines).

At the bulk scale, the strain coupling of the PE and MS can be divided into two pathways: the tension strain caused by magnetostriction and bending strain that is attributed to the configurational asymmetry of a bilayer, shrinkage of epoxy while drying, and mechanical properties of the cellulose. When the tension and bending strains were at equilibrium, the resonance frequency curve of the α_{ME} output voltage was a symmetrical Lorentzian profile. However, at H_{dc} values less or greater than H_{dc}= equilibrium, where the driving force for tension strain was either too weak or strong, then interference coupling on the equilibrium bending-tension strain results in a Fano-resonance profile.

The equilibrium strain coupling giving a symmetrical Lorentzian profile was observed at H_{dc}=10.8 Oe for the hot-pressed (**Figure 2.3a**) and H_{dc}=5.9 Oe for air-dried (**Figure 2.3b**). Since equivalent procedures and MS components were used to fabricate the laminates, a difference in the anti-resonance dependence on H_{dc}, as well as the damping coefficients (**Tables 2.1 and 2.2**), from the fitting are likely to be attributed to the different frequency-dependent strain transfer and tensile capacity of the cellulose as a consequence of their different processing methods (*i.e.* air-dried versus hot-pressed). Further to this, anti-resonance is useful for deconvolving the properties of complex mechanically coupled systems, and will be fundamentally important for elucidating the ME mechanisms in cellulose.

2.3.3. Crystallinity and Morphology of Cellulose

The overall increased performance of hot-pressed cellulose ME laminate compared to the air-dried (**Figure 2.3d**) is presumably due to the PE properties of each cellulose film, as determined by the extent of crystallinity. To verify this, DSC was employed to study hot-pressed and air-dried cellulose films by quantifying the heat associated with melting of the polymer (**Figure 2.8a**). Thermal analysis of the endothermic peaks corresponding to the melting process indicated the hot-pressed sample adsorbed significantly higher energy, with fusion enthalpies of 50.49 $J.g^{-1}$ and 9.39 $J.g^{-1}$ for the hot-pressed and air-dried, respectively, suggesting a higher crystalline content in former. Further TGA analyses indicate that the two different cellulose decompose at different temperature (**Figure 2.8b**). The difference of crystalline content was explained by changes in cellulose morphology, as evident in SEM images of film cross-sections (**Figure 2.8c and d**). In hot-pressed films, the cellulose displayed a layered, or aligned fibrous structure, consisting of smaller fibrils with uniform distribution along the longitudinal direction of the film (**Figure 2.8c**). In contrast, the air-dried film shows a less distinct anisotropic structure, particularly with the absence of smaller fibril structures (**Figure 2.8d**).

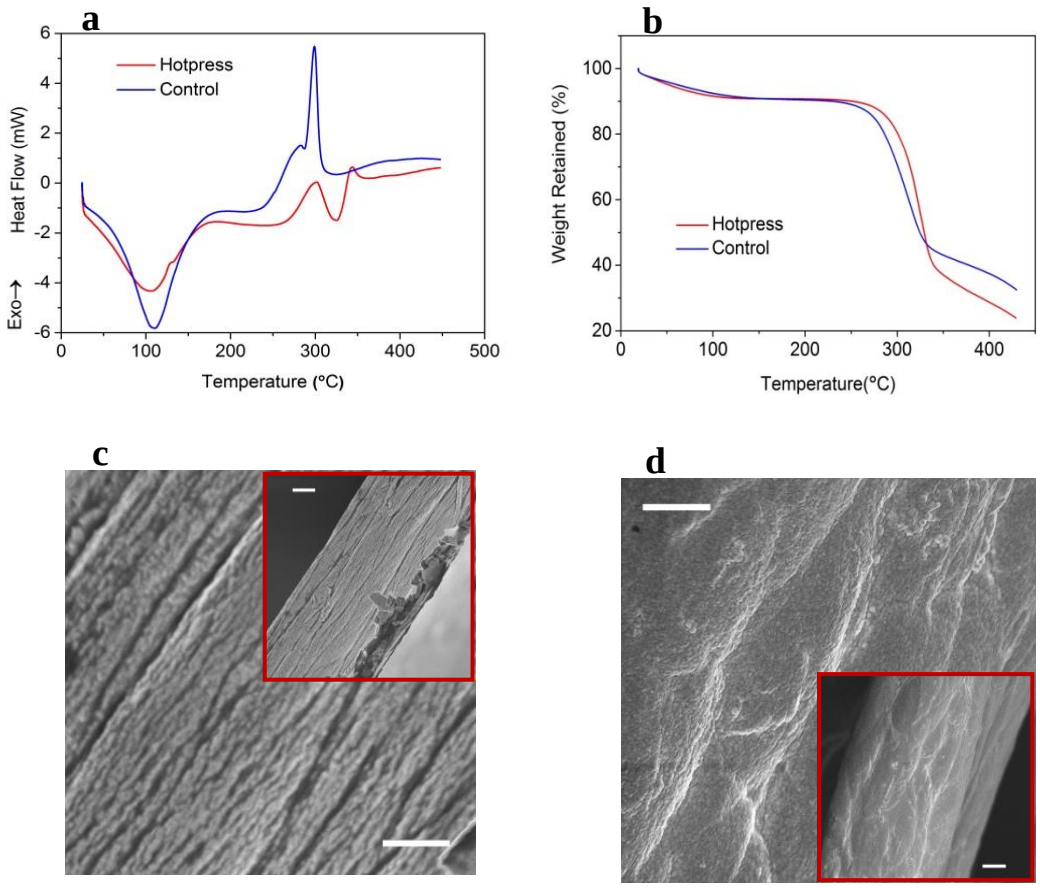

Figure 2.8 (a,b) DSC thermograms of hot-pressed (red line) and control (blue line) films. The melting and oxidation temperatures were 302.9 and 345.5 ℃ for hot-pressed film; 281.3 and 299.0 ℃ for air-dried film. The endothermic peak in this range corresponds to melting process of cellulose[39]. (b) TGA result of the difference of oxidation (decomposition) temperature of the two films. (c,d) SEM cross-section images of (c) hot-pressed and (d) air-dried cellulose films. The magnification was 15000 X for detailed view (scale bar 1 μm) and 5000 X for full view (inset, scale bar 2 μm).

2.3.4. PE Properties of Cellulose by Piezoresponse Force Microscopy

Piezoresponse force microscopy (PFM) was used to understand the relationship between the cellulose crystallinity, residual water content, ME output voltage and the

local PE properties of the hot-pressed versus air-dried films (**Figure 2.9**). It needs to note that the maximum tip bias applied for scanning was 10 V as higher voltage caused degradation of the cellulose films. For hot-pressed films, the amplitude response within domains was in excess of 100 pm (yellow-to-orange regions), with surrounding regions having values of ~ 60 pm (darker green) (**Figure 2.9a**). The amplitude response from air-dried was significantly lower with values of ~ 60 pm within domains (darker green) and surrounding regions < 40 pm (blue) (**Figure 2.9b**). The amplitude response (displacement) is related to the rotation of dipoles and is also associated with the movement of polymer matrix. Since the dipoles are on polymer chains, the rotation causes stretching/shrinking of the chains. This also greatly contributes to the displacement. Water will shield the tip bias thus reducing the PE response level. Higher crystallinity also improves the sensitivity to induce a bias, giving rise to higher response value. Domain sizes of ~ 100-200 nm were interpreted as piezoresponsive regions rather than single crystalline domains and previous PFM studies show similar domain sizes in biological tissues[40]. However, the PE domain direction associated with crystalline cellulose, as well as the details of PE mechanism is not well understood at this current stage.

SS-PFM measurements were further employed to elucidate the polarization switching dynamics of the differently treated cellulose films. Representative hysteresis loops of the hot-pressed sample (**Figure 2.9c**) appear as a typical butterfly shape in the amplitude displacement (red curve) and the corresponding phase change was ≈ 180˚,

confirming a fully reversible polarization dynamic[21,22]. The air-dried film, on the other hand, showed an unsaturated piezo-response at positive biases (**Figure 2.9d**), as indicated by significantly less amplitude displacement located on the right wing of the butterfly loop compared to the left wing or negative bias. In addition, the corresponding phase changes were far below 180˚, indicating that a completely reversible polarization process was not achieved. This lower amplitude displacement and incomplete polarization switching was attributed to the lower crystallinity degree though the shielding effect of residual water could also be a contributing factor in air-dried films. Generally, there are two types of water molecules in regenerated cellulose film, namely, the free water and bound water in the cellulose matrix.[20] Free water molecules are easily removed by heating treatment, however, the bound water can persist even at high temperatures. Statistical analysis of bias induced piezoresponse at a maximum of -25 V showed the histogram peak distribution of the amplitude displacement for the hot-pressed film under 60 ℃ is 3-fold higher than the air-dried (**Figure 2.9e**), thus confirming differences observed in the PFM amplitude images. Similarly, the hot-pressed films under 100 ℃ showed significantly higher amplitude displacement in the butterfly curves (**Figure 2.10a**), with peak distribution values of ~160 pm (**Figure 2.10b**) that are comparable to the 60 ℃ films. Therefore, a decrease in the water content accompanied by an increase in crystallinity gave rise to higher PE response and complete polarization in hot-pressed films.

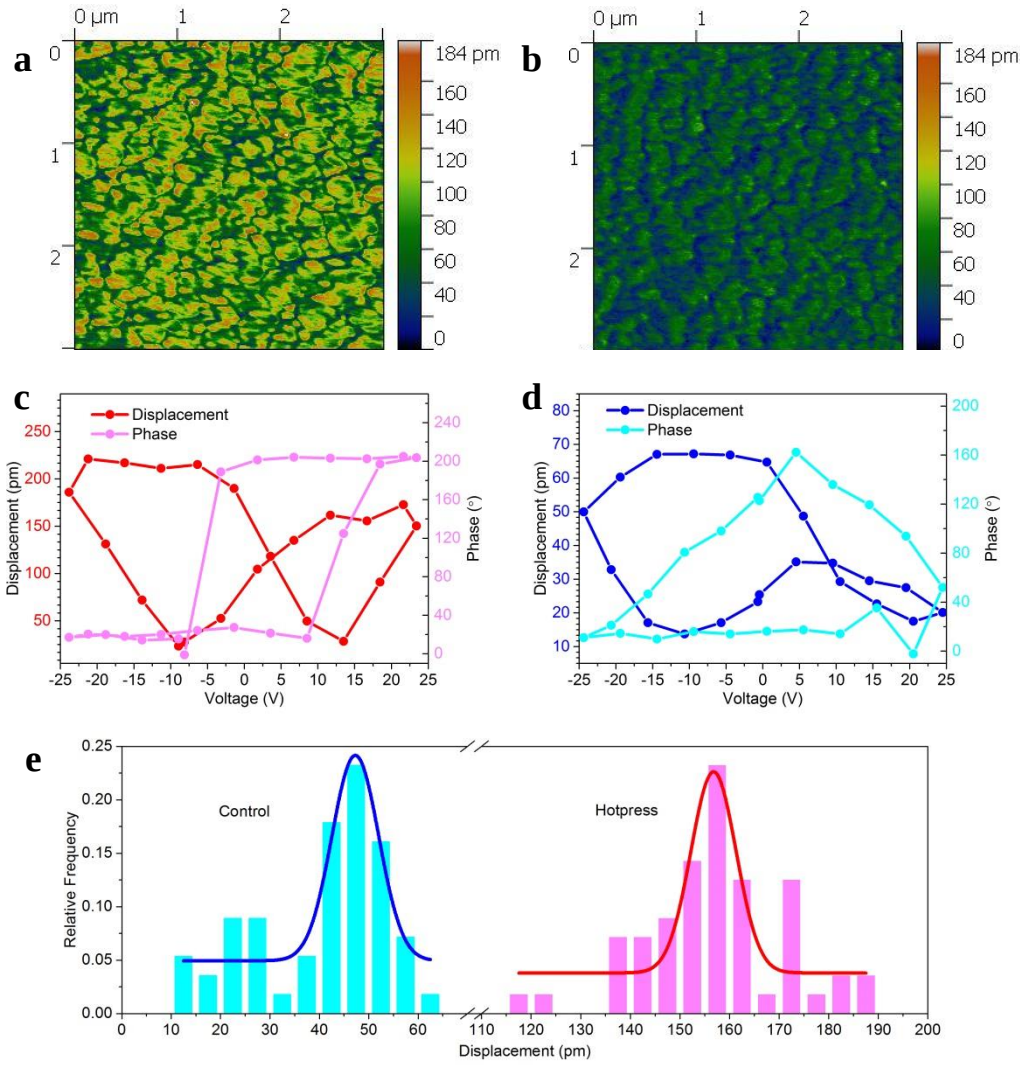

Figure 2.9 (a,b) PFM amplitude images of (a) hot-pressed and (b) air-dried samples. A conductive tip was used to apply a constant bias of 9.4 V to induce local ME displacement while imaging (see corresponding height and phase images in appendix Figure A1). (c,d) PE butterfly loops of (c) hot-pressed and (d) control cellulose films elucidated using SS-PFM. The red and blue dots are the hysteresis loops representing the bias induce amplitude displacement. The pink and cyan dots represent phase changes corresponding to the hysteresis loops. (e) histograms of bias induced amplitude displacement at applied voltage of -25 V during SS-PFM measurements.

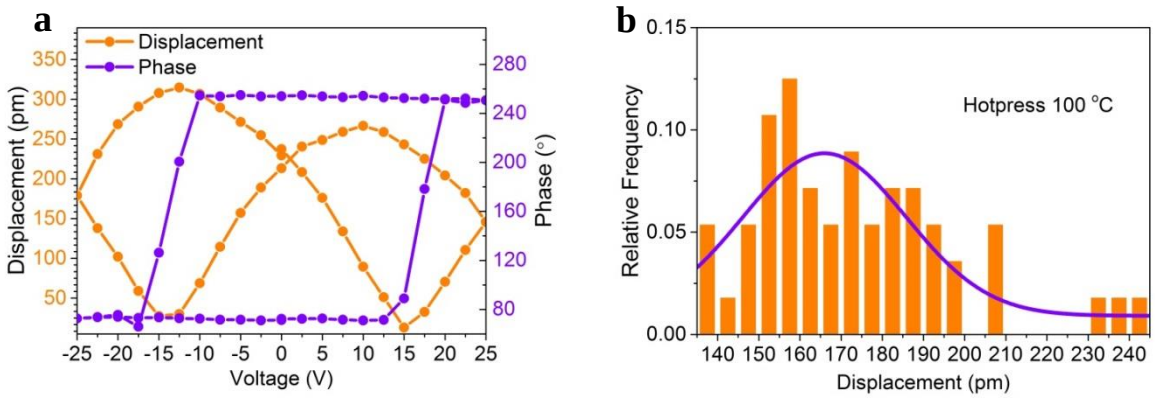

Figure 2.10. (a) local PE response of hot-pressed cellulose film elucidated using SS-PFM. The orange dots are the hysteresis loops representing the bias induce amplitude displacement. The violet dots represent phase changes corresponding to the hysteresis loops. (b) histograms of bias induced amplitude displacement at applied voltage of -25 V during SS-PFM measurements.

Also, due to the surface charge of cellulose films the electrostatic effect may slightly influence the displacement values. The effect is not caused by cellulose *per se* but is attributed to the residual salt. Because the cellulose was dissolved using LiCl/DMAc solvent system and the salt was not 100% eliminated by washing, it is possible that a small amount of surface charge is present. Despite our interpretation the system is complex and as yet the exact mechanisms are unclear.

2.4. Conclusion

In conclusion, ME composites were fabricated using cellulose as the active PE material, leading to considerable α_{ME} coefficients of 1.41 V cm^{-1} Oe^{-1}. The cellulose and improvement of its crystallinity, PE properties and consequently the ME output was easily achieved using simple and inexpensive solution processing methods. A Fano-like resonance, consisting of an anti-resonance dependence on the magnetic field strength, appeared to be due to the unique chemical structure and properties of the cellulose. The asymmetric Fano-resonance profile demonstrated that it was possible to shift the ME output voltage from a peak value to zero sharply, enabling for accurate control of a relatively broad range of power output by easily manipulating the applied magnetic field. Further studies on the resonance line shape will be fundamental for understanding cellulose-based magnetoelectric composites. The ME composites also exploit the current demand for cellulose as a renewable and cheap material, as well as biocompatible and biodegradable properties[41] that, for example, will progress the development of ME composites in a range of applications. In doing so, the study successfully demonstrates the concept of using natural occurring PE biopolymers though it is anticipated that other PE proteins and biological materials *(e.g.* collagen) will importantly find their way into ME composites.

Note

The manuscript based on **Chapter 2.** is published as a journal article with citation as below:

Zong, Y.; Zheng, T.; Martins, P.; Lanceros-Mendez, S.; Yue, Z.; Higgins, M. J. *Cellulose-based magnetoelectric composites*. Nature Communications **2017**, *8*, 38.

2.5. References

1 Spaldin, N. A. & Fiebig, M. The Renaissance of Magnetoelectric Multiferroics. *Science* **309**, 391-392, (2005).

2 Eerenstein, W., Mathur, N. D. & Scott, J. F. Multiferroic and magnetoelectric materials. *Nature* **442**, 759-765, (2006).

3 Ma, J., Hu, J., Li, Z. & Nan, C.-W. Recent Progress in Multiferroic Magnetoelectric Composites: from Bulk to Thin Films. *Adv. Mater.* **23**, 1062-1087, (2011).

4 Wang, Y. *et al.* An Extremely Low Equivalent Magnetic Noise Magnetoelectric Sensor. *Adv. Mater.* **23**, 4111-4114, (2011).

5 Suchtelen, J. v. *Philips Res. Rep.* **27**, 28-37, (1972).

6 Silva, M. *et al.* Optimization of the Magnetoelectric Response of Poly(vinylidene fluoride)/Epoxy/Vitrovac Laminates. *ACS Appl. Mater. Interfaces.* **5**, 10912-10919, (2013).

7 Zhai, J., Dong, S., Xing, Z., Li, J. & Viehland, D. Giant magnetoelectric effect in Metglas/polyvinylidene-fluoride laminates. *Appl. Phys. Lett.* **89**, 083507, (2006).

8 Dong, S., Zhai, J., Li, J. & Viehland, D. Near-ideal magnetoelectricity in high-permeability magnetostrictive/piezofiber laminates with a (2-1) connectivity. *Appl. Phys. Lett.* **89**, 252904, (2006).

9 Martins, P. & Lanceros-Méndez, S. Polymer-Based Magnetoelectric Materials. *Adv. Funct. Mater.* **23**, 3371-3385, (2013).

10 Nan, C. W., Li, M. & Huang, J. H. Calculations of giant magnetoelectric effects in ferroic composites of rare-earth–iron alloys and ferroelectric polymers. *Phys. Rev. B* **63**, 144415, (2001).

11 Lee, B. Y. *et al.* Virus-based piezoelectric energy generation. *Nat Nano* **7**, 351-356, (2012).

12 Fukada, E. On the piezoelectric effect of silk fibers. *J. Phys. Soc. Jpn.* **11**, 1301, (1956).

13 Eiichi, F. & Iwao, Y. Piezoelectric Effects in Collagen. *Japanese Journal of Applied Physics* **3**, 117, (1964).
14 Fukada, E. Piezoelectricity as a fundamental property of wood. *Wood Science and Technology* **2**, 299-307.
15 Jarvis, M. Chemistry: Cellulose stacks up. *Nature* **426**, 611-612, (2003).
16 Fukada, E. Piezoelectricity of Wood. *J. Phys. Soc. Jpn.* **10**, 149-154, (1955).
17 Csoka, L. *et al.* Piezoelectric Effect of Cellulose Nanocrystals Thin Films. *ACS Macro Lett.* **1**, 867-870, (2012).
18 Nogi, M. & Yano, H. Transparent Nanocomposites Based on Cellulose Produced by Bacteria Offer Potential Innovation in the Electronics Device Industry. *Adv. Mater.* **20**, 1849-1852, (2008).
19 Zhu, H. *et al.* Biodegradable transparent substrates for flexible organic-light-emitting diodes. *Energy Environ. Sci.* **6**, 2105-2111, (2013).
20 Kim, J., Yun, S. & Ounaies, Z. Discovery of Cellulose as a Smart Material. *Macromolecules* **39**, 4202-4206, (2006).
21 Jung-Hwan, K., Ki-Ju, Y., Joo-Hyung, K. & Jaehwan, K. Mechanical stretching effect on the actuator performance of cellulose electroactive paper. *Smart Mater. Struct.* **18**, 055005, (2009).
22 Srinivasan, G. Magnetoelectric Composites. *Annu. Rev. Mater. Res.* **40**, 153-178, (2010).
23 McCormick, C. L., Callais, P. A. & Hutchinson, B. H. Solution studies of cellulose in lithium chloride and N,N-dimethylacetamide. *Macromolecules* **18**, 2394-2401, (1985).
24 Dinesh Kumar, S., Ramesh, G. & Subramanian, V. Enhanced self-biased direct and converse magnetoelectric effect in Pb(In1/2Nb1/2)O3–PbTiO3/NiFe2O4 bi-layer laminate composite. *Journal of Materials Science: Materials in Electronics* **26**, 2682-2687, (2015).
25 Brian, J. R., Clint, C., Sergei, V. K. & Roger, P. Dual-frequency resonance-tracking atomic force microscopy. *Nanotechnology* **18**, 475504, (2007).
26 Zhai, J., Xing, Z., Dong, S., Li, J. & Viehland, D. Magnetoelectric Laminate Composites: An Overview. *J. Am. Ceram. Soc.* **91**, 351-358, (2008).
27 Shi, Z. *et al.* Magnetoelectric sensor with miniature universal tunable bias magnetic circuit. *Appl. Phys. Lett.* **103**, 032903, (2013).
28 Gonçalves, R. *et al.* Synthesis of highly magnetostrictive nanostructures and their application in a polymer-based magnetoelectric sensing device. *Eur. Polym. J.* **84**, 685-692, (2016).
29 Shuxiang, D., Jie-Fang, L. & Viehland, D. Longitudinal and transverse magnetoelectric voltage coefficients of magnetostrictive/piezoelectric laminate composite: theory. *IEEE Trans. Ultrason., Ferroelect., Freq. Control.* **50**, 1253-1261, (2003).

30 Yun, S., Chen, Y., Nayak, J. N. & Kim, J. Effect of solvent mixture on properties and performance of electro-active paper made with regenerated cellulose. *Sensors Actuators B: Chem.* **129**, 652-658, (2008).
31 Gyu-Young, Y., Joo-Hyung, K. & Jaehwan, K. Dielectric and polarization behaviour of cellulose electro-active paper (EAPap). *J. Phys. D: Appl. Phys.* **42**, 082003, (2009).
32 Sungryul, Y., Sangdong, J., Gyu-Young, Y. & Jaehwan, K. Electrically aligned cellulose film for electro-active paper and its piezoelectricity. *Smart Mater. Struct.* **18**, 117001, (2009).
33 Fan, S. & Joannopoulos, J. D. Analysis of guided resonances in photonic crystal slabs. *Phys. Rev. B* **65**, 235112, (2002).
34 Luk'yanchuk, B. *et al.* The Fano resonance in plasmonic nanostructures and metamaterials. *Nat Mater* **9**, 707-715, (2010).
35 Bichurin, M. I. *et al.* Resonance magnetoelectric effects in layered magnetostrictive-piezoelectric composites. *Phys. Rev. B* **68**, 132408, (2003).
36 Nguyen, T. T., Mininger, X., Bouillault, F. & Daniel, L. Finite Element Harmonic Modeling of Magnetoelectric Effect. *IEEE Trans. Magn.* **47**, 1142-1145, (2011).
37 Gerken, M. Resonance line shape, strain and electric potential distributions of composite magnetoelectric sensors. *AIP Adv.* **3**, 062115, (2013).
38 Hasanyan, D. *et al.* Theoretical and experimental investigation of magnetoelectric effect for bending-tension coupled modes in magnetostrictive-piezoelectric layered composites. *J. Appl. Phys.* **112**, 013908, (2012).
39 Pedersoli Júnior, J. L. Effect of cellulose crystallinity on the progress of thermal oxidative degradation of paper. *J. Appl. Polym. Sci.* **78**, 61-66, (2000).
40 Liu, Y., Zhang, Y., Chow, M.-J., Chen, Q. N. & Li, J. Biological Ferroelectricity Uncovered in Aortic Walls by Piezoresponse Force Microscopy. *Phys. Rev. Lett.* **108**, 078103, (2012).
41 Klemm, D., Heublein, B., Fink, H.-P. & Bohn, A. Cellulose: Fascinating Biopolymer and Sustainable Raw Material. *Angew. Chem. Int. Ed.* **44**, 3358-3393, (2005).

Chapter 3. Nanocrystalline Cellulose for Anisotropic Magnetoelectric Composites

3.1. Introduction

ME materials that enable magnetic to electrical signal conversion are promising for energy harvesting[1], magnetic sensing[2] and non-volatile memory storing[3] applications. PE polymers provides the possibility to fabricate more flexible and lower-cost ME composites. Generally, polymeric ME composites are easier to process and more flexible than ME ceramics.[4,5] Significant enhancement of the ME effect can be achieved through modification of a polymer matrix to improve its piezoelectricity. For example, the highest α_{ME} reported so far is observed in a ME laminate combining chain-end crosslinking functionalized P(VDF-TrFE), with a high performance MS film, Metglas.[6]

Accordingly, due to their high α_{ME}, PVDF and its copolymers have almost exclusively been used in ME composites and this remains the current situation despite an inventory of unexplored PE polymers such as naturally occurring biomolecules[7,8] that were first demonstrated only recently by our group (**Chapter 2**)[9]. In this work, regenerated cellulose in ME composites exhibited a giant α_{ME} (>1 V cm^{-1} Oe^{-1}) under relatively weak magnetic field, leading to the discovery of new fundamental ME properties as well as access to cheap, renewable and degradable materials for

development of ME devices. Therefore, despite having lower PE coefficients, polymers other than PVDF have potential to bring added value properties and functions, and cellulose is no exception in this regard.

Cellulose is known to come in many different structural forms and degrees of crystallinity, including a wide variety of easily synthesized nanocrystalline cellulose (CNC) such as nanofibrils, nanowhiskers,[10-12] and nanospheres[13,14], which are expected to offer a unique opportunity to manipulate the fabrication and operation of ME devices.

CNC is the structural component of cellulose fibrils which coexists with amorphous cellulose in plant tissues.[10,11] High aspect ratio CNC whiskers can be prepared from different cellulose resources by using acid hydrolysis method to dissolve the amorphous cellulose section.[11,12] Due to its unique mechanical and self-assembly properties, CNC has been widely used as a supporting template or filler in composites.[15-19] In addition, its low dimensional (1D) nanostructure can be fabricated to form aligned structures that are sensitive to directional changes, which is effectively confirmed in natural wood sheets showing anisotropic piezoelectricity[20].

In this chapter, different CNC were synthesized and used in ME composites to enhance the ME effect and impart new functions in biopolymer-based ME composites. We take advantage of aligned CNC nanowhiskers to demonstrate an anisotropic ME effect, which as yet has not been demonstrated *via* the PE component in polymer-based ME composites and gives rise to significant increases in the output

voltage by an order of magnitude for anisotropic ME devices with vector-sensing capability.

3.2. Experimental Methods

CNC Preparation: CNC was prepared *via* acid hydrolysis using 65 wt% H_2SO_4. To prepare CNC whiskers, 4g α-cellulose (Sigma-Aldrich C8002) was blended with 30 mL H_2SO_4. A pre- swelling treatment was developed to produce spherical CNC. Firstly, 4g of α-cellulose was immersed in 10 mL distilled (DI) water overnight and then the acid concentration was adjusted by adding 80 wt% H_2SO_4 into the cellulose slurry under ice bath conditions until the target concentration is reached. The hydrolysis reaction took place under 55 ˚C with constant stirring at 1,400 rpm for 40 min. To cease the reaction, 250 mL iced DI water is added, and then the resultant suspension was washed by centrifugation at ~10,000 rpm for several times until the upper layer became turbid. The obtained CNC samples were viscous aqueous dispersion (~3 wt%).

CNC Crystalline Characterization: X-ray diffraction (XRD) was performed on the raw material and the freeze-dried CNC powder using a GBC MMA XRD (λ = 1.54Å) in the range of 10-45˚. The voltage, current and scanning speed were set as −40 kV, 25mA and 1˚ min^{-1}, respectively. The Fourier Transform Infrared Spectroscopy (FT-IR) spectrum was performed on a Shimadzu AIM8000 FT-IR spectrometer. The

raw materials and freeze-dried CNC powder were measured using a KBr-pellet method in the range of 700-4000 $cm^{-1.}$

CNC Film Casting: For non-aligned films, the gel-like CNC was poured into a casting well of 0.8 mm in depth, which was then immersed in a 0.5 M $CaCl_2$ solution for 5 min, followed by DI water washing. Then the film casting process was conducted under room temperature (20 ˚C) or 80 ˚C in vacuum oven. To develop aligned CNC whisker film, the CNC whisker aqueous dispersion was added into a small glass vial comprising a flexible PET film that lined the inside of the vial and enabled subsequent removal of the CNC whisker film. The vial was sealed and placed in a home-made spinner **(Figure 3.1)**, running 0.5 h at ~1,000 rpm. The details of the alignment process can be found in a schematic demonstration in **Figure 3.9**. After the CNC whiskers were well aligned, the PET film was removed and transferred to $CaCl_2$ solution, following the aforementioned method to dry and cast films.

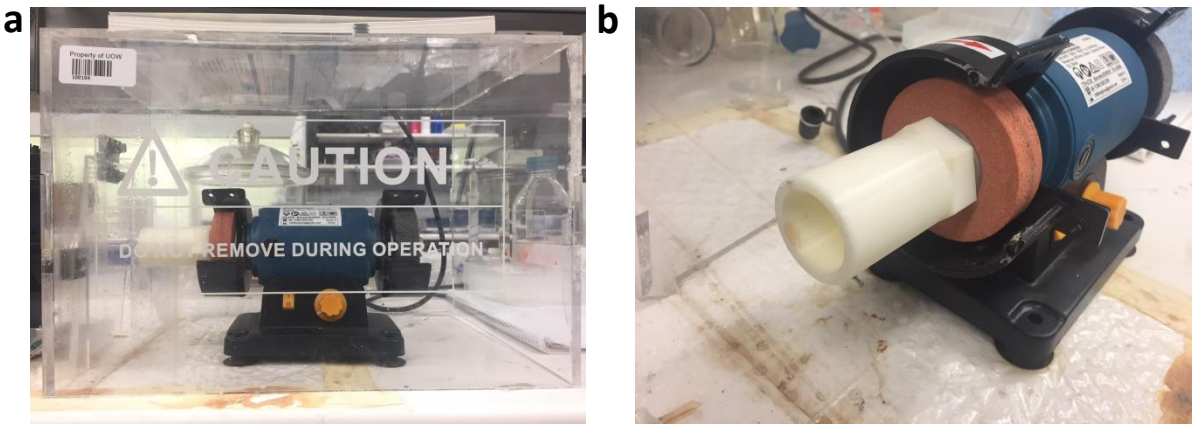

Figure 3.1. (a) Overview of the home made spinner in a safety box and (b) the vial hold of the spinner.

Tensile test: Tensile strengths and Young's Moduli were tested using a Shimadzu EZ-TEST system with a 50 N testing cell. The samples were cut into strips of 5mm in width and 20 mm in length. The thickness of each film was measured by using micrometer.

ME Laminate Composite Fabrication: The CNC films were sputter coated with 30 nm gold layers on both sides as contact electrodes (the sputtering is conducted with 1 min on and 0.5 min off cycles to avoid degradation) and were then cut into a 40 mm × 8 mm rectangular using a scalpel. To fabricate the ME laminate composites, a 32 mm × 6 mm Metglas 2605 SA1 tape was glued onto the centre of the cellulose film using commercial Devcon epoxy (**Figure 3.2a**). To ensure even distribution, the epoxy was pre-heated to 60 ℃ to improve the liquidity. Copper wires were then connected to the laminate *via* the gold electrodes using silver paint.

Bulk ME Effect Measurement: An alternating Helmholtz coil was used to apply a magnetic ac field at 0.4 Oe with frequencies from 20.1 - 92.1 kHz. A separate electromagnet was use to apply magnetic dc fields with strengths in the range of ~0.5-30 Oe and both the ac and dc magnetic fields were applied simultaneously along the length direction of the ME laminate composites. The induced ME output voltage was recorded using a model SR8 10 DSP lock-in amplifier (**Figure 3.2b**).

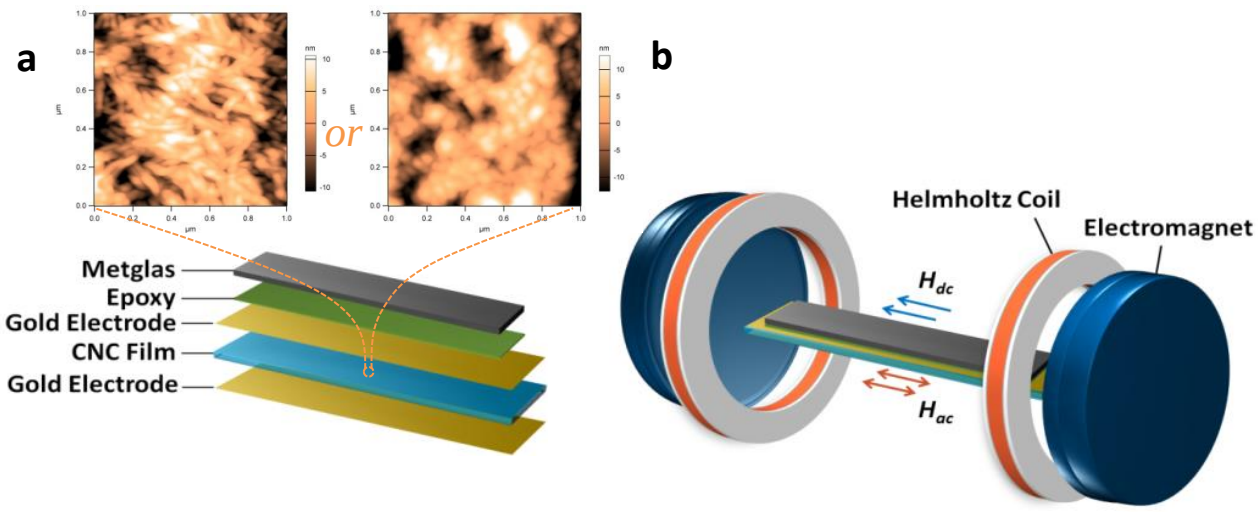

Figure 3.2. (a) Schematic view of CNC based ME laminate structure. CNC nanowhiskers and nanospheres were used to cast films. (b) Schematic view of the bulk system for ME voltage measurement. The output voltage was collected from the interface gold electrodes and monitored as root mean square (RMS) values using a lock-in amplifier.

Thermogravimetric Analysis (TGA): TA Instrument SDT Q600 thermal analysis system was employed for thermogravimetric analysis. The measurements were run under an atmosphere with 9:1 oxygen/nitrogen flows from 35~425 ℃ at a ramping rate of 10 ℃ min^{-1}.

Piezoresponse Force Microscopy (PFM): The local PE response of CNC was measured with an MFP-3D Atomic Force Microscope (Asylum Research, Santa Barbara, US) using PFM. A conductive tip (Olympus OMCL-AC240TM) with Pt/Ti coating, resonant frequency of 70 kHz and spring constant of ~2.0 N m^{-1} were used. The sensitivity of the tip was calibrated on a glass slide based on a force curve measurement. The PFM height, amplitude and phase images were obtained in Dual

AC Response Tracking (DART) mode[21] with contact resonant frequency of ~ 260 kHz. The PE response was measured as the first-harmonic of a bias-induced tip deflection: $d = d_0 + A\cos(\omega t + \varphi)$, where d_0 is the equilibrium position of the tip; A is the amplitude and ω is the frequency of applied bias; φ is the phase yielded information on the polarization direction below the tip. To study the polarization switching dynamics, switching spectroscopy-PFM (SS-PFM) was used to obtain the local PE hysteresis loop. For each laminate sample, SS-PFM measurements were acquired across a $3 \times 3\ \mu m^2$ area by applying a bias at least 5 positions on the sample. The voltage during the SS-PFM measurements was applied in the range of ± 29 V with a frequency of 0.5 Hz, which was sufficient to reversibly switch the polarization component. To enable this, the PFM instrumentation was modified by connecting an external amplifier to increase the upper limit of output signal to ± 30V. All SS-PFM loops were acquired in off-state and a driving amplitude was set to 200 mV for all PFM measurements.

3.3. Results and Discussion

3.3.1. Nanostructure and Crystallinity of CNCs

Two types of CNC, namely the nanowhiskers and nanospheres were synthesized to fabricate the ME laminates (**Figure 3.3**). Spherical CNC has been reported elsewhere, produced by mixed acid combined with ultrasonic treatment.[13,14] In this study,

nanowhiskers were obtained from direct acid hydrolysis (**Figure 3.3a**) while a newly introduced pre-swelling treatment before the acid hydrolysis produces the nanospheres (**Figure 3.3b**). Due to the change of configuration, the freeze dried nanowhiskers and nanospheres have a different appearance (**Figure 3.3c**). X-ray diffraction (XRD) (**Figure 3.3d**) and Fourier transform infrared spectroscopy (FTIR) (**Figure 3.4**) spectra reveal the nanospheres possess a crystalline II lattice structure in contrast to nanowhiskers and raw material (α-cellulose) that both show crystalline I lattice structures. In particular, cellulose crystalline I is ubiquitous and widely observed in earlier studies on CNC,[10,13,14] however, the existence of crystalline II in CNC is a serendipitous finding yet to be reported. A conversion from the crystalline I to II is explained by the prior swelling treatment that weakens the interaction between polymer chains and leads to rearrangement of the cellulose polymeric matrix into spherical-like structures.

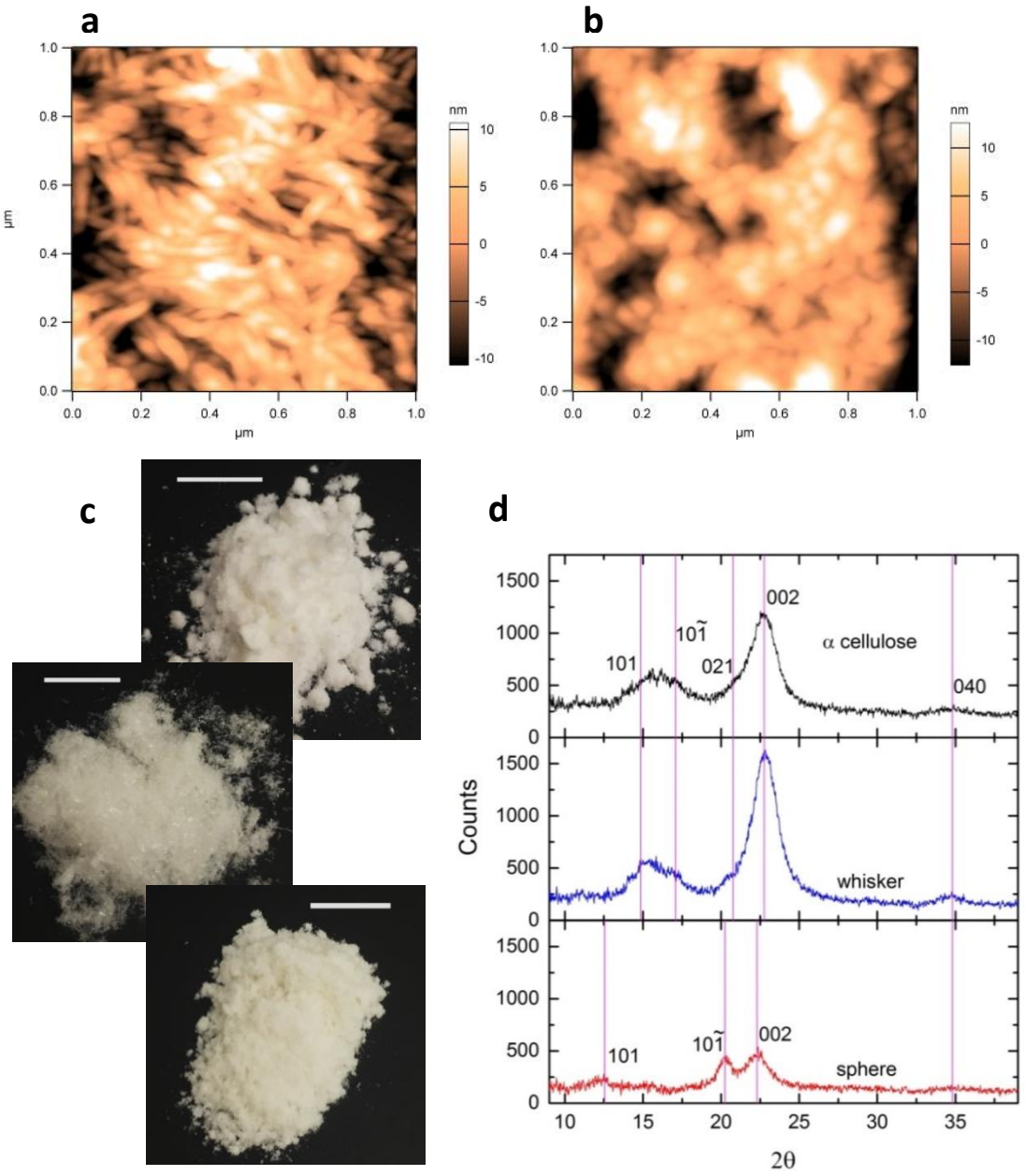

Figure 3.3. (a,b) AFM height images of whisker and spherical CNC, the scanning size was 1×1 µm. (c) α-cellulose powder, freeze-dried CNC whiskers and spheres (top-down) corresponding to the left XRD spectra (scale bar=1 cm). (d) XRD spectra of the raw material and resulted CNCs. The raw material and whisker CNC has interference rising at diffraction angles 2θ=14.9˚, 17.6˚, 20.7˚ and 22.7˚ corresponding to lattice (101), (10$\tilde{1}$), (021) and (002), which is the typical XRD spectrum for cellulose crystalline I. The spherical nanocrystal is mainly constructed by cellulose crystalline II, of which the interference of lattice (101), (10$\tilde{1}$), and (002) were seen at 2θ=12.5˚, 20.2˚and 22.3˚.

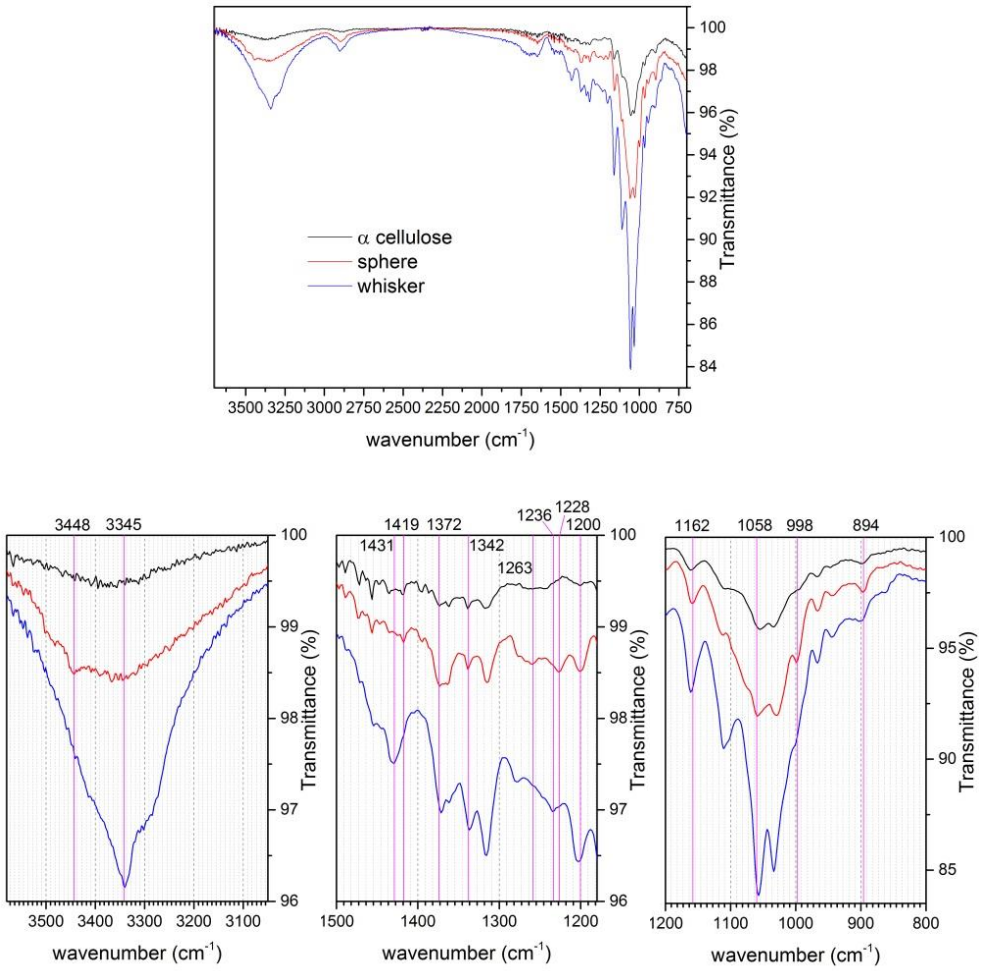

Figure 3.4. FTIR spectra of α-cellulose, CNC whisker and sphere. The features of **nanowhisker** are all corresponding to cellulose crystal I,[22] and the features of **nanosphere** are all corresponding to cellulose crystal II,[22] as displayed in **Table 3.1**.

Table 3.1. FT-IR features of nanowhiskers and nanospheres, as well as the corresponding groups.

Nanowhisker	Nanosphere	Corresponding Groups
898 cm^{-1}	894 cm^{-1}	stretching COC at glycosidic linkage; stretching COC, CCO and CCH at C5 and C6.
N/A	998 cm^{-1}	stretching CO at C6.
1058 cm^{-1}	N/A	stretching CO at C3 and stretching CC.
1165 cm^{-1}	1162 cm^{-1}	stretching at glycosidic linkage.
1202&1236 cm^{-1}	1200&1228 cm^{-1}	bending COH in plane at C6.
N/A	1263 cm^{-1}	bending COH in plane at C2 and C3.
1372 cm^{-1}	N/A	bending CH.
1431 cm^{-1}	1419 cm^{-1}	bending CH (sym) at C6.
3345 cm^{-1}	3448 cm^{-1}	stretching OH in hydrogen bonding.

The PE property of cellulose is critically dependent on the degree of crystallinity. One reliable evaluation standard is the crystallinity index (CI) determined by the XRD interference intensity and expressed by the following equation[23]:

$$CI = \frac{(I_{002} - I_{am})}{I_{002}} \quad (3.1)$$

where the intensity of (002) peak at 22.7 and 22.3 is assigned to cellulose crystalline I and II, respectively. I_{am} is the intensity of the amorphous component at 2θ of 18° for

crystalline I and 16˚ for crystalline II.[23] Compared to the raw material, the CI of nanowhiskers and nanospheres increases from 68.1 % to 89.3 % and 80.5 %, respectively. The increased crystallinity degree of both whisker and spherical CNC is attributed to the reduction of amorphous cellulose regions, as a result of acid-induced polymer degradation.

3.3.2. CNC-Based ME Laminate Composites

To fabricate the CNC-based ME composites, the nanowhiskers and nanosphere dispersions (~3 wt %) were drop casted as films with additional Ca^{2+} to stabilize the network and then air-dried under room temperature (RT, 20 ℃) or alternatively vacuum-dried under 80 ℃ in an attempt to remove residual water. The CNC films were then fixed to MS Metglas tape (see methods section) and coated with a gold surface electrodes to produce ME laminate composites, as shown in **Figure 3.2**. Due to the fast evaporation of water, severe cracking is observed in the nanospheres films developed under 80 ˚C and therefore were not considered for further ME measurements. The performance of ME laminates based on three differently prepared CNC films (*i.e.* nanowhiskers under RT and 80 ˚C, and nanospheres under RT) is evaluated using a dynamic ME measurement method whereby an alternating magnetic field (H_{ac}) was superimposed on a constant DC magnetic field (H_{dc}) to generate an ME output voltage that was measured as a function of the magnetic field strength and frequency. Based on this method, the ME voltage coefficient was evaluated using the following equation:[24]

$$\alpha_{\mathrm{ME}} = \frac{V_{\mathrm{ME}}}{T \times H_{ac}} \tag{3.2}$$

where V_{ME} is the actual voltage output collected from surface electrodes, T is the thickness of PE film and H_{ac} is the strength of the alternating magnetic field.

Firstly, the H_{ac} and H_{dc} strength were fixed and the ME output voltage was measured as the function of H_{ac} frequency change. The frequency-dependent ME effect and H_{dc} dependent curves of α_{ME} were displayed in **Figure 3.5a, b**. The resonance enhancement phenomenon was observed in all the samples, that is, when the resonance frequency of the MS film encountered the H_{ac} frequency, the mechanical strain was dramatically amplified thus giving a significant increase in the ME output voltage. The resonance frequency (f_{r}) of the MS film, which depends on several factors, including its density (ρ), Young's modulus (E) and the length (L) along the magnetic field, was calculated using the following equation:

$$f_r = 1/2L \times \sqrt{E/\rho} \tag{3.3}$$

For Metglas, E=100~110 GPa and ρ= 7.18×10^3 kg m^{-3}. In our case L=32 mm, thus the calculated theoretical f_r of 58.31~61.16 kHz was very close to the experimental data shown in **Figure 3.5a**. To more accurately determine the ME output voltage, the frequency dependent curves in **Figure 3.5a, b** were fitted to a modified Maxwell equation:

$$V(\omega) = A\left|\frac{\omega^2 - 2i\delta_a\omega_a\omega - \omega_a^2}{\omega^2 - 2i\delta_r\omega_r\omega - \omega_r^2}\right| + a\omega + b \tag{3.4}$$

where A is the amplitude constant. $\omega_r=2\pi f_r$ is the resonance frequency and $\omega_a=2\pi f_a$ is the anti-resonance frequency. δ_r and δ_a are the damping constants for the resonance and anti-resonance, respectively. a is the constant corresponding to a linear background noise and b is the factor fitting the imaginary section to experimental data. The fitting results (dashed line in **Figure 3.5a**) show good agreement with the experimental data (dots) and the same equation (3) is also used to fit the frequency-dependent curves measured under different H_{dc} strength. The fitting parameters are provided in **Tables 3.2, 3.3 and 3.4**. The peak values of the resonance enhanced α_{ME} corresponding to different H_{dc} strength are given in **Figure 3.5b**. The highest output voltage of 2.98 mV was obtained for the nanospheres, with a calculated α_{ME} of 2.33 V cm^{-1} Oe^{-1}, followed by the nanowhisker sample vacuum dried under 80 ˚C (α_{ME} =1.40 V cm^{-1} Oe^{-1}) and then the air-dried nanowhisker sample (α_{ME} =0.75 V cm^{-1} Oe^{-1}). These α_{ME} are higher than those previously recorded for the regenerated cellulose[9] in **Chapter 2** and a comparison of all values are provided in **Table 3.5**.

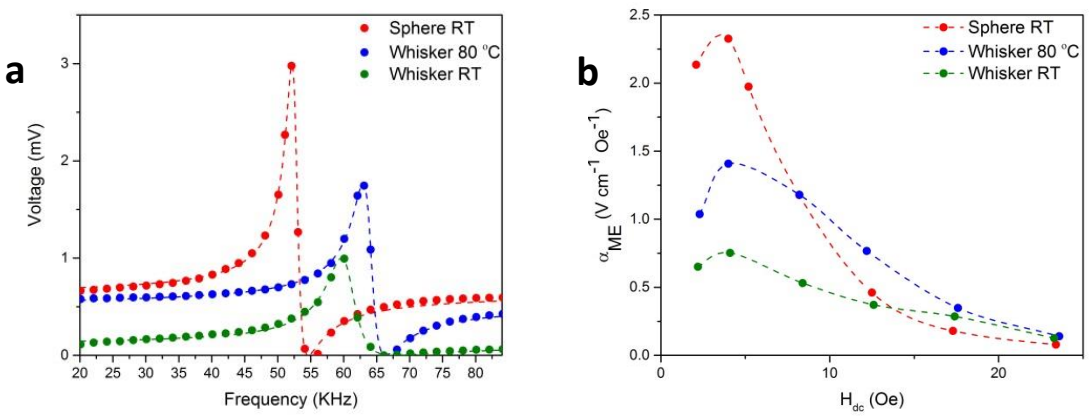

Figure 3.5. (a) ME output voltage as a function of H_{ac} frequency under H_{dc}=4.0 Oe and H_{ac}=0.4 Oe. The experimental data (dots) were fitted to equation (3.4) and the results were shown as dashed lines. (b) Resonance enhanced ME voltage coefficient as a function of H_{dc}, and the H_{ac} strength was fixed as 0.4 Oe.

Table 3.2. Fitting parameters (imaginary section) of equation (3.4) for anti-resonance frequency effect of room temperature aired nanospheres ME laminate under different H_{dc} strength.

H_{dc} (Oe)	A (mV)	f_r (kHz)	f_a (kHz)	δ_r	δ_a
2.1	0.3333	51.9595	55.7657	-0.0224	0.1280
4.0	0.5344	52.7003	55.7814	-0.0190	0.0642
8.2	0.3052	54.2317	55.9816	-0.0153	0.0538
12.5	0.1490	55.0440	56.0966	-0.0115	0.0373
15.8	0.0872	55.7367	56.5707	-0.0129	0.0196
23.4	0.0688	55.8827	57.5200	-0.0026	0.0124

Table 3.3. Fitting parameters (imaginary section) of equation (3.4) for anti-resonance frequency effect of room temperature aired nanowhiskers ME laminate under different H_{dc} strength.

H_{dc} (Oe)	A (mV)	f_r (kHz)	f_a (kHz)	δ_r	δ_a
2.2	0.2566	64.2375	69.2374	-0.0335	0.0479
4.1	0.2798	60.6186	67.1118	-0.0418	0.0473
12.6	0.1003	65.1630	54.0654	0.0344	-0.0393
17.4	0.0922	65.3815	59.6550	0.0272	-0.0529
23.3	0.0754	66.2220	63.0019	0.0327	-0.0206

Table 3.4. Fitting parameters (imaginary section) of equation (3.4) for anti-resonance frequency effect of 80 ˚C dried nanowhiskers ME laminate under different H_{dc} strength.

H_{dc} (Oe)	A (mV)	f_r (kHz)	f_a (kHz)	δ_r	δ_a
2.3	0.3622	64.1285	65.8250	-0.0194	0.0452
4.0	0.5277	63.9581	65.9886	-0.0242	0.0491
8.2	0.3657	64.3038	66.8993	-0.0235	0.0578
12.2	0.2743	64.8638	67.4460	-0.0247	0.0473
17.5	0.2029	65.5312	66.9661	-0.0200	0.0199
23.6	0.1450	65.9730	66.6561	-0.0204	0.0017

Table 3.5. The thicknesses and mechanical properties of PE CNC films and the corresponding performance of CNC ME laminates.

Piezoelectric Phase	Casting Temp. (˚C)	Testing Angle (˚)	Thickness (μm)	V_{peak} (mV)	α_{ME} (V cm^{-1} Oe^{-1})
Nanospheres	20	N/A	32±4	2.98	2.33
Nanowhiskers (Random)	20	N/A	33±3	0.99	0.75
	80	N/A	30±4	1.75	1.40
Nanowhiskers (Aligned)	80	90	29±3	2.23	1.92
		45	28±3	1.10	0.99
		0	29±3	0.63	0.55

Moreover, a Fano-resonance appeared in all the frequency-dependent profiles, consisting of a resonance peak and accompanied by an anti-resonance peak where the ME output voltage sharply dropped down to zero (**Figure 3.6**). This anti-resonance effect was clearly different to typical symmetrical Lorentzian resonance profiles seen to date in artificial polymeric ME laminates[25] and only recently observed in regenerated cellulose based ME composites,[9] making it seemingly unique to the properties of cellulose. The CNC nanowhisker air-dried sample under RT showed a symmetric Lorentzian resonance profile at H_{dc}=8.2 Oe. However, at H_{dc}<8.2 Oe a Fano-resonance with anti-resonance peak appeared at a frequency higher than the resonance frequency though oppositely occurred at a lower frequency when H_{dc}>8.2 Oe (**Figure 3.6a-c**). This Fano-resonance-dependence on the H_{dc} was very similar to that previously observed for regenerated cellulose-based ME composites[9] though differs to the behaviour of the other two CNC films. For instance, the CNC

nanospheres (**Figure 3.6d-f**) and nanowhiskers vacuum-dried samples under higher temperatures at 45 ˚C or above (**Figure 3.6g-i**) only show a Fano-resonance with anti-resonance at frequencies greater than the resonance peak and remarkably no symmetrical Lorentzian profile was observed at any applied H_{dc}. As discussed in the previous chapter for regenerated cellulose-based ME composites, it was suggested that water content, consisting of free/bound residual water, had an effect on the frequency-dependent curves, including the Fano-resonance profiles.[9] Thermogravimetric analysis (TGA) indicated the air-dried nanowhiskers contained the highest amount of water followed by vacuum-dried nanowhiskers, with the least water content in air-dried nanospheres (**Figure 3.7**). Due to the high crystallinity degree and limited porosity within single nanowhiskers, the CNC inter-nanowhisker space was expected to facilitate only free water content, giving rise to resonance profiles similar to those of regenerated cellulose which was shown to contain the most water when air-dried. Further removal of free water by vacuum heating leaded to a phenomena whereby no symmetrical resonance profile, and only a Fano-resonance persists, at all H_{dc} and is unique to CNC. Interestingly, however, the CNC nanospheres were also air-dried yet show a similar ME response to the heated nanowhiskers samples (**Figure 3.6g-i**). This may be due to nanospheres that can more easily be compacted, *e.g.* where smaller particles fill in the interstices, producing a film structure that inherently limits the available space for free water, as supported by TGA results (**Figure 3.7**). The effect of water content was also seen on the damping constants related to the quality factor of the enhanced ME resonance. The CNC

nanowhisker air-dried sample, containing most residue water, showed the broadest peak or lowest quality factor, with damping constant of δ_r=-0.0418 under H_{dc}=4.0. In contrast, the CNC nanospheres and heated nanowhisker samples with lower water content showed narrower resonance peaks, with significantly lower damping constants of δ_r=-0.0190 and δ_r=-0.0242, respectively (**Tables 3.2, 3.3 and 3.4**). Therefore, the presence of free water in these CNC and cellulose in general effects the ME resonance profile, presumably through changes in the mechanical properties and/or ion migration during electrical polarization.

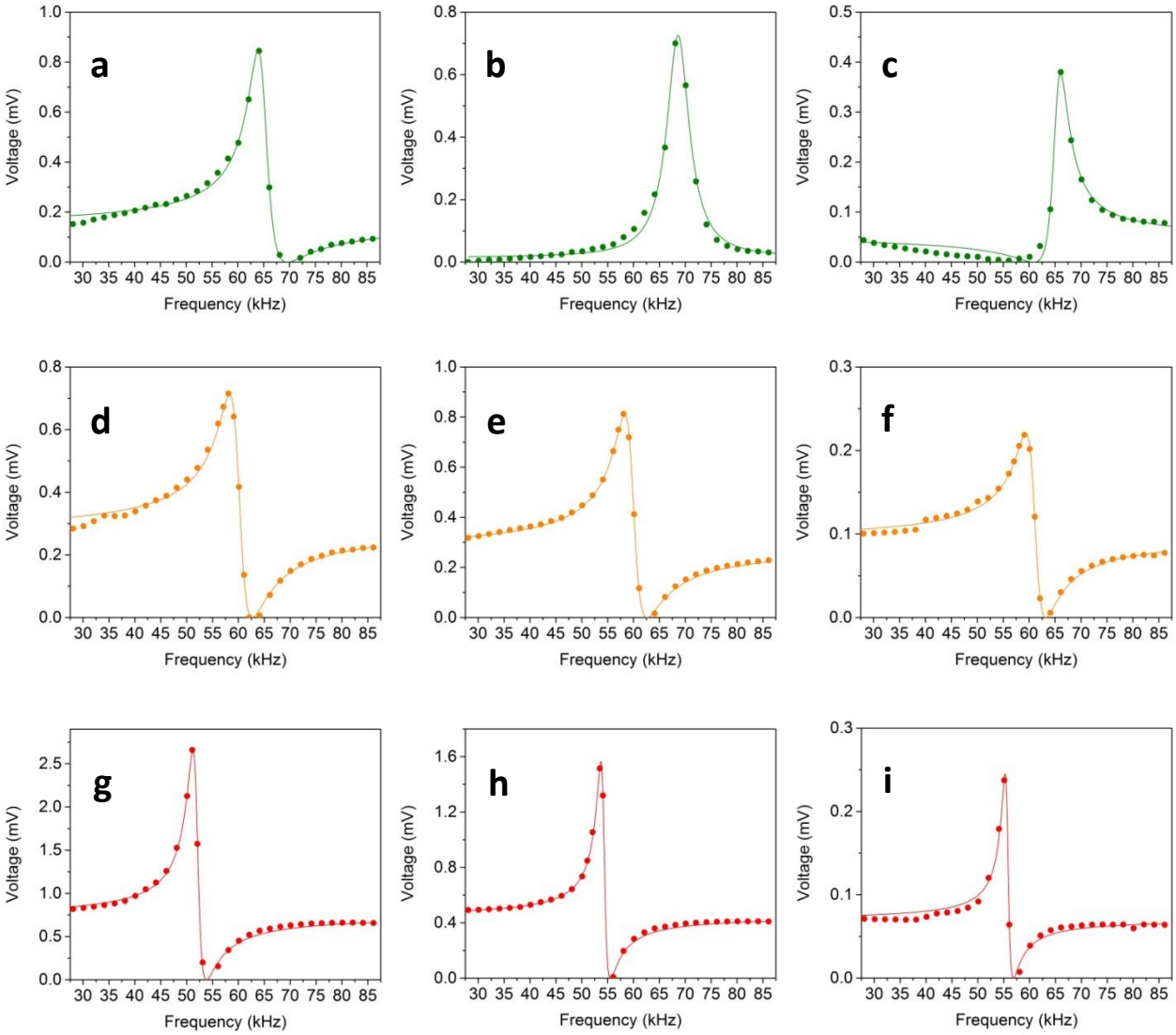

Figure 3.6. (a-c) ME output voltage of aired nanowhiskers samples as a function of H_{ac} frequency under (a) H_{dc}=2.2 Oe, (b) H_{dc}=8.2 Oe and (c) H_{dc}=17.4 Oe. (d-f) ME output voltage of nanowhiskers samples dried at 45 ℃ as a function of H_{ac} frequency under (d) H_{dc}=2.2 Oe, (e) H_{dc}=8.5 Oe and (f) H_{dc}=17.7 Oe. (g-i) ME output voltage of aired nanoshperes samples as a function of H_{ac} frequency under (g) H_{dc}=2.1 Oe, (h) H_{dc}=8.2 Oe and (i) H_{dc}=17.3 Oe. The experimental data (dots) were fitted to a modified Lorentzian equation (3.4) (shown as solid lines).

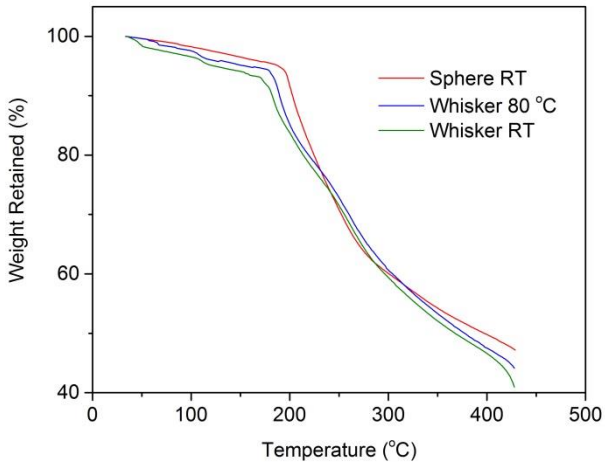

Figure 3.7. TGA curves of CNC films: aired nanospheres (red line) and nanowhiskers (green line) under RT, and vacuum dried nanowhiskers (blue line) under 80 ℃. The reduced weight from 35-100 ℃ was considered as free water evaporation, suggesting nanospheres film has the lowest water content amount. Also the nanospheres shows different decomposition curve compared to nanowhiskers films, indicating the nanospheres and nanowhiskers consist of different crystalline lattices.

To address if the water in CNCs affects their mechanical properties and further influences the ME effect, the Young's modulus of the different CNC films was measured using tensile testing and their ME output voltage shown to be dependent on the Young's modulus. The highest α_{ME} of 2.33 V cm^{-1} Oe^{-1} (**Figure 3.5b**) for the CNC nanospheres correlates to the highest Young's modulus of 2.30 GPa (**Figure 3.8a**). α_{ME} of 1.40 and 0.75 V cm^{-1} Oe^{-1} (**Figure 3.5b**) for CNC nanowhisker vacuum-dried (80 ˚C) and nanowhisker air-dried samples correlate with their respective Young's moduli of 0.96 and 0.08 GPa (**Figure 3.8a**), confirming the greatest output voltages and α_{ME} were achieved from higher modulus CNC films. In addition to mechanical properties, the local piezo-response of the three CNC films

was investigated by switching spectroscopy piezoresponse force microscopy (SS-PFM) (**Figure 3.8b**). During a fully reversible dipolarization of 180˚, the CNC nanospheres air-dried (**Figure 3.8b**, red) and nanowhiskers vacuum-dried samples under 80 ˚C (**Figure 3.8b**, blue) showed a typical butterfly loop in amplitude displacement curves and their respective PE coefficient values estimated to be 9.50 ± 0.3 pm V^{-1} and 10.20 ± 0.6 pm V^{-1}. Considering they have similar PE coefficients despite the CNC nanospheres giving a ≈ 50% increase in ME output voltage, it was reasonable to deduce that their mechanical properties in **Figure 3.5a** play a dominate role in the magnitude of the ME response. Also, these values are ~2 times higher than the PE coefficient calculated in **Chapter 2,** which is due to higher crystallinity in CNC. However, the values are much less than that reported in literature (21 pm V^{-1} see ref. 123 in **Chapter 1**). The difference is attributed to the different forms of CNC films in this work, *e.g.* the films are thicker (~30 μm, Table 3.5) compared to a previous studies on ultra thin CNC layer (less than 100 nm). The thin film is much easier for the bias to penetrate so the value only corresponds to the condition (thickness, water content, crystallinity) of a material. The CNC nanowhisker air-dried samples under room temperature (**Figure 3.8b**, green) show a differently shaped hysteresis loop, particularly a narrower coercive field and 180˚ phase reversal at lower applied voltages. For the same type of ferroelectric material, a thinner film will have lower coercivity.[26] However, the thicknesses of the different CNC films were similar (**Table 3.5**). Thus, the narrower coercive field and non-classical butterfly loop in the CNC nanowhisker air-dried film was attributed to its higher water content, including the movement of free Ca^{2+} (introduced in film casting process) that could influence the electrical dipolarization. Further drying of the CNC nanowhiskers at higher temperatures (45 ˚C) to eliminate residual water content caused the hysteresis loops to

convert to a typical butterfly shape in amplitude displacement curves, with wider coercive field present in the phase loops (**Figure 3.9**). As discussed in **Chapter 2**, the observed Fano resonance was the result of a two-pathway signal interference, namely the ME output voltages induced from vertical and longitudinal directions. Clearly, a higher water content in CNC films had a causative effect on the ME resonance profiles, such as the α_{ME} and damping constants, occurring through changes in the mechanical and PE properties. The removal of free water, or alternatively CNC nanostructures that limited water content, increased the mechanical strength and optimized the PE response to provide an overall higher ME response.

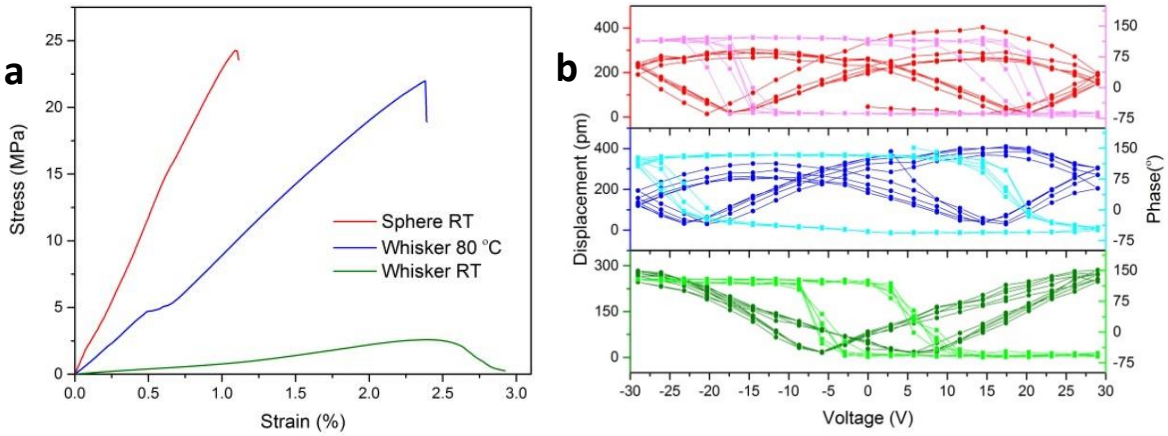

Figure 3.8. (a) Tensile curves of CNC films displayed as stress against strain. (b) The hysteresis loops representing the bias induce amplitude displacement as well as the phase changes corresponding to the hysteresis loops.

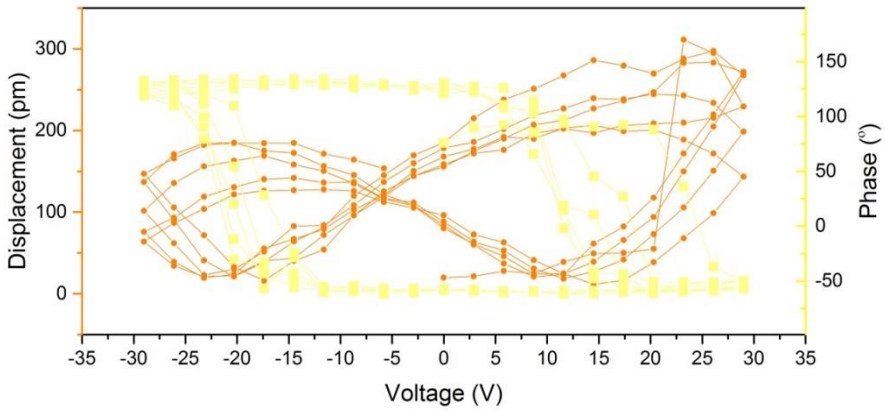

Figure 3.9. Hysteresis loop of randomly arranged nanowhiskers film after dehydration, which was performed by reheating the film under 45 ˚C in a vacuum oven for 6 h.

3.3.3. Anisotropic ME effect of Aligned CNC Whiskers/Metglas Laminate Composites

Having established the CNC-based ME composites, a main objective was to investigate the ability to observe an anisotropic ME effect by introducing PE nanomaterials. To achieve this, a home-built 'spinner' was used to align the CNC nanowhiskers (**Figure 3.10a**) and preferred over other techniques such as doctor blade[27], as the 'spinner' can provide a constant shear that was expected to achieve better alignment. AFM height and phase images confirmed the alignment of the nanowhiskers, with large whiskers arranged perpendicular to the shear orientation and tiny whiskers displaying branch-like structures on the surface (**Figure 3.10b**). In

contrast, a random array of nanowhiskers was observed when no shear was applied for drop casted film (**Figure 3.10c**).

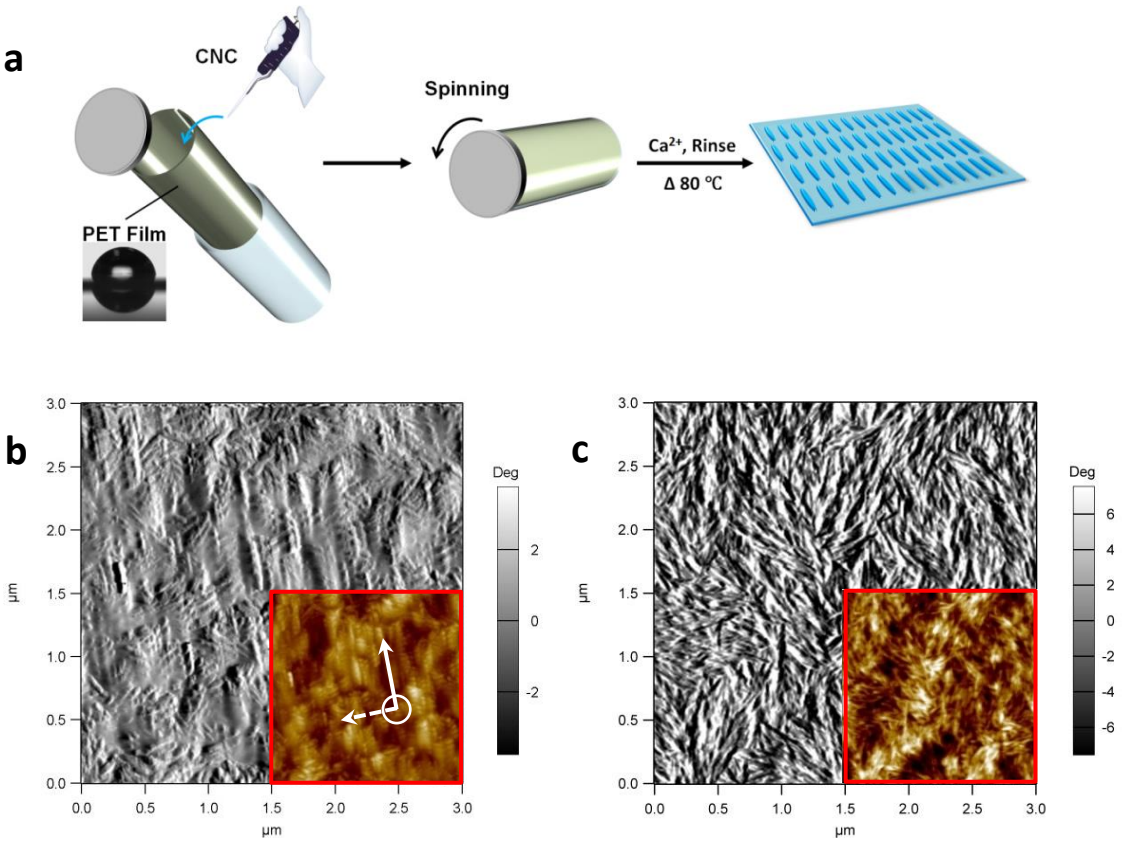

Figure 3.10. (a) Schematic view of CNC whisker alignment. An adhesion removable polyester (PET) film (water contact angle=100.1˚) was used as casting substrate. (b) AFM height (inset section, displayed as in ±25 nm) and phase images of aligned CNC whisker film. The solid and dash arrows indicate the alignment and rolling or shear directions, respectively. (c) AFM height (insect section, displayed as in ±15 nm) and phase images of drop casted non-aligned CNC whisker film. The scanning size of all AFM images was 3×3 μm.

The nanowhisker films were vacuum dried under 80 ˚C using Ca^{2+} as framework stabilizer and combined with MS Metglas *via* epoxy to enable the strain coupling. The Metglas films with the same dimension were attached onto the CNC film at different angles to the aligned orientation of the nanowhiskers. Specifically, the long-edge of the Metglas film was aligned parallel (0˚), perpendicular (90˚) or intermediate at a 45˚ angle to the aligned orientation of the nanowhiskers (**Figure 3.11a**). Using the dynamic testing method as above, stimulating magnetic fields H_{ac} and H_{dc} were applied longitudinally along all the ME laminates. The frequency and H_{dc} dependent curves were shown in **Figure 3.11b, c**, respectively. For all three ME laminates, an ME resonance enhancement with Fano-resonance profile is observed (**Figure 3.11b**) and the α_{ME} increases dramatically from 0-4.0 Oe (**Figure 3.11c**), and then decreases gradually according to the increasing H_{dc}. The good performance under low H_{dc} (up to ~4.0 Oe) was attributed to the high magnetic permeability and low field saturation of the MS Metglas film and all fitting parameters based on equation (3.4) are provided in **Tables 3.6, 3.7 and 3.8**. Significantly, the highest output voltage of 2.23 mV, with calculated α_{ME} of 1.92 V cm^{-1} Oe^{-1} was obtained when the magnetostriction was induced perpendicular (90˚) to the CNC nanowhisker aligned orientation and the lowest was from that applied parallel (0˚) (**Fig. 3.11b,c**), confirming an anisotropic effect in the ME response. Furthermore, intermediate values of α_{ME} were obtained at an applied angle of 45˚. These findings were in agreement with converse PE effects of natural wood sheets that show the greatest mechanical strain when the direction of wood grains were at 90˚ to the applied electrical field[20]. Rotation of the wood grains

to 45˚ gave an intermediate strain, while the lowest strain was observed at an angle of 0˚. Therefore, by successfully reconstructing the orientated cellulose fibril structures found in natural plants *via* the spinning-induced alignment of CNC nanowhiskers, an anisotropic effect originating from the PE phase in ME composites was attained. To confirm whether the mechanical strength of the aligned whisker CNC films also plays a role, tensile tests were conducted by stretching samples at the three different angles from the aligned CNC orientation and show that the Young's modulus is highly dependent on the applied angle of the tensile test (**Figure 3.11d**). However, on this occasion for the aligned CNC, the lowest modulus sample at a tensile testing angle of 90° showed the highest ME output voltage, which was opposite to the non-aligned CNC. Interestingly, a linear dependence was not observed as the highest and intermediate modulus samples, with respective testing angles of 45° and 0°, interchange with respect to the ME output voltage (**cf. Fig. 3.11c and Fig. 3.11d**). Thus, despite the interplay between effects of PE anisotropy and mechanical properties, the results suggested that the strain coupling direction, *i.e.* magnetostriction relative to the PE orientation, was important for producing the highest ME output voltage in aligned CNC. To confirm the above anisotropic effect, control samples were also fabricated by attaching Metglas films at angle intervals of 0˚, 45˚ and 90˚ onto drop casted CNC films with randomly aligned nanowhiskers, as seen in **Figure 3.12a**. At all angles, the peak voltage (V_{peak}) outputs were very similar with a value of ~1.75 mV under H_{dc}=4.0 Oe (**Figure 3.12b**), confirming a non-anisotropic effect for these randomly-aligned samples.

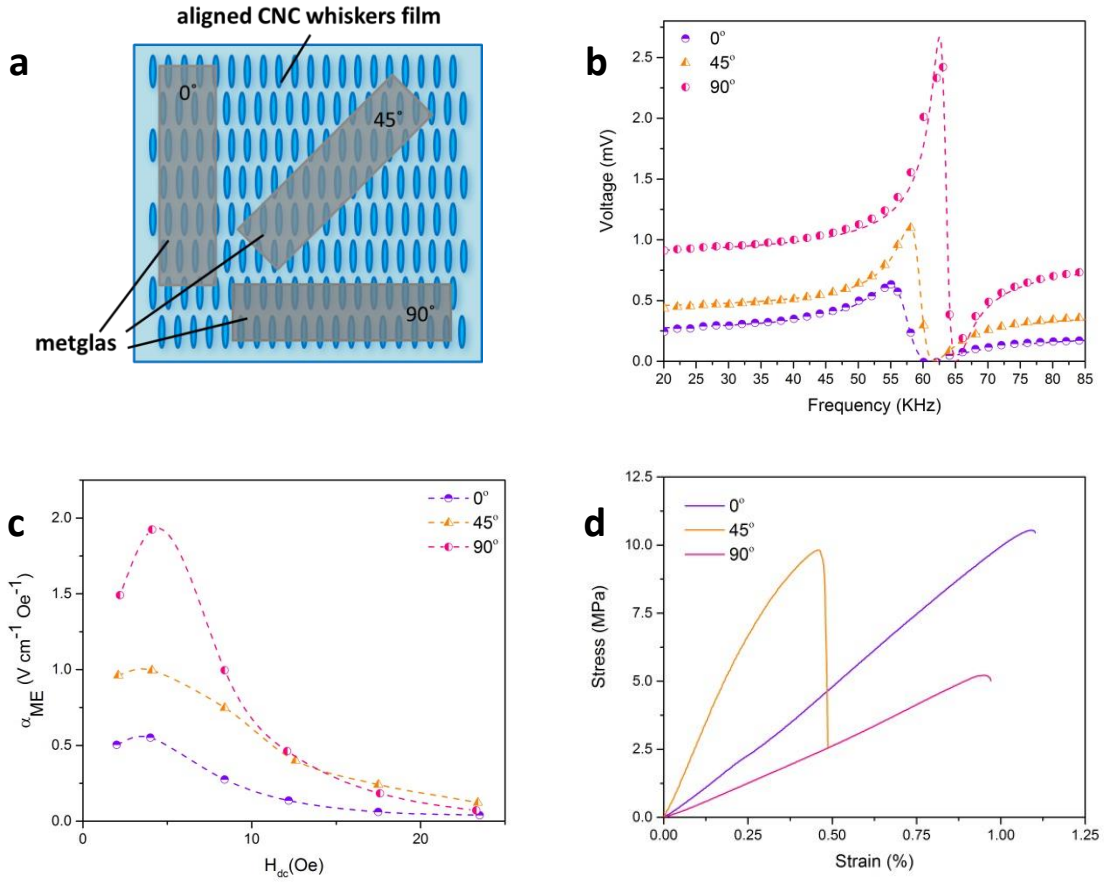

Figure 3.11. (a) The schematic illustration of MS and PE combination. The actual laminate was fabricated by tailoring the aligned whisker CNC film into desired size through different directions, sputter coating surface electrodes, and then glued with Metglas. (b) ME output voltage as a function of H_{ac} frequency under H_{dc}=4.0 Oe and H_{ac}=0.4 Oe. The experimental data (dots) were fitted to equation (3.4). (c) Resonance enhanced *ME* output voltage as a function of H_{dc}, and the H_{ac} strength was fixed as 0.4 Oe. (d) tensile curves obtained from aligned whisker CNC film at testing angles of 0˚, 45˚ and 90˚. The results were displayed as stress against strain.

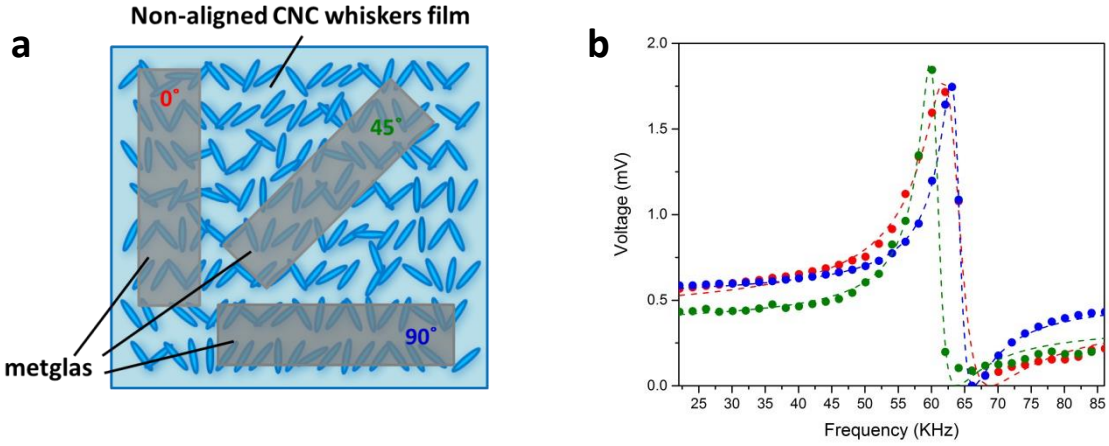

Figure 3.12. (a) The schematic illustration of ME response induced from non-aligned CNC whiskers based ME laminates with 3 different testing angles. The actual laminate was fabricated by tailoring the aligned whisker CNC film into desired size through different directions, sputter coating surface electrodes, and then glued with Metglas. (b) ME output voltage induced from 3 testing angles as a function of H_{ac} frequency under H_{dc}=4.0 Oe and H_{ac}=0.4 Oe. The experimental data (dots) were fitted to equation 3 (shown as dashed lines).

Table 3.6. Fitting parameters (imaginary section) of equation (3.4) for anti-resonance frequency effect of aligned nanowhiskers ME laminate at 0˚ testing angle under different H_{dc} strength.

H_{dc} (Oe)	A (mV)	f_r (kHz)	f_a (kHz)	δ_r	δ_a
2.0	0.2535	57.7560	59.2023	-0.0422	0.0493
4.0	0.2956	57.3004	58.6598	-0.0533	0.0555
8.4	0.1441	57.8364	59.6155	-0.0532	0.0544
12.2	0.1088	58.0102	59.3114	-0.0469	0.0141
17.5	0.0528	58.6455	59.6057	-0.0442	0.0112
23.6	0.0476	59.6851	60.1364	-0.0381	0.0124

Table 3.7. Fitting parameters (imaginary section) of equation (3.4) for anti-resonance frequency effect of aligned nanowhiskers ME laminate at 45˚ testing angle under different H_{dc} strength.

H_{dc} (Oe)	A (mV)	f_r (kHz)	f_a (kHz)	δ_r	δ_a
2.2	0.4292	63.3463	65.2271	-0.0265	0.0725
4.0	0.6675	63.4143	65.0039	-0.0193	0.0520
8.4	0.3338	63.7681	65.8497	-0.0226	0.0529
12.6	0.2543	64.6473	65.9233	-0.0237	0.0229
17.6	0.1527	65.5765	66.3572	-0.0209	0.0071
23.3	0.1193	66.1313	66.4977	-0.0208	-0.0075

Table 3.8. Fitting parameters (imaginary section) of equation (3.4) for anti-resonance frequency effect of aligned nanowhiskers ME laminate at 90˚ testing angle under different H_{dc} strength.

H_{dc} (Oe)	A (mV)	f_r (kHz)	f_a (kHz)	δ_r	δ_a
2.1	0.3437	59.0790	60.1090	-0.0322	0.0637
4.0	0.4147	59.4076	60.4718	-0.0308	0.0483
8.4	0.2917	59.9820	60.7676	-0.0279	0.0525
12.6	0.1933	60.5137	61.0982	-0.0276	0.0396
17.2	0.1572	60.9415	61.3103	-0.0280	0.0211
23.4	0.0992	61.4236	61.5523	-0.0259	0.0114

3.4. Conclusion

In conclusion, an anisotropic ME effect provides new opportunities for the development of polymer-based ME composite with vector sensing ability, which as yet cannot be achieved using bulk, homogeneous, PE polymer films. Although the incorporation of nanomaterials into polymer-based ME composites has enabled the

demonstration of anisotropic ME sensors[28], the use of nanomaterials was restricted to inorganic MS components, such as magnetic nanowires (iron, nickel and Galfenol) [29] or nanosheets, such as δ-FeO(OH) or CoFeOOH,[28,30] within 0-3 particulate composites that inevitably show very small output voltages at the micro-volt level. A significant advance in this work was that the introduction of a PE nanomaterial into polymer-based ME composites that enabled an anisotropic ME effect that produces an output voltage that was an order of magnitude higher than those from previous anisotropic ME devices. The ME composites also took advantage of cellulose as a renewable and cheap material, as well as biocompatible and biodegradable properties, and demonstrated the general concept of using PE biomaterials in ME composites. In using cellulose, it is therefore possible to have facile synthesis of a diverse array of CNC that by virtue of their nanoscale dimensions bring new function and capabilities to ME biopolymer-based ME composites.

Note

The manuscript based on **Chapter 3.** is published as a journal article with citation as below:

Zong, Y.; Yue, Z.; Higgins, M. J. *Nanocrystalline cellulose for anisotropic magnetoelectric composites*. Macromolecular Materials and Engineering **2018** *303*, 201800099.

3.5. References

1 Ryu, J. *et al.* Ubiquitous magneto-mechano-electric generator. *Energy Environ. Sci.* **8**, 2402-2408, (2015).

2 Israel, C., Mathur, N. D. & Scott, J. F. A one-cent room-temperature magnetoelectric sensor. *Nat Mater* **7**, 93-94, (2008).

3 Heron, J. T. *et al.* Deterministic switching of ferromagnetism at room temperature using an electric field. *Nature* **516**, 370-373, (2014).

4 Wang, Y., Hu, J., Lin, Y. & Nan, C.-W. Multiferroic magnetoelectric composite nanostructures. *NPG Asia Mater* **2**, 61-68, (2010).

5 Martins, P. & Lanceros-Méndez, S. Polymer-Based Magnetoelectric Materials. *Adv. Funct. Mater.* **23**, 3371-3385, (2013).

6 Jin, J. *et al.* Multiferroic Polymer Composites with Greatly Enhanced Magnetoelectric Effect under a Low Magnetic Bias. *Adv. Mater.* **23**, 3853-3858, (2011).

7 Lee, B. Y. *et al.* Virus-based piezoelectric energy generation. *Nat Nano* **7**, 351-356, (2012).

8 Fukada, E. Piezoelectric properties of biological polymers. *Quarterly Reviews of Biophysics* **16**, 59-87, (1983).

9 Zong, Y. *et al.* Cellulose-based magnetoelectric composites. *Nature Communications* **8**, 38, (2017).

10 Habibi, Y., Lucia, L. A. & Rojas, O. J. Cellulose Nanocrystals: Chemistry, Self-Assembly, and Applications. *Chemical Reviews* **110**, 3479-3500, (2010).

11 Klemm, D. *et al.* Nanocelluloses: A New Family of Nature-Based Materials. *Angew. Chem. Int. Ed.* **50**, 5438-5466, (2011).

12 Lagerwall, J. P. F. *et al.* Cellulose nanocrystal-based materials: from liquid crystal self-assembly and glass formation to multifunctional thin films. *NPG Asia Mater* **6**, e80, (2014).

13 Wang, N., Ding, E. & Cheng, R. Preparation and Liquid Crystalline Properties of Spherical Cellulose Nanocrystals. *Langmuir* **24**, 5-8, (2008).

14 Wang, N., Ding, E. & Cheng, R. Thermal degradation behaviors of spherical cellulose nanocrystals with sulfate groups. *Polymer* **48**, 3486-3493, (2007).

15 Moon, R. J., Martini, A., Nairn, J., Simonsen, J. & Youngblood, J. Cellulose nanomaterials review: structure, properties and nanocomposites. *Chemical Society Reviews* **40**, 3941-3994, (2011).

16 Pei, A., Malho, J.-M., Ruokolainen, J., Zhou, Q. & Berglund, L. A. Strong Nanocomposite Reinforcement Effects in Polyurethane Elastomer with Low Volume Fraction of Cellulose Nanocrystals. *Macromolecules* **44**, 4422-4427, (2011).

17 Majoinen, J. *et al.* Chiral Plasmonics Using Twisting along Cellulose Nanocrystals as a Template for Gold Nanoparticles. *Adv. Mater.* **28**, 5262-5267, (2016).
18 Xiong, R. *et al.* Ultrarobust Transparent Cellulose Nanocrystal-Graphene Membranes with High Electrical Conductivity. *Adv. Mater.* **28**, 1501-1509, (2016).
19 Wang, B. & Walther, A. Self-Assembled, Iridescent, Crustacean-Mimetic Nanocomposites with Tailored Periodicity and Layered Cuticular Structure. *ACS Nano* **9**, 10637-10646, (2015).
20 Gindl, W., Emsenhuber, G., Plackner, J., Konnerth, J. & Keckes, J. Converse Piezoelectric Effect in Cellulose I Revealed by Wide-Angle X-ray Diffraction. *Biomacromolecules* **11**, 1281-1285, (2010).
21 Brian, J. R., Clint, C., Sergei, V. K. & Roger, P. Dual-frequency resonance-tracking atomic force microscopy. *Nanotechnology* **18**, 475504, (2007).
22 Oh, S. Y. *et al.* Crystalline structure analysis of cellulose treated with sodium hydroxide and carbon dioxide by means of X-ray diffraction and FTIR spectroscopy. *Carbohydr. Res.* **340**, 2376-2391, (2005).
23 Nelson, M. L. & O'Connor, R. T. Relation of certain infrared bands to cellulose crystallinity and crystal lattice type. Part II. A new infrared ratio for estimation of crystallinity in celluloses I and II. *J. Appl. Polym. Sci.* **8**, 1325-1341, (1964).
24 Reis, S. *et al.* Electronic optimization for an energy harvesting system based on magnetoelectric Metglas/poly(vinylidene fluoride)/Metglas composites. *Smart Mater. Struct.* **25**, 085028, (2016).
25 Srinivasan, G. Magnetoelectric Composites. *Annu. Rev. Mater. Res.* **40**, 153-178, (2010).
26 Liu, F. *et al.* Room-temperature ferroelectricity in CuInP2S6 ultrathin flakes. *Nature Communications* **7**, 12357, (2016).
27 Diaz, J. A., Wu, X., Martini, A., Youngblood, J. P. & Moon, R. J. Thermal Expansion of Self-Organized and Shear-Oriented Cellulose Nanocrystal Films. *Biomacromolecules* **14**, 2900-2908, (2013).
28 Gonçalves, R. *et al.* Synthesis of highly magnetostrictive nanostructures and their application in a polymer-based magnetoelectric sensing device. *Eur. Polym. J.* **84**, 685-692, (2016).
29 Alnassar, M. Y., Ivanov, Y. P. & Kosel, J. Flexible Magnetoelectric Nanocomposites with Tunable Properties. *Advanced Electronic Materials* **2**, 1600081-n/a, (2016).
30 Martins, P. *et al.* Novel Anisotropic Magnetoelectric Effect on δ-FeO(OH)/P(VDF-TrFE) Multiferroic Composites. *ACS Appl. Mater. Interfaces.* **7**, 11224-11229, (2015).

Chapter 4. Magnetoelectric Coupling in Nanoscale 0-1 Connectivity

4.1. Introduction

The ME effect is the interaction between electrical polarization and magnetization components that enables magnetic-to-electrical signal conversion. Early studies on Cr_2O_3 reported a ME voltage coefficient ~0.01 V Oe^{-1} cm^{-1}, which is the highest value for ME single phase crystal to date.[1] Due to the good room temperature ME performance,[2,3] ME composites are promising for a wide range of applications from electronic to magnetic devices.[4,5] Their separated PE and MS components that coexist in ME composites gives rise to strain-mediated giant ME responses (>1 V Oe^{-1} cm^{-1}) orders of magnitude higher compared to single phase ME crystals (*e.g.* Cr_2O_3).[6] The elastic connection between the two phases is essentially the tensor property and regarded as the configuration of merit required to produce the enhanced ME coupling[7] and associated output voltage.[3] Thus, studies on various configurations and 'connectivities' between the two phases have attracted extensive research interest[8].

Generally, the connectivity of ME coupling is determined according to the dimension of the MS and PE phases. In particular, particulate composites consisting of MS particles within a bulk PE material is known as 0-3 connectivity,[9-11] laminate composites made of MS and PE layers are in a 2-2 connectivity,[12-14] and

heterostructural composites with magnetostrictive rods embedded in a piezoelectric bulk are defined as 1-3 connectivity (**as shown in Chapter 1, Figure 1.13**).[15-17] These aforementioned connectivities are well-studied however novel connectivities are emerging and being explored for their ME properties. For example, a significant increase the non-resonant ME effect with α_{ME} of 22 V Oe^{-1} cm^{-1} was achieved using a composite in a 2-1 connectivity: this consists of a layer of aligned PE fibers (1-D) laminated with a Metglas layer (2-D).[1] A novel 1-1 connectivity ME composite consisting of a $Pb(Mg,Nb)O_3$-$PbTiO_3$ (PMN-PT) single-crystal fiber (1-D) combined with a Metglas fiber (1-D) showed a dramatic enhancement of the α_{ME} with a value of ~7,000 V Oe^{-1} cm^{-1} at resonance, which is approximately 7 times higher than previously studied 2-1 connectivity PMN-PT piezofiber layer/Metglas composite.[18] Ceramic nanoparticles/wires were typically used to produce particulate composites to achieve connectivities of 0-0 or 0-1 however due to the poor adhesive property of ceramic nanoparticles/nanowires an additional component to build up ME coupling. Earlier studies have introduced polymer as a binder (3-D bulk) to provide strain coupling between MS (0-D) and PE (0-D) nanoparticles.[19,20] These ME composite consisting of three phases are not considered to be 0-0 type but effectively 0-0-3 in connectivity. Therefore, in order to achieve a purely two phase ME composite in 0-0 or 0-1 connectivities at least one of the two phases should be a self-assembling material to form stable composites, *e.g.* consisting of 2 different MS and PE nanomaterials without a binder.

CNC nanowhiskers as a 1-dimentional (1D) with high aspect ratio[21] is a very suitable material to fabricate novel connectivity ME composites. They have self-assembly properties,[22] thus providing the possibility of developing a two-phase composite embedded with magnetic nanoparticles,[23,24] and therefore give rise to potential ME coupling in low-dimension 0-1 connectivity (**Figure 4.1a**).

The primary aim of this chapter is to develop and investigate a novel 0-1 connectivity ME composites based on CNC. To achieve this, MS nanoparticles were embedded in a cellulose nanowhisker network whereby the nanoparticle diameter and CNC nanowhiskers width were both on the scale of tens of nanometers and therefore the ME coupling between the two components were considered to be a nanoscopic 0-1 connectivity (**Figure 4.1a**), which has not previously been reported. In order to study the effect of interaction between the PE and MS nanomaterials (the coupling essentially giving rise to ME effect) two types of MS nanoparticles, namely cobalt ferrite (CFO) and surfactant modified CFO with cetyltrimethylammonium bromide (CTAB-CFO) were employed. CNC produced from sulfuric acid hydrolysis presents surface sulfonic groups, and both CNC and CFO possess hydroxyl groups. Consequently, their hydrophilic surfaces were conducive to the formation of hydrogen bonding, thus enabling a relatively stable interaction between the CNC and CFO. In contrast, CTAB-CFO nanoparticles were more hydrophobic and expected to form a weaker interaction with the CNC due to the reduced hydrogen bonding.

4.2. Experimental Methods

CNC Preparation: CNC was produced from filter paper *via* acid hydrolysis using 65 wt% H_2SO_4. To prepare cellulose nanowhiskers, 4g filter paper (Advantec, Lot No. 90909520) was cut into strips 0.5 cm in width and blended with 30 mL H_2SO_4. The hydrolysis reaction took place under 70 ˚C with constant stirring over 1,000 rpm for 20 min. To cease the reaction, 250 mL iced DI water was added and the resultant suspension was washed by centrifugation at ~10,000 rpm for several rounds until the upper layer became turbid. The pH value under this condition is ~ 2. The obtained CNC formed a gel-like aqueous dispersion with concentration of approximately 7 wt%. After calculating the precise concentration of each batch by solvent evaporation method, the CNC samples were stored under 4 ˚C without further treatment until use.

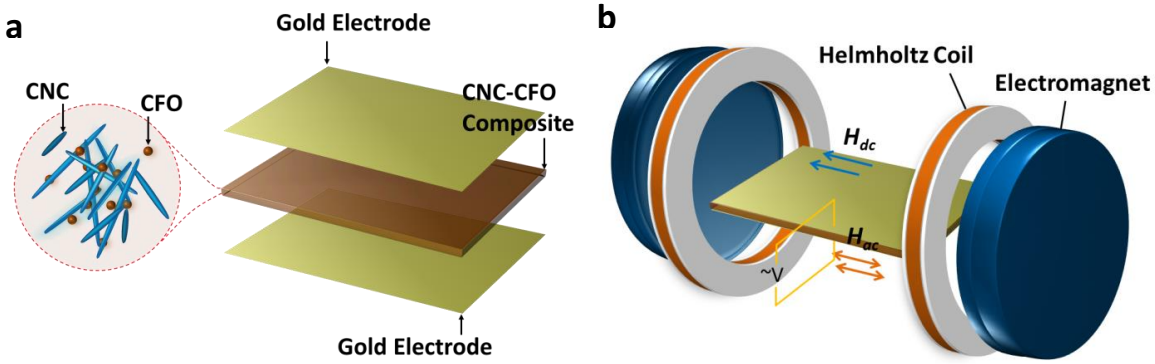

Figure 4.1. (a) Schematic view of CNC embedded magnetostrictive nanoparticles composite and the ME coupling in nanoscopic 0-1 connectivity. (b) Schematic view of the bulk system for ME voltage measurement. The output voltage was collected from the interface gold electrodes and monitored as root mean square (RMS) values using a lock-in amplifier.

Fabrication of ME Composites: Two types of MS nanoparticles were used to fabricate ME composites. The commercially available CFO nanoparticles (Sigma-Aldrich, Cat. No. 773352) were used as received; the surfactant modified CTAB-CFO nanoparticles were prepared by the lab at University of Minho, Portugal and the details can be found in an earlier study.[25] Firstly, 0.05 g CFO or CTAB-CFO nanoparticles were dispersed in 1.5 mL DI water and sonicated for 0.5 h. The desired amount of CNC suspension was then added to make aqueous dispersions with CNC:CFO (or CNC:CTAB-CFO) in 1:19, 1:9 and 1:4 in weight, and the corresponding MS concentrations in composites were calculated as 5 wt%, 10 wt% and 20 wt%, respectively. To avoid CNC degradation, the dispersions were sonicated for 15 min in an ice bath and poured into Teflon evaporation wells with 0.8 mm in thickness. After evaporation for 2 h, the evaporation wells were immersed in 0.5 M $AlCl_3$ solution for 5 min, followed by DI water washing and dried as films under room temperature (20 ˚C). The ME composite films were further vacuum dried under 50 ˚C to eliminate residual water and sputter coating used to deposit 30 nm gold layers as surface electrodes for the ME measurements (**Figure 4.1a**).

Bulk ME Effect Measurement: An alternating Helmholtz coil was used to apply a magnetic ac field at 0.6 Oe at a fixed frequency of 5 kHz following the method in previous report.[26] A separate electromagnet was use to apply magnetic dc fields with strengths in the range of 0-3000 Oe and both the ac and dc magnetic fields were

applied simultaneously along the length direction of the ME laminate composites. The induced ME output voltage was recorded using a model SR8 10 DSP lock-in amplifier (**Figure 4.1b**).

Magnetic Measurement: Magnetic properties of CFO and CTAB-CFO nanoparticles were characterized using a 14T PPMS system with vibrating sample magnetometer (VSM) function. All measurements were taken under room temperature (300K) with applied magnetic fields ranging from -10,000 to 10,000 Oe.

X-Ray diffraction (XRD): XRD measurements were performed on CNC using a GBC MMA XRD (λ = 1.54Å) in the range of 10-80 ˚ on the 0-1 connectivity ME composite films and CFO/CTAB-CFO nanoparticles. The voltage, current and scanning speed were set to −40 kV, 25mA and 2˚ min^{-1}, respectively.

Fourier Transform Infrared Spectroscopy (FT-IR): FT-IR spectrum was recorded on a Shimadzu AIM8000 FT-IR spectrometer. The pure CNC film and the 0-1 connectivity ME composite films were measured using an FT-IR ATR method in the range of 900-1450 cm^{-1}.

Atomic Force Microscope (AFM): An MFP-3D Atomic Force Microscope (Asylum Research, Santa Barbara, US) was used for imaging the CNC, magnetic nanoparticles and 0-1 ME composite films. AFM imaging was performed using a Tap300-G tip (Budget Sensors, Bulgaria) with resonant frequency of 300 kHz and spring constant

of 40 N m^{-1}. The height and phase images were obtained in air using tapping mode with scan rate of 1.0 Hz.

Piezoresponse Force Microscopy (PFM): The local piezoelectric response of CNC was measured with an MFP-3D Atomic Force Microscope (Asylum Research, Santa Barbara, US) using PFM. A conductive tip (Olympus OMCL-AC240TM) with Pt/Ti coating, resonant frequency of 70 kHz and spring constant of ~2.0 N m^{-1} were used. The PFM height, amplitude and phase images were obtained in Dual AC Response Tracking (DART) mode[27] with contact resonant frequency of ~ 260 kHz. The piezoelectric response was measured as the first-harmonic of a bias-induced tip deflection: $d = d_0 + A\cos(\omega t + \varphi)$, where d_0 is the equilibrium position of the tip; A is the amplitude and ω is the frequency of applied bias; φ is the phase yielded information on the polarization direction below the tip. To study the polarization switching dynamics, switching spectroscopy-PFM (SS-PFM) was used to obtain the local piezoelectric hysteresis loop. For each laminate sample, SS-PFM measurements were acquired across a 3×3 μm^2 area by applying a bias at least 5 positions on the sample. The voltage during the SS-PFM measurements was applied in the range of ± 29 V with a frequency of 0.5 Hz, which was sufficient to reversibly switch the polarization component. To enable this, the PFM instrumentation was modified by connecting an external amplifier to increase the upper limit of output signal to ± 30V. The driving amplitude was set to 200 mV for all PFM measurements. To perform the SS-PFM measurements, the cellulose nanowhiskers were drop cast onto a gold mylar

substrate, and then a sequence of inducing bias is applied through a conductive tip (see **Chapter 1, Figure 1.34**). To estimate the piezoelectric coefficient, the peak value of displacement was divided by the corresponding inducing bias based on three testing points.

4.3. Results and Discussion

4.3.1. Morphology and Crystallinity of CNC

CNC can be produced from different resources and among them CNC synthesized from cotton were high crystalline products with crystallinity >85 %.[22,28] The CNC nanowhiskers used for this work were synthesized from filter paper, which contained 100% cotton α-cellulose. The obtained CNC nanowhiskers have high aspect ratio, with ~300 nm in length and 40-60 nm in width (**Figure 4.2 a,b**). X-ray diffraction (XRD, **Figure 4.2c**) spectrum reveals the nanowhiskers retain the cellulose I crystalline lattice of the cotton α-cellulose before acid hydrolysis,[29] indicating the synthesis process does not affect the crystalline configuration. Previously in **Chapter 2, Figure 2.9** it was shown that the cellulose crystallinity plays a direct role in the piezoelectric properties and further influences the ME effect.[30] As such, synthesizing and/or treating cellulose to induce a higher degree of crystallinity is expected to increase performance of ME composite output voltages. Different methods were reported to study the crystallinity of cellulose[29,31] and the crystallinity index (DI)

calculated from XRD intensity is one of the most reliable methods, which is expressed by the following equation:[29]

$$CI = \frac{(I_{002} - I_{am})}{I_{002}} \quad (4.1)$$

where I_{002} is the intensity of (002) peak at 22.82˚ and I_{am} is the intensity of the amorphous component at 2θ of 18˚ for cellulose crystalline I (**Figure 4.2c**).[29] Based on equation 4.1 the CI of CNC in this study is calculated as 91.72%, which is slightly higher than previously reported CNC nanowhiskers synthesized from cotton.[28]

4.3.2. PE Properties of CNC

Since the piezoelectricity of cellulose is essentially governed by its crystallinity, a high crystallinity is expected to increase the piezoelectricity. As the only suitable technique that allows piezoelectric measurement on nanomaterials, Switching Spectroscopy-Piezoresponse Force Microscopy (SS-PFM) was used to measure the local PE properties.

The dynamic of the CNC nanowhisker piezoresponse was shown as hysteresis loops of both displacement (change in amplitude) and phase change as a function of the applied tip voltage (**Figure 4.2d**). A classical butterfly shape of the displacement and 180˚ change in the phase confirms a fully reversible piezoelectric dynamic, which was essentially the bias induced di-polarization process of piezoelectric material.[32,33] Based on a tip bias induced displacement and a coercive field of approximately 40 V (from -18 to over 20 V), the PE coefficient is estimated to be 11.67±0.94 pm V^{-1}

based on three hysteresis loops. This value is similar to cellulose whiskers produced from α-cellulose powder in previous **Chapter 3**.

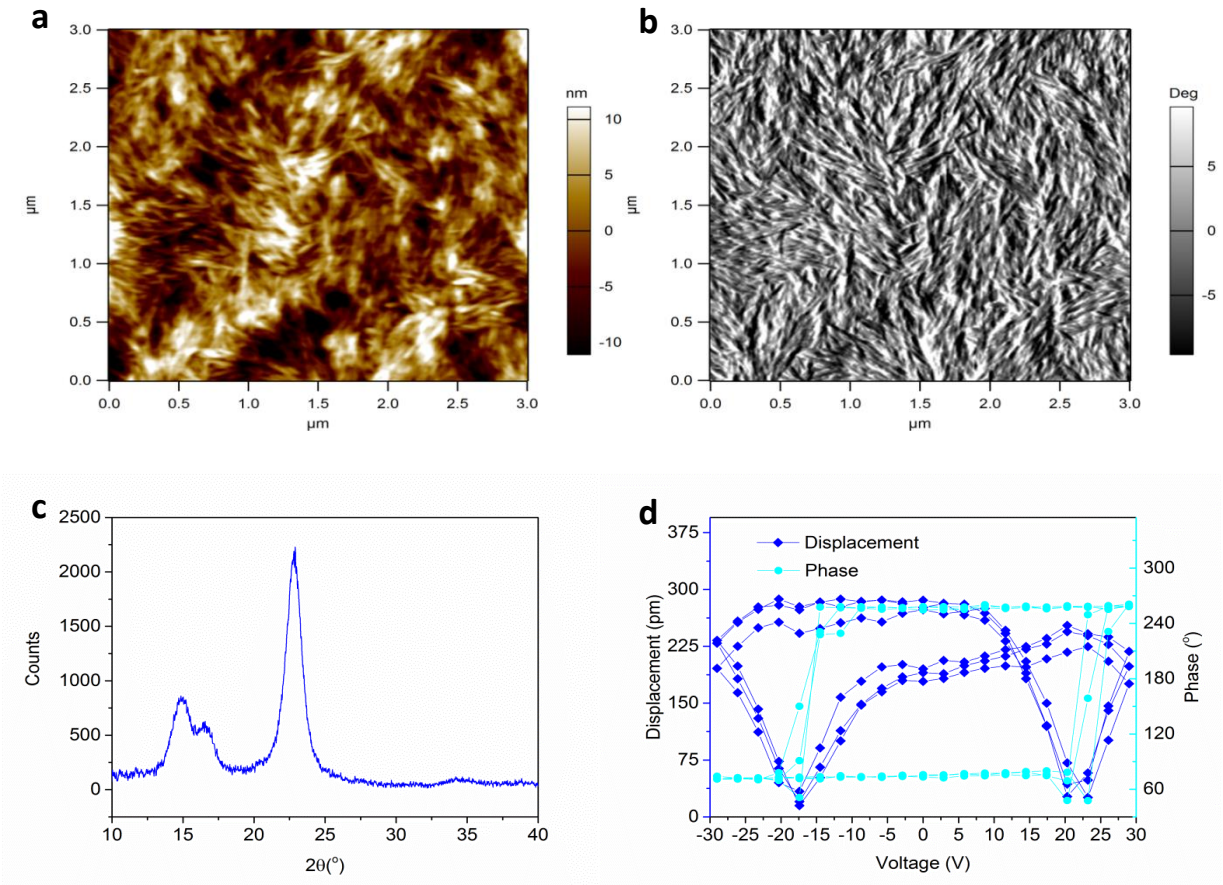

Figure 4.2. (a,b) AFM (a) height and (b) phase images of cellulose nanowhiskers, the scanning size is 3 μm × 3 μm. (c) XRD spectrum of the resulted CNC. The cellulose nanowhiskers have interference rising at diffraction angles 2θ=14.9˚, 17.4˚, 20.7˚, 22.8˚ and 34.6˚ corresponding to lattice (101), (10$\tilde{1}$), (021), (002) and (004), which is the typical XRD spectrum for cellulose crystalline I. (d) The hysteresis loops (3 cycles) representing the bias induce amplitude displacement as well as the phase changes corresponding to the displacement hysteresis loops.

4.3.3. Magnetic Properties of CFO and CTAB-CFO Nanoparticles

Figures 4.3a, b show the magnetic hysteresis loops of CFO and CTAB-CFO nanoparticles, respectively. The particle size of the commercial CFO was ~30 nm as indicated by the supplier and the CTAB-CFO was ~50 nm as shown in earlier report.[25] The saturation magnetization values under room temperature were 54.79 emu g^{-1} for CFO and 59.72 emu g^{-1} for CTAB-CFO nanoparticles, both of which were slighter lower than values obtained previously for 24 nm size CFO sample.[34] However, an obvious difference is found in their coercivity values, which were 3200 Oe and 3870 Oe for CFO and CTAB-CFO nanoparticles, respectively, and in contrast to 1205 Oe for the 24 nm size CFO sample.[34] The wider coercive fields of CFO and CTAB-CFO nanoparticles in this work were presumably caused by their increased volume. The effect of increased volume on coercive field is also observed in spherical and cubic CFO nanocrystals at extremely low temperature of 5K.[35]

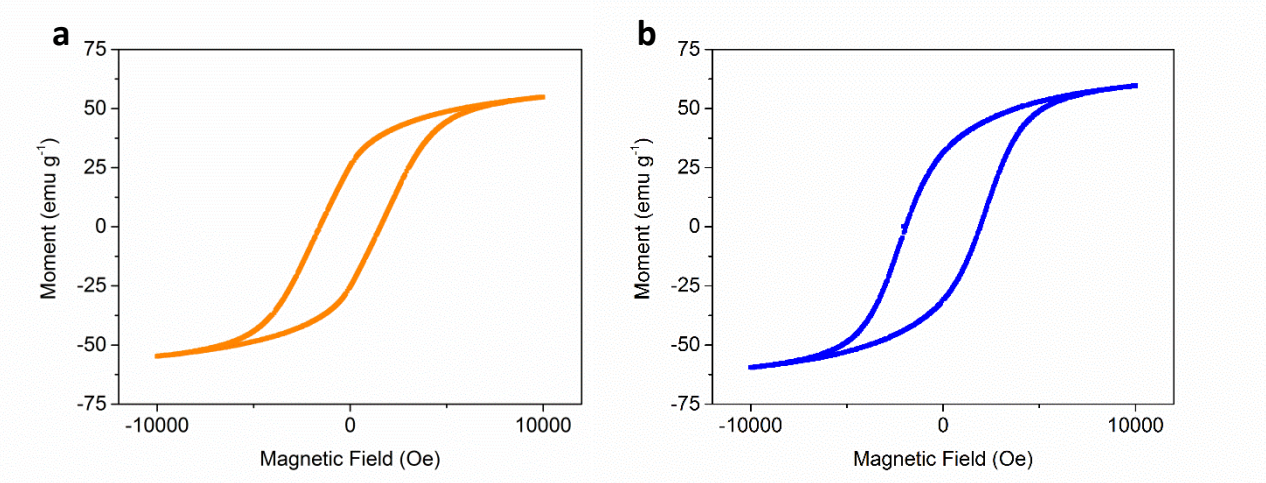

Figure 4.3. (a,b) Magnetic hysteresis loops of (c) CFO and (d) CTAB-CFO nanoparticles measured at room temperature (300K).

4.3.4. Dispersion Properties of CFO and CTAB-CFO Nanoparticles

Different from particulate ME composites in which nanoparticles were embedded in a soft 3-D polymer bulk,[36,37] the MS nanoparticles in this research were distributed in a matrix consisting of 1-D CNC nanowhiskers. In order to understand the effect of the surface chemistry of MS nanoparticles, such as hydrophilic and hydrophobic groups, on their physical interactions with CNC nanowhiskers and subsequently on the ME composite properties, two different types of MS nanoparticles, hydrophilic CFO nanoparticles and surfactant modified CTAB-CFO nanoparticles, were investigated. The effect of surface groups on nanoparticle dispersions in aqueous condition is shown in **Figures 4.4a, b**. CFO or CTAB-CFO nanoparticles were well-dispersed in DI water after sonication (**Figure 4.4a**). After standing for 10 min, the CFO nanoparticles maintain their suspension due to their hydrophilicity, however, most of

the hydrophobic CTAB-CFO nanoparticles were precipitated and form an aggregation in the upper layer (**Figure 4.4b**). To further understand the interaction between the MS nanoparticles and CNC nanowhiskers, a CNC suspension (CNC mass is equivalent to MS nanoparticles) is added to the nanoparticle dispersions, followed by sonication (**Figure 4.4c**). CNC is a hydrophilic nanomaterial due to the presence of surface hydroxyl groups, in addition to sulfonic groups from the acid hydrolysis process that enable the formation of stable aqueous dispersions. Consequently, the hydrophilic CFO nanoparticles with CNC nanowhiskers maintain good dispersions after 12 h whereas in contrast the hydrophobic CTAB-CFO nanoparticles do not maintain dispersions after 12 h (**Figure 4.4d**). Interestingly, the CFO nanoparticles with CNC nanowhiskers were precipitated after 1 week (**Figure 4.4e**). This is due to magnetic attraction of CFO nanoparticles that reduced the dispersion ability of cellulose nanowhiskers, suggesting the CFO nanoparticles were attached to the CNC.

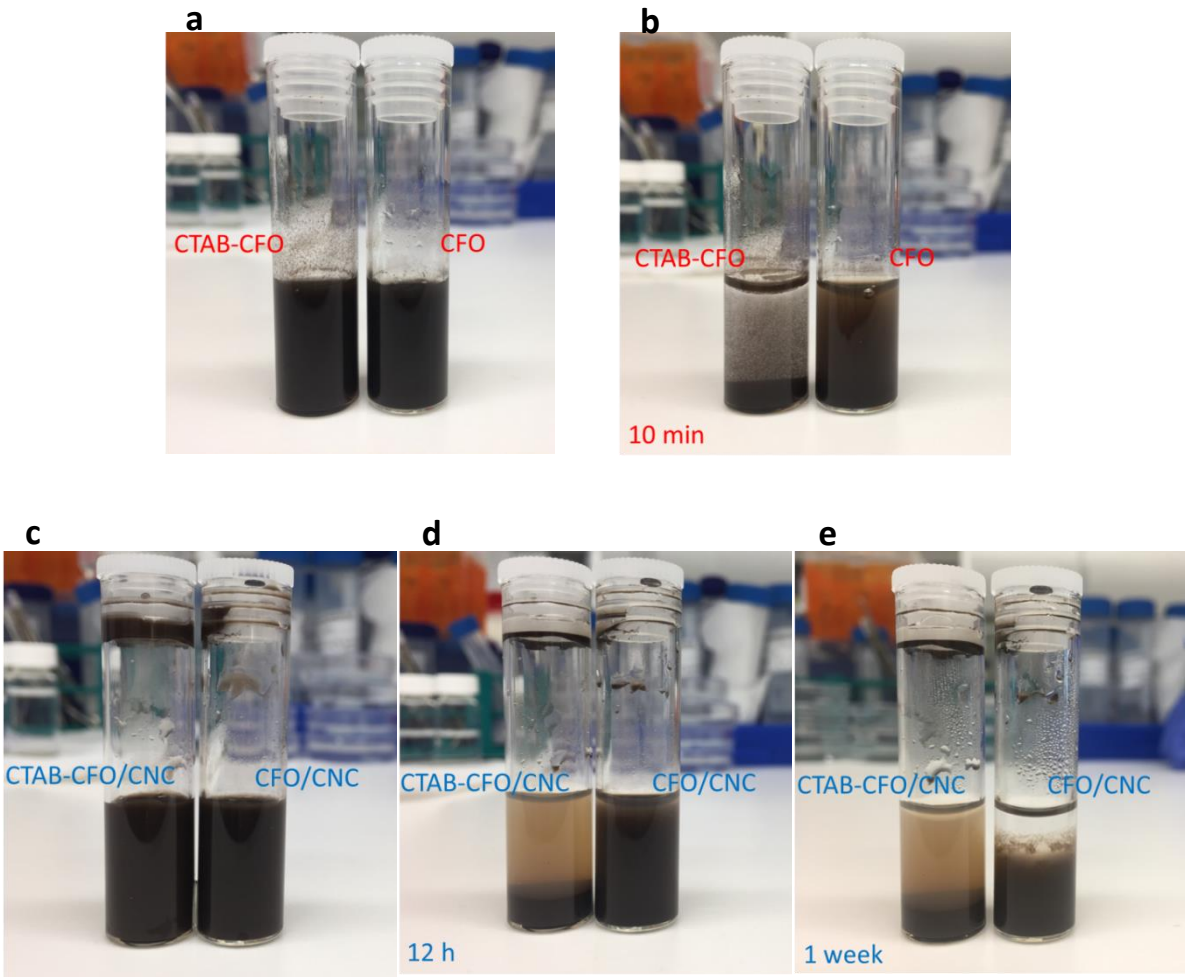

Figure 4.4. (a,b) Dispersion of CTAB-CFO and CFO nanoparticles in Di water (a) right after sonication and (b) after standing still for 10 min. (c-e) Dispersion of CTAB-CFO/CNC and CFO/CNC (c) right after sonication and after standing still for (d) 12 h and (e) 1 week.

The 0-1 connectivity ME composites were prepared from the dispersions with different MS nanoparticle concentrations of 5, 10 and 20 wt% (**Figure 4.5**). The 2.5 cm × 3.5 cm composites produced rigid films and their transparency was dependent on the CFO or CTAB-CFO concentrations. To avoid cracking of the composite films,

Al^{3+} ions were also introduced to stabilize the CNC network. However, it was found that cracking/breaking could not be avoided if the MS nanoparticles were over 25 wt%, as shown in **Figure 4.6**.

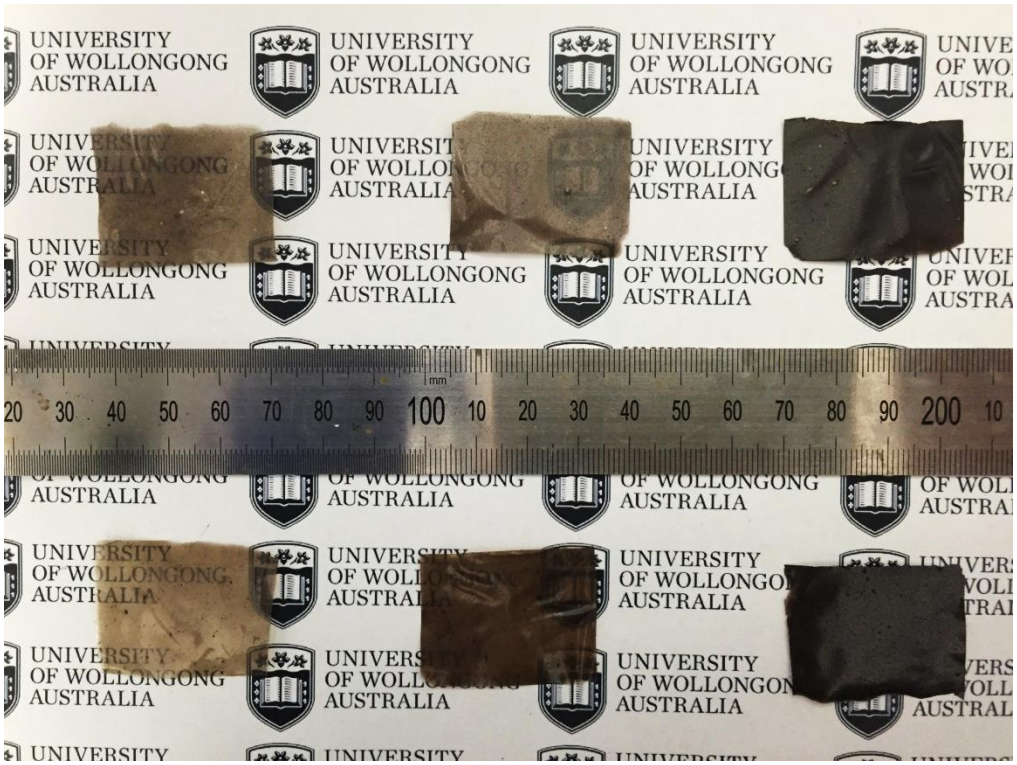

Figure 4.5. Appearance of CFO/CNC (upper row) and CTAB-CFO/CNC composites with different MS nanoparticle concentrations of 5, 10 and 20 wt% (from left to right)

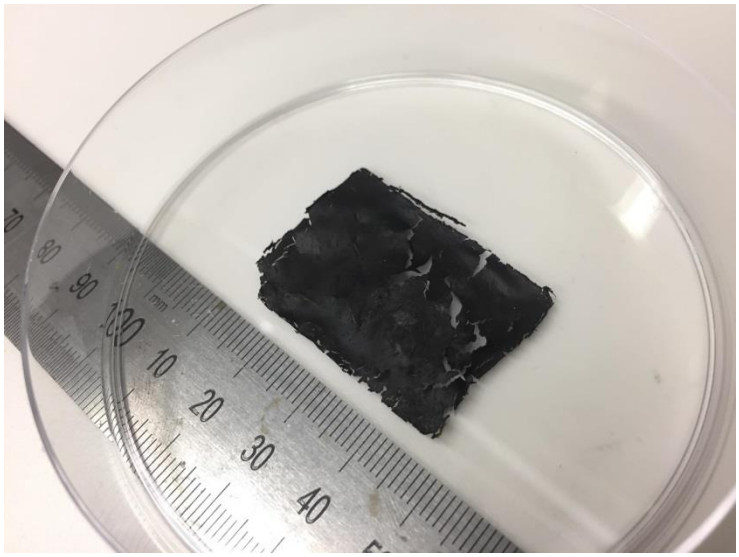

Figure 4.6. Representation of cracked sample with high magnetostrictive concentration. The sample is CFO/CNC composite containing 25 w.t.% of CFO nanoparticles (CFO:CNC=1:3).

The crystalline structure of the developed composites was investigated using XRD. Representative spectra of CFO/CNC and CTAB-CFO/CNC composites containing 20 wt% MS nanoparticles (**black curves)** in comparison with pure CFO and CTAB-CFO nanoparticles (**red curves)** were displayed in **Figure 4.7a and b**. The interference of CFO and CTAB-CFO nanoparticles showed good agreement with previously reported indices of cobalt ferrite,[38] and no impurities were observed in the spectra. Spectra of the 0-1 connectivity ME composites (CFO/CNC and CTAB-CFO/CNC) show the interference of CNC in the range from 13˚-25˚ combined with the characteristic peaks of the pure CFO and CTAB-CFO nanoparticles at diffraction angles from 30˚-65˚, confirming the coexistence of PE and MS phases in the composites. The interference

indices corresponding to the cellulose lattice (004) at 34.6˚ and CFO lattice (111) at 19.9˚ have low intensity and therefore were not observed in spectra of the composites. FT-IR spectra of pure CNC and the composites containing 5, 10, 20 wt% MS nanoparticles were displayed in **Figure 4.7c and d**. Compared to pure CNC nanowhiskers, the composites with MS nanoparticles show a series of absorption bands at 985, 1000 and 1015 cm^{-1}, which were all assigned to cellulose C-O. stretching.[39] These bonds suggested the interaction between MS particles and CNC nanowhiskers, however the mechanism that gave the aforementioned bonds needs further clarification.

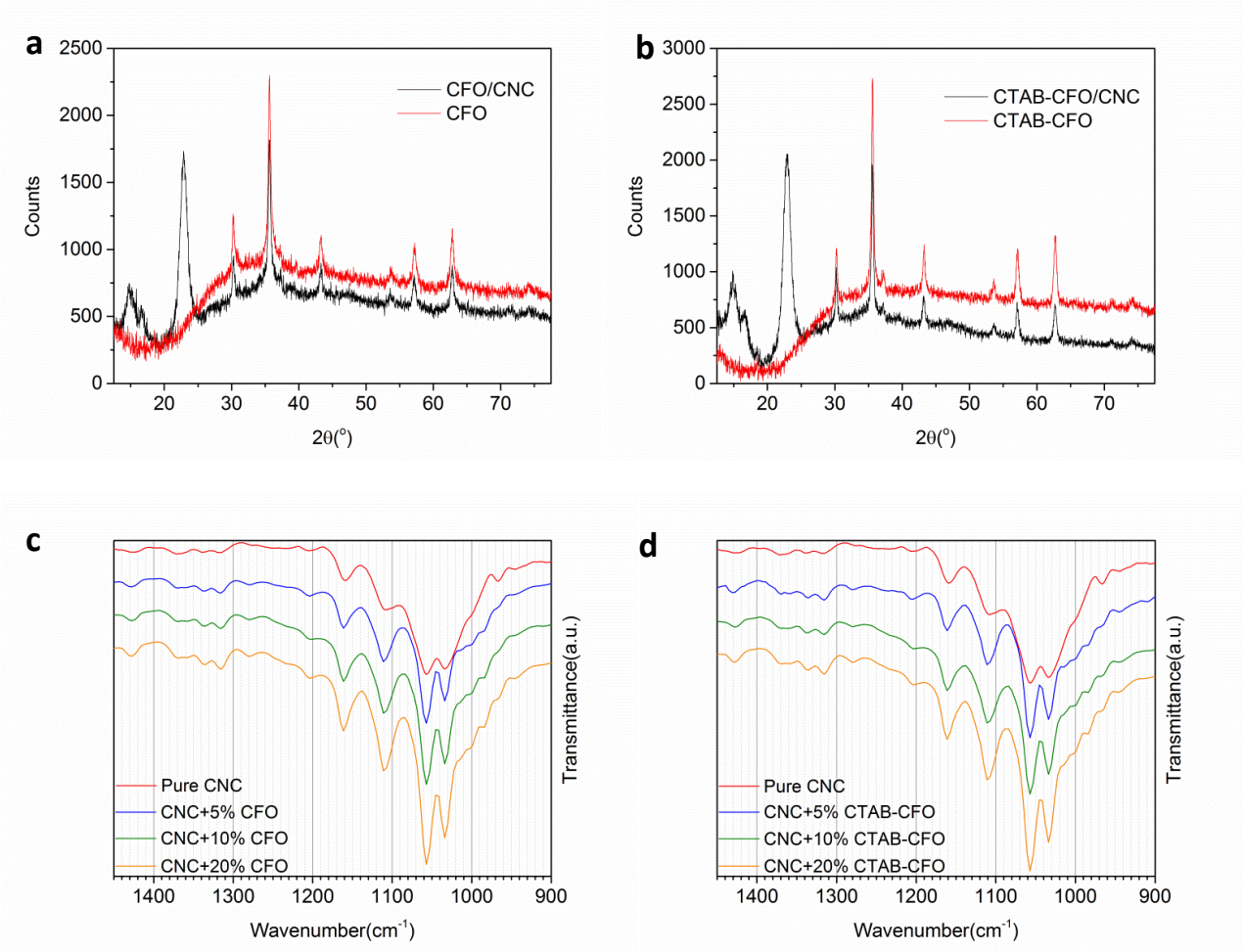

Figure 4.7. XRD patterns of (a) CFO nanoparticles and CFO/CNC composite and (b) CTAB-CFO nanoparticles and CTAB-CFO/CNC composite. The CFO/CTAB-CFO have interference rising at diffraction angles 2θ=18.5˚, 30.2˚, 35.6˚, 36.3˚, 43.3˚, 53.8˚, 57.2˚, 62.8˚ and 74.1˚ corresponding to lattice (111), (220), (311), (222), (400), (422), (511), (440) and (533). (c, d) FT-IR spectra of pure CNC and (c) CFO/CNC and (d) CTAB-CFO/CNC composites containing different w.t. ratios of magnetostrictive particles.

4.3.5. Surface Morphology of ME Composites

AFM was used to study the surface morphology of 0-1 connectivity ME composites containing 20 wt% of MS nanoparticles. AFM height images showed a relatively smooth surface for CFO/CNC composites with the appearance of some particulate regions (**Figure 4.8a**) although no clear observations of individual CFO nanoparticles were made when the scan size is reduced to 3 μm and only the CNC whiskers were observed (**Figure 4.8b**). The roughness of the two samples were calculated based on the 15 μm ×15 μm images (**Figure 4.8 a and c**). A low surface roughness (r.m.s = 9.34 nm) of CFO/CNC composites surface is attributed to the good dispersion ability of CFO nanoparticles. In contrast, significantly more particulate regions were observed on the CTAB-CFO/CNC with greater surface roughness with r.m.s = 80.34 nm) that may be due to surface aggregated nanoparticles (**Figure 4.8c**). Higher resolution images indicated that the presence of these aggregations with cellulose nanowhiskers showing clear separation from each other on the surface (**Figure 4.8d**).

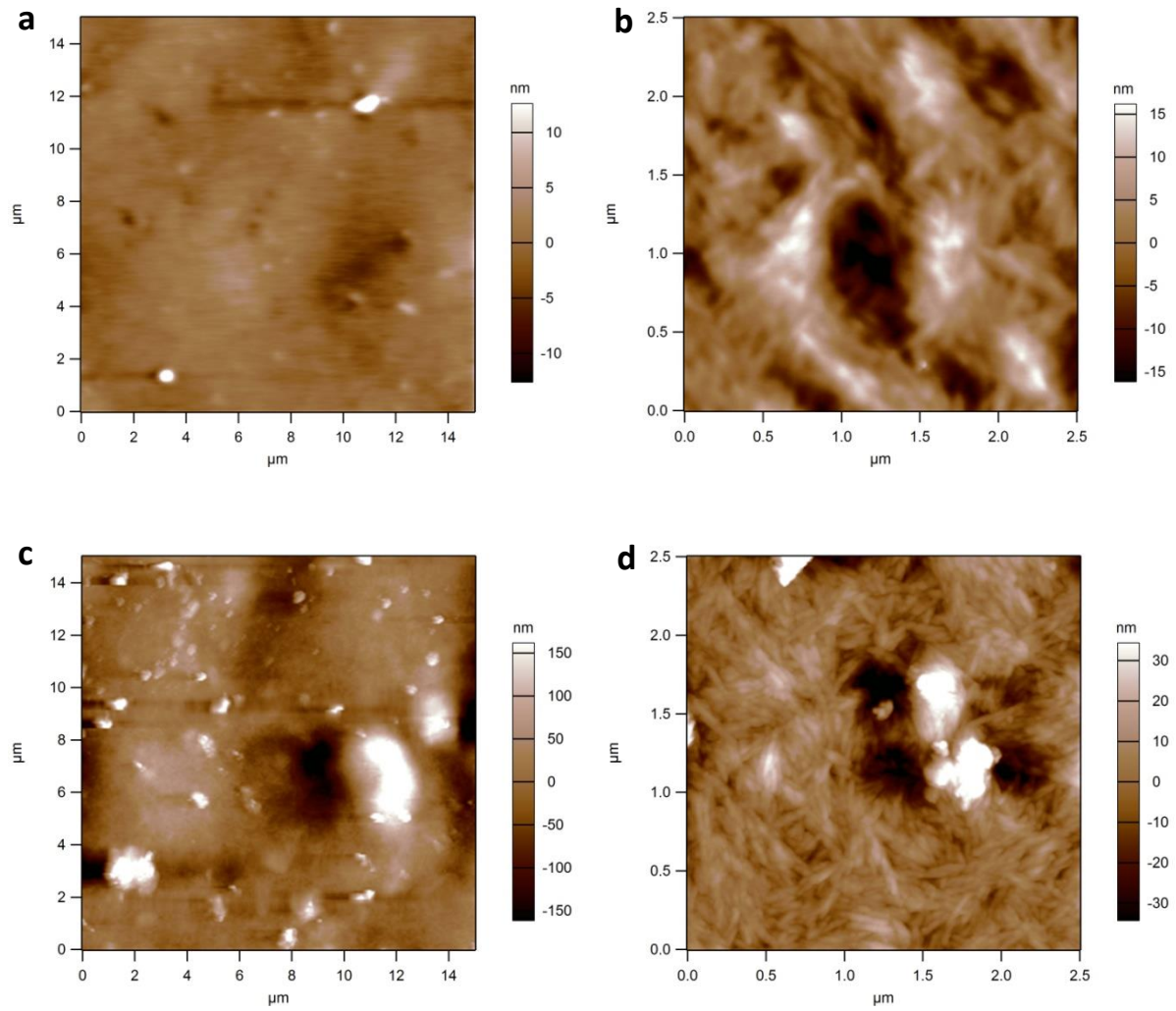

Figure 4.8. (a,b) Morphology of CFO/CNC composite with scanning size of (a) 15 µm ×15 µm and (b) 3 µm × 3 µm. (c,d) Morphology of CTAB-CFO/CNC composite with scanning size of (c) 15 µm ×15 µm and (d) 3 µm × 3 µm.

4.3.6. ME Effect of CFO/CNC and CTAB-CFO/CNC Composites

The ME composites were coated with surface electrodes on both sides (**Figure 4.1a**) and the ME measurements were performed in a bulk test system (**Figure 4.1b**) using a

dynamic method with an applied alternating magnetic field (H_{ac}) superimposed on a constant magnetic field (H_{dc}) to induce the ME output voltage. Based on this method, the ME voltage coefficient is evaluated using the following equation:[40]

$$\alpha_{ME} = \frac{V_{ME}}{T \times Hac} \quad (4.2)$$

where V_{ME} is the actual voltage output collected from surface electrodes, T is the thickness of piezoelectric film and H_{ac} is the strength of the alternating magnetic field. The thickness of the CFO/CNC and CTAB-CFO/CNC composites were in the range of 50-60 and 70-80 μm, respectively. The actual magnetic induced voltages (μV) are given later in **Figure 4.10**.

The bulk testing of the ME effect followed the method for nanoparticulate CFO/PVDF ME composites early reported.[26] For all measurements, H_{ac} was fixed at 0.6 Oe with frequency of 5 KHz.[26] As such, only the ME effect dependence on H_{ac} values were studied in this chapter. In particular, the α_{ME} is recorded according to gradually increased H_{ac} strength. **Figure 4.9** showed that no clear ME response was observed for CFO/CNC and CTAB-CFO/CNC composites containing 5 wt% of magnetic nanoparticles, most likely due to insufficient magnetostriction to induce strain required for a measurable ME effect. At higher concentrations of MS nanoparticles, an ME effect is observed with composites containing 20 wt% MS nanoparticles giving a higher value of α_{ME} compared to those have 10 wt.% concentration (**Figure 4.9**) regardless of the type of MS nanoparticles. Specifically, α_{ME} from 10 wt% CFO/CNC composites (**Figure 4.9a**, **red trace**) gradually increases

until peaking at ~1800 Oe (**Point A,** 0.039 mV cm^{-1} Oe^{-1}) followed by a second peak at ~2700 Oe (**Point B,** 0.038 mV cm^{-1} Oe^{-1}). For the 20 wt% CFO/CNC composites (**Figure 4.9a**, **black trace**), again the α_{ME} gradually increases with an increase in H_{dc}, consisting of two similar peaks of 0.110 mV cm^{-1} Oe^{-1} (**Point C**) at 1819 Oe and 0.135 mV cm^{-1} Oe^{-1} (**Point D**) at 2700 Oe (**Figure 4.9a, black trace**). The first peak is suggested to be associated with the MS properties of CFO nanoparticles of which the saturation is achieved ~1800 Oe and was in good agreement with previously studied particulate CFO/PVDF ME composites.[11,37] However, the origin of the second peak at 2700 Oe is at present not clear. Comparably, the α_{ME} from CTAB-CFO/CNC composites reached a plateau at ~800 Oe and ~1500 Oe for 10 wt% and 20 wt% concentrated samples, respectively. For both concentrations, the ME effect reduced dramatically after the magnetic saturation at ~2000 Oe and eventually reaches 0 at the maximum H_{dc} of 3000 Oe (**Figure 4.9b**). Compared to CTAB-CFO/CNC, the CFO/CNC composites have a better overall performance. The peak values of ME output voltages from 10 wt% and 20 wt% CFO/CNC samples were 0.55 and 0.15 μV (**Figure 4.10a,c**) compared to the peaks of 0.25 and 0.12 μV (**Figure 4.10b,d**) for CTAB-CFO samples. The higher ME output voltages of CFO samples were attributed to their better dispersion ability in the composite. The concentrations of 5 wt% CFO and CTAB-CFO were too low to induce an ME effect and the recorded voltage in the range of 0-0.05 μV was in the background noise of the measurement (**Figure 4.10e and f**).

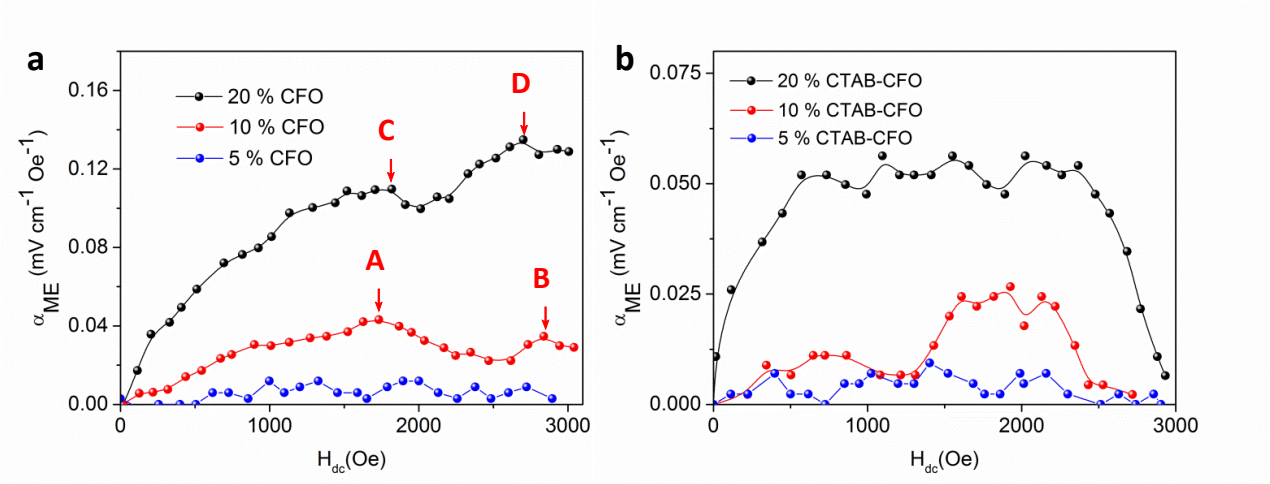

Figure 4.9. α_{ME} as a function of H_{dc} for (a) CFO/CNC and (b) CTAB-CFO/CNC composites with magnetostrictive concentrations of 10 wt% and 20 wt%.

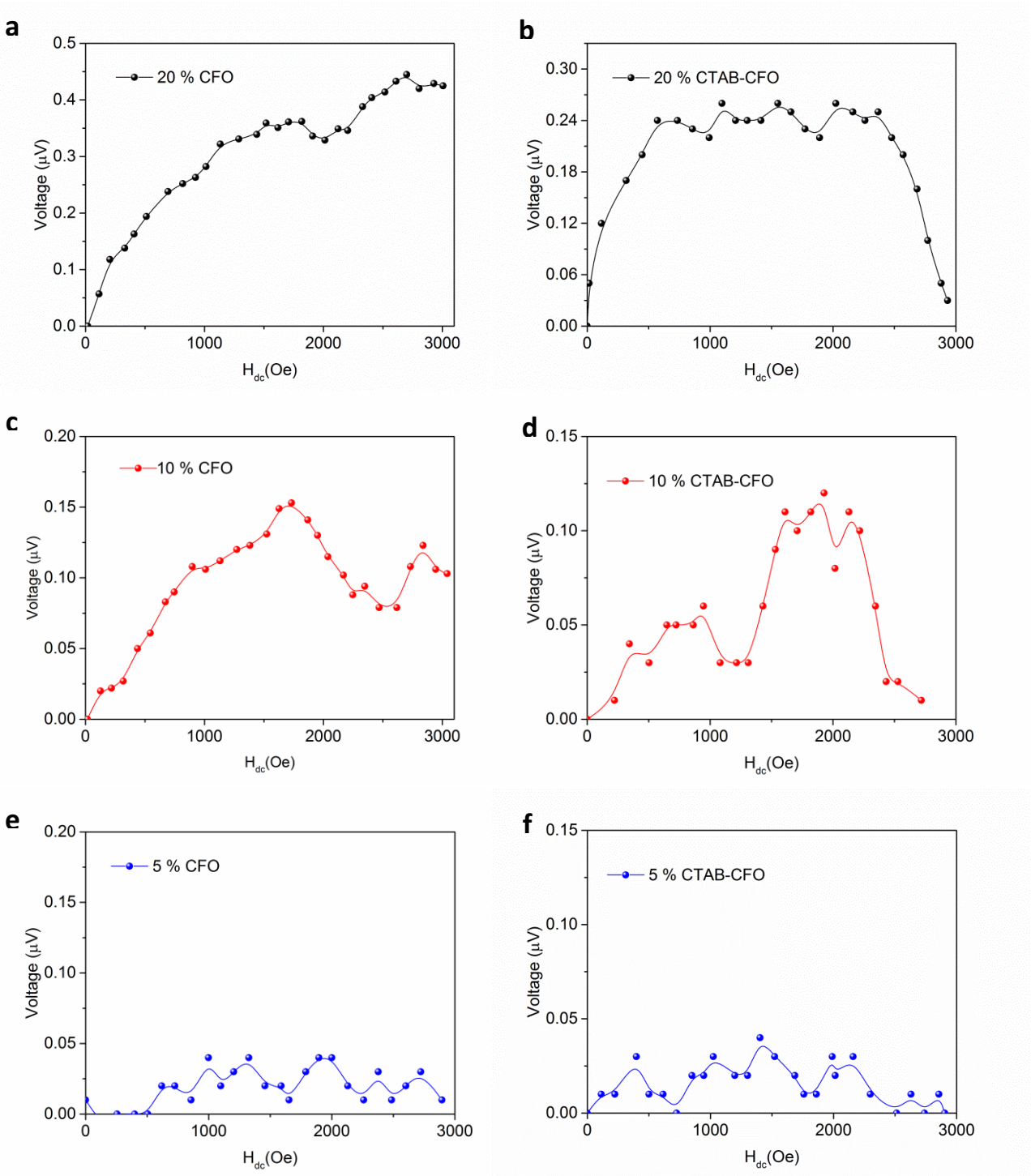

Figure 4.10. Magnetically induced voltage as a function of H_{dc} for CFO/CNC composites containing (a) 20 w.t.%, (c) 10 w.t.% and (e) 5 w.t.% of CFO nanoparticles; and CTAB-CFO/CNC composites containing (b) 20 w.t.%, (d) 10 w.t.% and (f) of 5 w.t.% CFO nanoparticles. The thicknesses of measured samples were: (a) 55, (b) 77, (c) 59, (d) 75, (e) 56 and (f) 71 μm.

4.4. Conclusion

In conclusion, an ME coupling in 0-1 connectivity was proposed and has been successfully verified in this work. To the best of our knowledge, this is the first ME composite with 0-1 connectivity. Strong hydrogen bonding between the hydrophilic surfaces of CFO and CNC improved the dispersion of MS nanoparticles and gave rise to the highest α_{ME} of 0.135 mV cm^{-1} Oe^{-1} in a CFO/CNC ME composite with MS concentration of 20 w.t.%. Also, the amount of the MS nanoparticles played a role in the ME effect, with higher concentrated sample producing the greatest ME output voltage. The ME response of CFO/CNC or CTAB-CFO/CNC composites is not as high as PVDF based particulate ME composites in 0-3 connectivity,[26] which is due to the limited piezoelectric property of cellulose. Compared to ME laminates which usually generate a giant ME effect of α_{ME}>1 V cm^{-1} Oe^{-1}, the ME voltage of 0-1 connectivity ME composites is relatively low level. This is mainly due the structural merit of 2-2 connectivity of ME laminate for strain transfer.[41] However, the work provides a new concept for a novel ME coupling connectivity and opens up the possibility of using different types of combinations of 0-D and 1D MS and PE materials to investigate ME composites, which are further discussed below in the Summary/Perspectives Chapter.

4.5. References

1 Dong, S., Zhai, J., Li, J. & Viehland, D. Near-ideal magnetoelectricity in high-permeability magnetostrictive/piezofiber laminates with a (2-1) connectivity. *Appl. Phys. Lett.* **89**, 252904, (2006).

2 Eerenstein, W., Mathur, N. & Scott, J. F. Multiferroic and magnetoelectric materials. *nature* **442**, 759-765, (2006).

3 Spaldin, N. A. & Fiebig, M. The Renaissance of Magnetoelectric Multiferroics. *Science* **309**, 391-392, (2005).

4 Nan, C.-W., Bichurin, M. I., Dong, S., Viehland, D. & Srinivasan, G. Multiferroic magnetoelectric composites: Historical perspective, status, and future directions. *J. Appl. Phys.* **103**, 031101, (2008).

5 Hu, J.-M., Chen, L.-Q. & Nan, C.-W. Multiferroic Heterostructures Integrating Ferroelectric and Magnetic Materials. *Adv. Mater.* **28**, 15-39, (2016).

6 Ma, J., Hu, J., Li, Z. & Nan, C.-W. Recent Progress in Multiferroic Magnetoelectric Composites: from Bulk to Thin Films. *Adv. Mater.* **23**, 1062-1087, (2011).

7 Suchtelen, J. v. *Philips Res. Rep.* **27**, 28-37, (1972).

8 Palneedi, H., Annapureddy, V., Priya, S. & Ryu, J. Status and Perspectives of Multiferroic Magnetoelectric Composite Materials and Applications. *Actuators* **5**, 9, (2016).

9 Li, Y. *et al.* Magnetoelectric quasi-(0-3) nanocomposite heterostructures. *Nat Commun* **6**, 6680, (2015).

10 Islam, R. A., Bedekar, V., Poudyal, N., Liu, J. P. & Priya, S. Magnetoelectric properties of core-shell particulate nanocomposites. *J. Appl. Phys.* **104**, 104111, (2008).

11 Etier, M. *et al.* The Direct and the Converse Magnetoelectric Effect in Multiferroic Cobalt Ferrite–Barium Titanate Ceramic Composites. *J. Am. Ceram. Soc.* **99**, 3623-3631, (2016).

12 Islam, R. A., Ni, Y., Khachaturyan, A. G. & Priya, S. Giant magnetoelectric effect in sintered multilayered composite structures. *J. Appl. Phys.* **104**, 044103, (2008).

13 Wang, Y. *et al.* An Extremely Low Equivalent Magnetic Noise Magnetoelectric Sensor. *Adv. Mater.* **23**, 4111-4114, (2011).

14 Ryu, J., Priya, S., Carazo, A. V., Uchino, K. & Kim, H.-E. Effect of the Magnetostrictive Layer on Magnetoelectric Properties in Lead Zirconate Titanate/Terfenol-D Laminate Composites. *J. Am. Ceram. Soc.* **84**, 2905-2908, (2001).

15 Ma, J., Shi, Z. & Nan, C. W. Magnetoelectric Properties of Composites of Single Pb(Zr,Ti)O3 Rods and Terfenol-D/Epoxy with a Single-Period of 1-3-Type Structure. *Adv. Mater.* **19**, 2571-2573, (2007).
16 Lam, K. H., Lo, C. Y. & Chan, H. L. W. Frequency response of magnetoelectric 1–3-type composites. *J. Appl. Phys.* **107**, 093901, (2010).
17 Shi, Z., Nan, C.-W., Zhang, J., Ma, J. & Li, J.-F. Magnetoelectric properties of multiferroic composites with pseudo-1-3-type structure. *J. Appl. Phys.* **99**, 124108, (2006).
18 Chu, Z. *et al.* Enhanced Resonance Magnetoelectric Coupling in (1-1) Connectivity Composites. *Adv. Mater.* **29**, 1606022-n/a, (2017).
19 Nan, C.-W. *et al.* A three-phase magnetoelectric composite of piezoelectric ceramics, rare-earth iron alloys, and polymer. *Appl. Phys. Lett.* **81**, 3831-3833, (2002).
20 Chau, K. H., Wong, Y. W. & Shin, F. G. Magnetoelectric effect of polymer electrolyte composites with Terfenol-D and lead zirconate titanate inclusions. *Appl. Phys. Lett.* **94**, 202902, (2009).
21 Lagerwall, J. P. F. *et al.* Cellulose nanocrystal-based materials: from liquid crystal self-assembly and glass formation to multifunctional thin films. *NPG Asia Mater* **6**, e80, (2014).
22 Habibi, Y., Lucia, L. A. & Rojas, O. J. Cellulose Nanocrystals: Chemistry, Self-Assembly, and Applications. *Chemical Reviews* **110**, 3479-3500, (2010).
23 Cao, S.-L., Li, X.-H., Lou, W.-Y. & Zong, M.-H. Preparation of a novel magnetic cellulose nanocrystal and its efficient use for enzyme immobilization. *Journal of Materials Chemistry B* **2**, 5522-5530, (2014).
24 Lizundia, E., Maceiras, A., Vilas, J. L., Martins, P. & Lanceros-Mendez, S. Magnetic cellulose nanocrystal nanocomposites for the development of green functional materials. *Carbohydr. Polym.* **175**, 425-432, (2017).
25 Martins, P. *et al.* Role of Nanoparticle Surface Charge on the Nucleation of the Electroactive β-Poly(vinylidene fluoride) Nanocomposites for Sensor and Actuator Applications. *The Journal of Physical Chemistry C* **116**, 15790-15794, (2012).
26 Martins, P. *et al.* Optimizing piezoelectric and magnetoelectric responses on CoFe 2 O 4 /P(VDF-TrFE) nanocomposites. *J. Phys. D: Appl. Phys.* **44**, 495303, (2011).
27 Brian, J. R., Clint, C., Sergei, V. K. & Roger, P. Dual-frequency resonance-tracking atomic force microscopy. *Nanotechnology* **18**, 475504, (2007).
28 Sun, B. *et al.* Further characterization of cellulose nanocrystal (CNC) preparation from sulfuric acid hydrolysis of cotton fibers. *Cellulose* **23**, 439-450, (2016).
29 Nelson, M. L. & O'Connor, R. T. Relation of certain infrared bands to cellulose crystallinity and crystal lattice type. Part II. A new infrared ratio for

estimation of crystallinity in celluloses I and II. *J. Appl. Polym. Sci.* **8**, 1325-1341, (1964).

30 Zong, Y. *et al.* Cellulose-based magnetoelectric composites. *Nature Communications* **8**, 38, (2017).

31 Segal, L., Creely, J. J., A.E. Martin, Jr. & Conrad, C. M. An Empirical Method for Estimating the Degree of Crystallinity of Native Cellulose Using the X-Ray Diffractometer. *Textile Research Journal* **29**, 786-794, (1959).

32 Jesse, S., Baddorf, A. P. & Kalinin, S. V. Switching spectroscopy piezoresponse force microscopy of ferroelectric materials. *Appl. Phys. Lett.* **88**, 062908, (2006).

33 Polking, M. J. *et al.* Ferroelectric order in individual nanometre-scale crystals. *Nat Mater* **11**, 700-709, (2012).

34 Maaz, K., Mumtaz, A., Hasanain, S. K. & Ceylan, A. Synthesis and magnetic properties of cobalt ferrite (CoFe2O4) nanoparticles prepared by wet chemical route. *J. Magn. Magn. Mater.* **308**, 289-295, (2007).

35 Song, Q. & Zhang, Z. J. Shape Control and Associated Magnetic Properties of Spinel Cobalt Ferrite Nanocrystals. *J. Am. Chem. Soc.* **126**, 6164-6168, (2004).

36 Nan, C. W., Li, M. & Huang, J. H. Calculations of giant magnetoelectric effects in ferroic composites of rare-earth\char21{}iron alloys and ferroelectric polymers. *Phys. Rev. B* **63**, 144415, (2001).

37 Zhang, J. X. *et al.* The effect of magnetic nanoparticles on the morphology, ferroelectric, and magnetoelectric behaviors of CFO/P(VDF-TrFE) 0–3 nanocomposites. *J. Appl. Phys.* **105**, 054102, (2009).

38 Pillai, V. & Shah, D. O. Synthesis of high-coercivity cobalt ferrite particles using water-in-oil microemulsions. *J. Magn. Magn. Mater.* **163**, 243-248, (1996).

39 Liang, C. Y. & Marchessault, R. H. Infrared spectra of crystalline polysaccharides. II. Native celluloses in the region from 640 to 1700 cm.−1. *J. Polym. Sci.* **39**, 269-278, (1959).

40 Reis, S. *et al.* Electronic optimization for an energy harvesting system based on magnetoelectric Metglas/poly(vinylidene fluoride)/Metglas composites. *Smart Mater. Struct.* **25**, 085028, (2016).

41 Srinivasan, G. Magnetoelectric Composites. *Annu. Rev. Mater. Res.* **40**, 153-178, (2010).

Chapter 5. Summary and Perspectives

5.1. Summary of the Thesis

The thesis introduced a new concept of using naturally occurring biopolymers as the piezoelectric component for ME composites that was successfully validated using different forms of cellulose biopolymers, including regenerated cellulose and nanocrystalline cellulose in the form of nanowhiskers and nanospheres. Generally, the ME coupling connectivity and cellulose crystallinity were found to be the main factors that influenced the performance of all ME composites. Compared to other connectivities, the 2-2 laminate structure was the most efficient for ME strain coupling and gives rise to a high ME coefficient. In addition, the cellulose ME laminates in **Chapters 2 and 3** produced ME output voltages at the millivolt level, which was an order higher than the 0-1 connectivity ME composites in **Chapter 4**.

The PE properties of cellulose was related to its crystallinity. Higher crystallinity improved the piezoelectricity of cellulose and gave rise to an enhanced ME response. In **Chapter 3**, highly crystalline cellulose CNC was employed as the PE material. Compared to regenerated cellulose, the CNC shows much better overall piezoresponse and the highest α_{ME} of 2.33 V cm^{-1} Oe^{-1} was observed for the CNC nanosphere ME laminate whereas the highest α_{ME} of 1.41 V cm^{-1} Oe^{-1} was observed for the regenerated cellulose.

As shown in **Chapter 2 and 3**, water content plays a significant role in the profile of the Fano-resonance enhanced ME effect. The degree of water content can give rise to different Fano resonance profiles where the anti-resonance peak could be located either at higher or lower frequencies relative to the resonance peak value. However, the samples with no residual water showed that a Fano-resonance profile with an anti-resonance peak that only occurred at a higher frequency relative to the resonance peak value. Moreover, it was found that higher water content can increase the damping factor of the Fano-resonance profile. As such, a narrower peak was observed from samples dried under high temperature while a broader peak could be observed from air-dried samples consisting a greater amount of residual water.

In **Chapter 4**, ME coupling was constructed in a nanoscale 0-1 connectivity and the dispersion properties of MS nanoparticles in the composite was a key factor for enabling a stronger ME effect. In this case, the hydrophilic CFO nanoparticles appeared better dispersed than the hydrophobic CTAB-CFO nanoparticles and produced greater ME output voltages.

Herein, the key findings are list below:

1. First polymer-based ME composite fabricated using a biopolymer
2. First experimentally observed Fano-resonance enhanced ME effect
3. First anisotropic ME response produced from an ME composite with a polymeric piezoelectric component
4. First ME coupling constructed in a 0-1 connectivity
5. First observation of a cellulose crystal II lattice in nanocrystalline cellulose

5.2. Suggested Future Work

This thesis opens a new pathway for the development of natural biopolymer-based ME composites. Future work is suggested to focus on different types of piezoelectric and magnetostrictive materials, and to construct novel connectivities in the nanoscale domain. Some suggestions for future experimental work beyond this thesis are described below.

5.2.1. Cellulose Nanofibrils (CNF)

CNC produced from an acid hydrolysis process was shown to be a promising piezoelectric material for ME composites. The high crystallinity degree gives a higher piezoelectric response and consequently leads to a higher ME effect than for the regenerated cellulose-based ME composites. The CNC 1-dimensional (1D) nanomaterial also possesses unique properties which can be used to process and align the CNC nanowhiskers to produce an anisotropic ME effect. However, one problem is that the CNC nanowhisker films are brittle and not suitable for applications involving flexible electronic devices. Considering this, cellulose nanofibrils (CNF) made by 2,2,6,6-tetramethylpiperidine-N-oxyl (TEMPO) oxidization is highly recommended. Similar to CNC, the CNF is also the structural component of natural cellulose fibers existing in wood or other plants. It maintains the cellulose crystal I lattice and high crystallinity which is expected to produce a considerable piezoelectric response.[1] CNF can be synthesised by different oxidization methods and the solution involving

NaClO/NaBr/TEMPO is the most commonly used one.[1] During the synthesis process the three oxidization agents play roles at different stages and all of them are recyclable (**Scheme 5.1**), thus meeting the requirements of green chemistry.[2] The oxidized CNF has surface carboxylate groups that ensure good dispersion ability of CNF in aqueous conditions. Moreover, it was found that when the carboxylate content reaches a certain value (*e.g.* 1.5 mmol/g for soft wood pulp CNF) the aqueous suspension becomes transparent,[3] making it suitable for optical materials or other materials requiring high transparency.

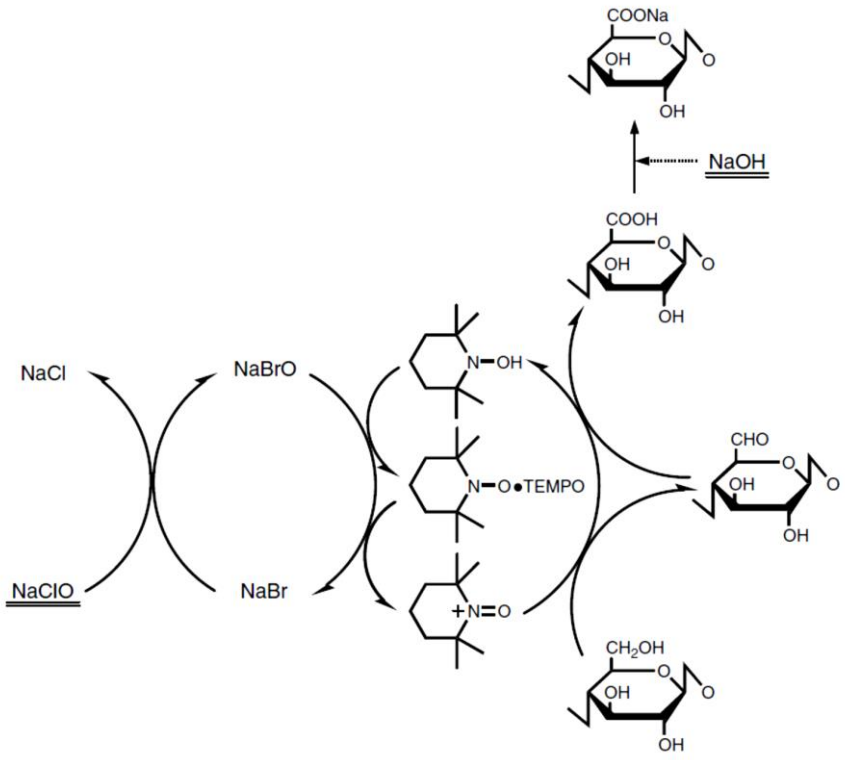

Scheme 5.1. TEMPO mediated oxidization of cellulose.[2]

TEMPO oxidized cellulose shows a fibril structure with higher aspect ratio than acid hydrolyzed cellulose nanocrystal (CNC). The length of CNF can reach up to a few microns (**Figure 5.1a**)[3] compared to that of CNC of only hundreds of nanometers in

length. Because of this, the CNF film has improved mechanical properties (10.0 ±1.7 GPa)[4] and is optically transparent (**Figure 5.1b**)[5]. It is also thermally stable and light weight of which the density is approximately 1.45-1.47 g cm^{-3}.[6] Owing to these unique properties, the free standing CNF film could be used for practical devices such as electronic displays or touch screen substrates (**Figure 5.1c,d**),[7,8] and is considered to be a promising candidate for use in more flexible ME composites electronic devices.

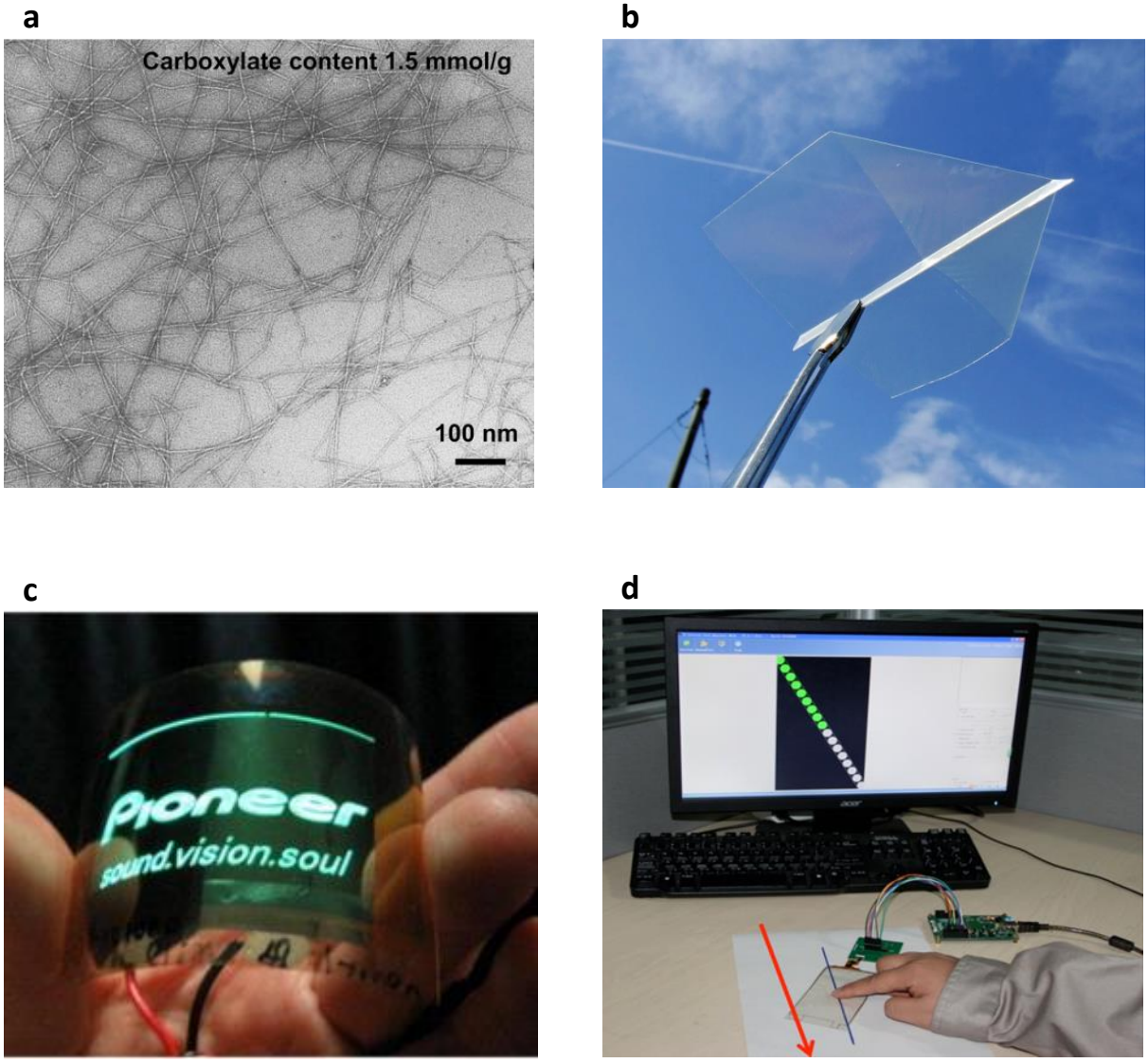

Figure 5.1. (a) TEM image of TEMPO oxidized CNF dispersion.[3] (b) CNF free standing film with good transparency and mechanical property.[5] (c) Luminescence of an organic light-emitting diode deposited onto a flexible and optically transparent wood–cellulose nanocomposite.[7] (d) Measurement of linearity of a CNF touch screen.[8]

5.2.2. Magnetic Nanowires

Future work on the MS materials, particularly on nanowires (NW) in the form of either a single metal or an alloy would be of interest and have potential impact.

Specifically, two types of nanowires are suggested to be considered: the nickel and Galfenol NWs. Ni is a negatively MS that shrinks along the longitudinal direction of the applied magnetic field. Because of its low permittivity the Ni-based ME composites possess a self-biased behaviour and are very suitable for low frequency energy harvesting applications (**Chapter 1)**.[9] Galfenol generally refers to an alloy of iron and gallium consisting of $Fe_{100-x}Ga_x$ with x from 13-29%.[10] It is a highly MS material that was originally developed and named by the U.S. Navy for sonar applications, and the magnetostriction of Galfenol NW can reach up to 300 ppm.[11]

MS NWs could be fabricated using electrodeposition methods combined with an anodic aluminum oxide (AAO) membrane. The AAO membrane shows an ordered and homogenous porous structure (**Figure 5.2a**), which provides a template for the growth of single metal NWs or the repeatable growth of alloy NWs.[12] Briefly, the electrodeposition process takes place in a solution containing desired metal ions and the chemical reduction occurs on the template of the AAO membrane until the expected length of the NWs is reached. NWs are then obtained by removing the AAO membrane, leaving the NWs standing on the back electrode substrate (**Figure 5.2b,c**).[13,14]

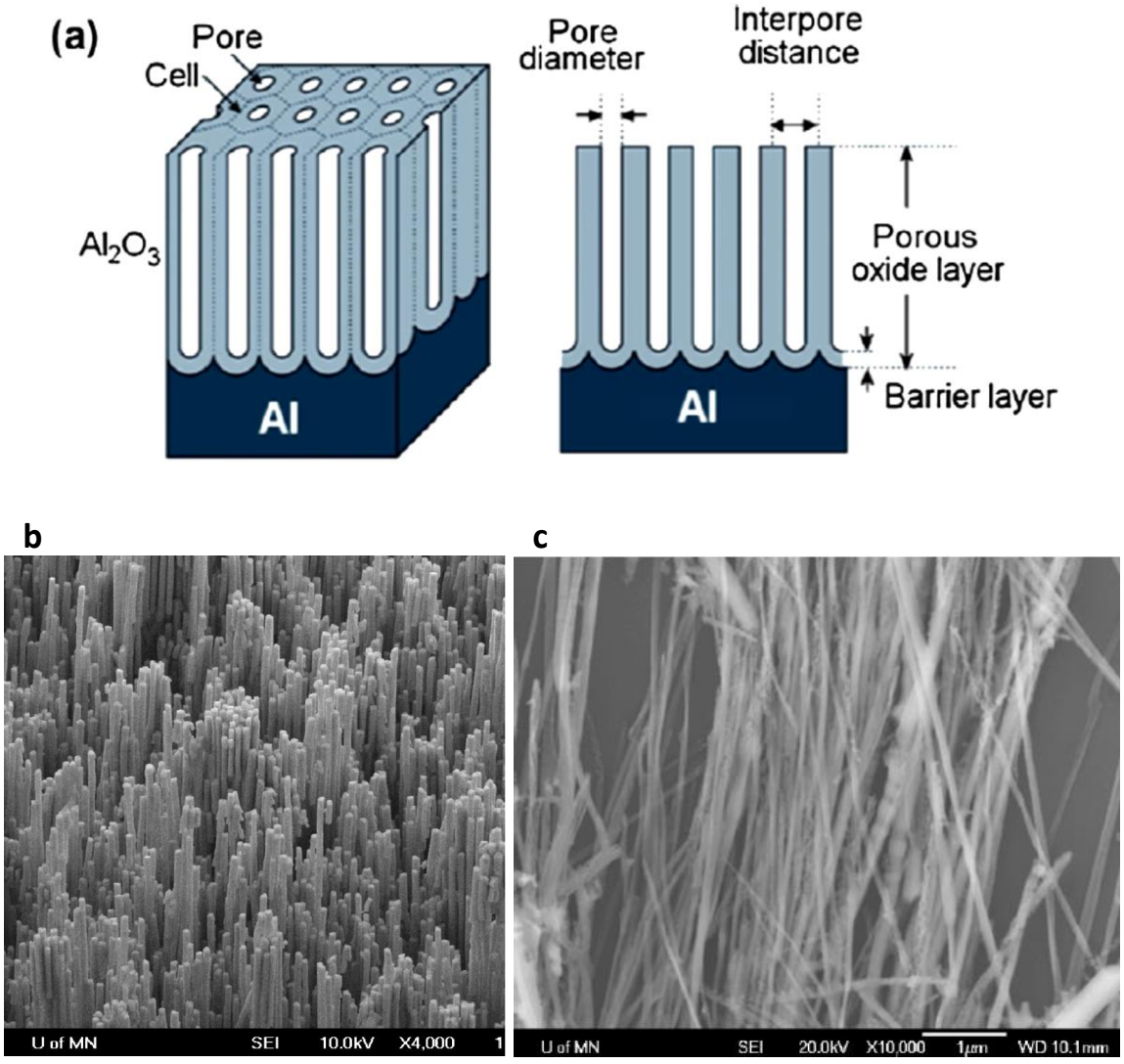

Figure 5.2. (a) Schematic view of AAO membrane.[12] (b,c) SEM images of (b) Ni and (c) galfenol NWs.[13,14]

5.2.3. ME Composites with 1-1 Connectivity

The ME nanocomposites consisting of CNF and magnetostrictive NWs are expected to show enhanced ME coupling compared to particulate ME composites developed in Chapter 4, and are hypothesised to possess unique physical properties. Firstly, the CNF and NWs are all 1-dimentional (1-D) materials, therefore the ME coupling is regarded as a novel nanoscopic 1-1 connectivity. Compared to MS nanoparticles such as Fe_3O_4,[15] NWs have a larger interface area for strain transfer that is expected to increase the ME response by several folds or even an order of magnitude higher than CFO/CNC nanocomposites developed in **Chapter 4**. This hypothesis is based on a study of Galfenol NW/PVDF ME composite that achieved an α_{ME} of over 100 mV cm^{-1} Oe^{-1} in comparison to the highest value of ~40 mV cm^{-1} Oe^{-1} for CFO/PVDF composites.[16,17] Also, the magnetically aligned MS NWs are capable of producing an anisotropic ME effect.[16] It is hypothesised that the interplay of aligned CNF and NW could enhance the anisotropic ME output voltage, in addition to the ME composite bearing greater flexibility than the CNC based laminates demonstrated in **Chapter 3**. Lastly and importantly, the high aspect ratio of the CNF and NW ensure a high transparency of the composites, which could be useful as a self-powered substrate for electronic displays. In addition to cellulose derivatives, there are also exciting possibilities in exploring the use of other naturally occurring piezoelectric polymers such as chitin,[18] peptides[19] and viruses[20].

5.3. References

1 Isogai, A., Saito, T. & Fukuzumi, H. TEMPO-oxidized cellulose nanofibers. *Nanoscale* **3**, 71-85, (2011).

2 Saito, T., Okita, Y., Nge, T. T., Sugiyama, J. & Isogai, A. TEMPO-mediated oxidation of native cellulose: Microscopic analysis of fibrous fractions in the oxidized products. *Carbohydr. Polym.* **65**, 435-440, (2006).

3 Saito, T., Kimura, S., Nishiyama, Y. & Isogai, A. Cellulose Nanofibers Prepared by TEMPO-Mediated Oxidation of Native Cellulose. *Biomacromolecules* **8**, 2485-2491, (2007).

4 Fujisawa, S., Okita, Y., Fukuzumi, H., Saito, T. & Isogai, A. Preparation and characterization of TEMPO-oxidized cellulose nanofibril films with free carboxyl groups. *Carbohydr. Polym.* **84**, 579-583, (2011).

5 Nogi, M., Iwamoto, S., Nakagaito, A. N. & Yano, H. Optically Transparent Nanofiber Paper. *Adv. Mater.* **21**, 1595-1598, (2009).

6 Fukuzumi, H., Saito, T., Iwata, T., Kumamoto, Y. & Isogai, A. Transparent and High Gas Barrier Films of Cellulose Nanofibers Prepared by TEMPO-Mediated Oxidation. *Biomacromolecules* **10**, 162-165, (2009).

7 Okahisa, Y., Yoshida, A., Miyaguchi, S. & Yano, H. Optically transparent wood–cellulose nanocomposite as a base substrate for flexible organic light-emitting diode displays. *Composites Science and Technology* **69**, 1958-1961, (2009).

8 Zhu, H. *et al.* Extreme Light Management in Mesoporous Wood Cellulose Paper for Optoelectronics. *ACS Nano* **10**, 1369-1377, (2016).

9 Ryu, J. *et al.* Ubiquitous magneto-mechano-electric generator. *Energy Environ. Sci.* **8**, 2402-2408, (2015).

10 Downey, P. R. & Flatau, A. B. Magnetoelastic bending of Galfenol for sensor applications. *J. Appl. Phys.* **97**, 10R505, (2005).

11 Engdahl, G. & Mayergoyz, I. D. *Handbook of Giant Magnetostrictive Materials*. (Elsevier Science, 1999).

12 Md Jani, A. M., Losic, D. & Voelcker, N. H. Nanoporous anodic aluminium oxide: Advances in surface engineering and emerging applications. *Prog. Mater Sci.* **58**, 636-704, (2013).

13 McGary, P. D. *et al.* Magnetic nanowires for acoustic sensors (invited). *J. Appl. Phys.* **99**, 08B310, (2006).

14 McGary, P. D. & Stadler, B. J. H. Electrochemical deposition of Fe1−xGax nanowire arrays. *J. Appl. Phys.* **97**, 10R503, (2005).

15 Martins, P., Kolen'ko, Y. V., Rivas, J. & Lanceros-Mendez, S. Tailored Magnetic and Magnetoelectric Responses of Polymer-Based Composites. *ACS Appl. Mater. Interfaces.* **7**, 15017-15022, (2015).

16 Alnassar, M. Y., Ivanov, Y. P. & Kosel, J. Flexible Magnetoelectric Nanocomposites with Tunable Properties. *Advanced Electronic Materials* **2**, 1600081-n/a, (2016).

17 Martins, P. *et al.* Optimizing piezoelectric and magnetoelectric responses on CoFe 2 O 4 /P(VDF-TrFE) nanocomposites. *J. Phys. D: Appl. Phys.* **44**, 495303, (2011).

18 Jin, J. *et al.* Chitin Nanofiber Transparent Paper for Flexible Green Electronics. *Adv. Mater.* **28**, 5169-5175, (2016).

19 Nguyen, V., Zhu, R., Jenkins, K. & Yang, R. Self-assembly of diphenylalanine peptide with controlled polarization for power generation. *Nature Communications* **7**, 13566, (2016).

20 Lee, B. Y. *et al.* Virus-based piezoelectric energy generation. *Nat Nano* **7**, 351-356, (2012).

Appendix

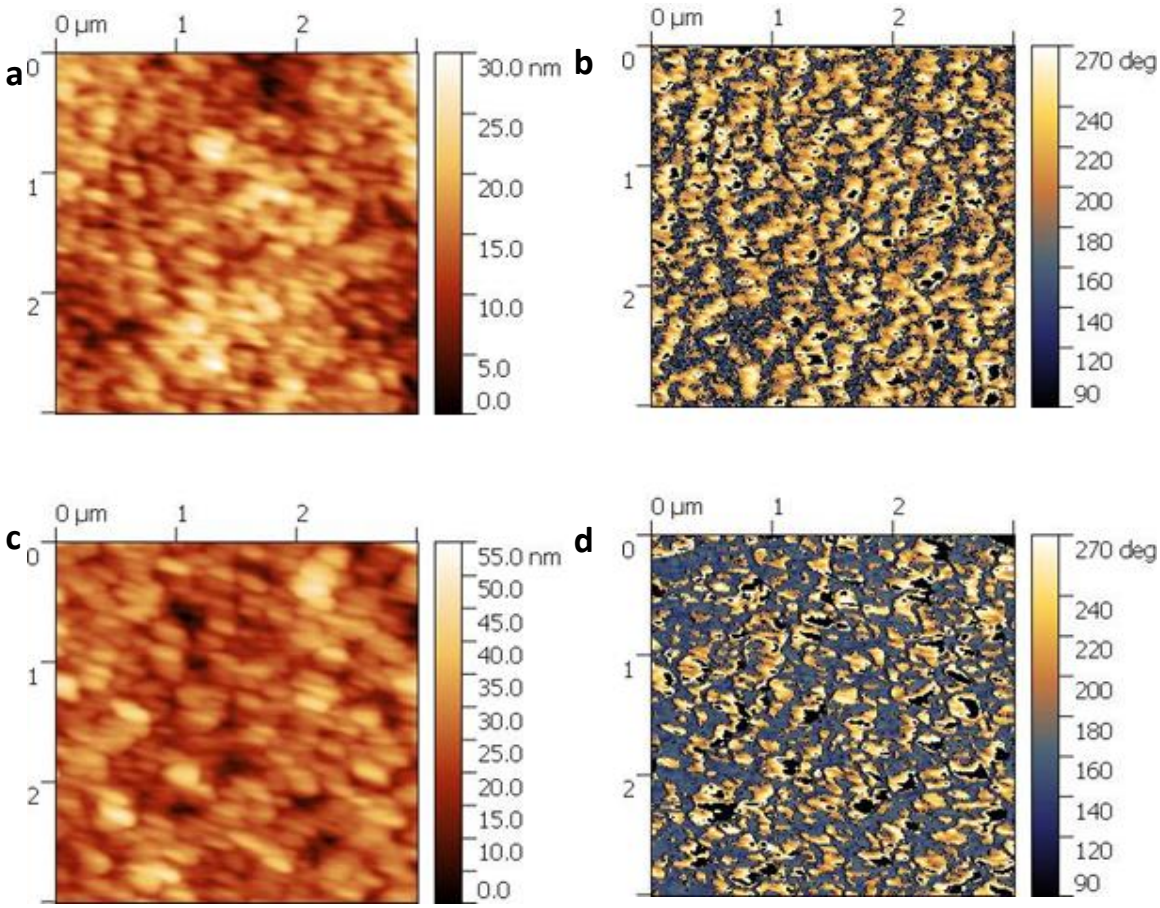

Figure A1. PFM (a) height and (b) phase images of hot-pressed (60 ℃) cellulose film, and (c) height and (d) phase images of air-dried cellulose film. A conductive tip was used to apply a constant amplitude of 9.4 V to induce local ME displacement while imaging.

PFM height and phase images corresponding to **Figure 2.9 a,b.** The height images reveal topography did not significantly differ (**Figure A1a and c**), while the spatial distribution of the PE nanoscale domains were similar for the hot-pressed versus

air-dried samples (**Figure 2.9**). Conversely, the phase (**Figure A1b and d**) and amplitude signal (**Figure 2.9a, b**) indicated that the magnitude of the PE response within domains was significantly different. Also it is noticeable that the phase image color turns into black in the center of some domains. This indicates that the center part has a PE response in the opposite direction to the surrounding area, as shown in the scale bar. The other possibility is that the surface charge in this area influences the tip interaction.

In addition, **Figure A1** show the morphology and phase images directly corresponding to the amplitude images in **Figure 2.9**. The piezoresponsive regions (brighter regions) in **Figures 2.9a and b** were of similar size and lateral distribution but do not clearly correlate to the position of globular structures of the surface topography, confirming there was no cross-talk in the PFM measurements.

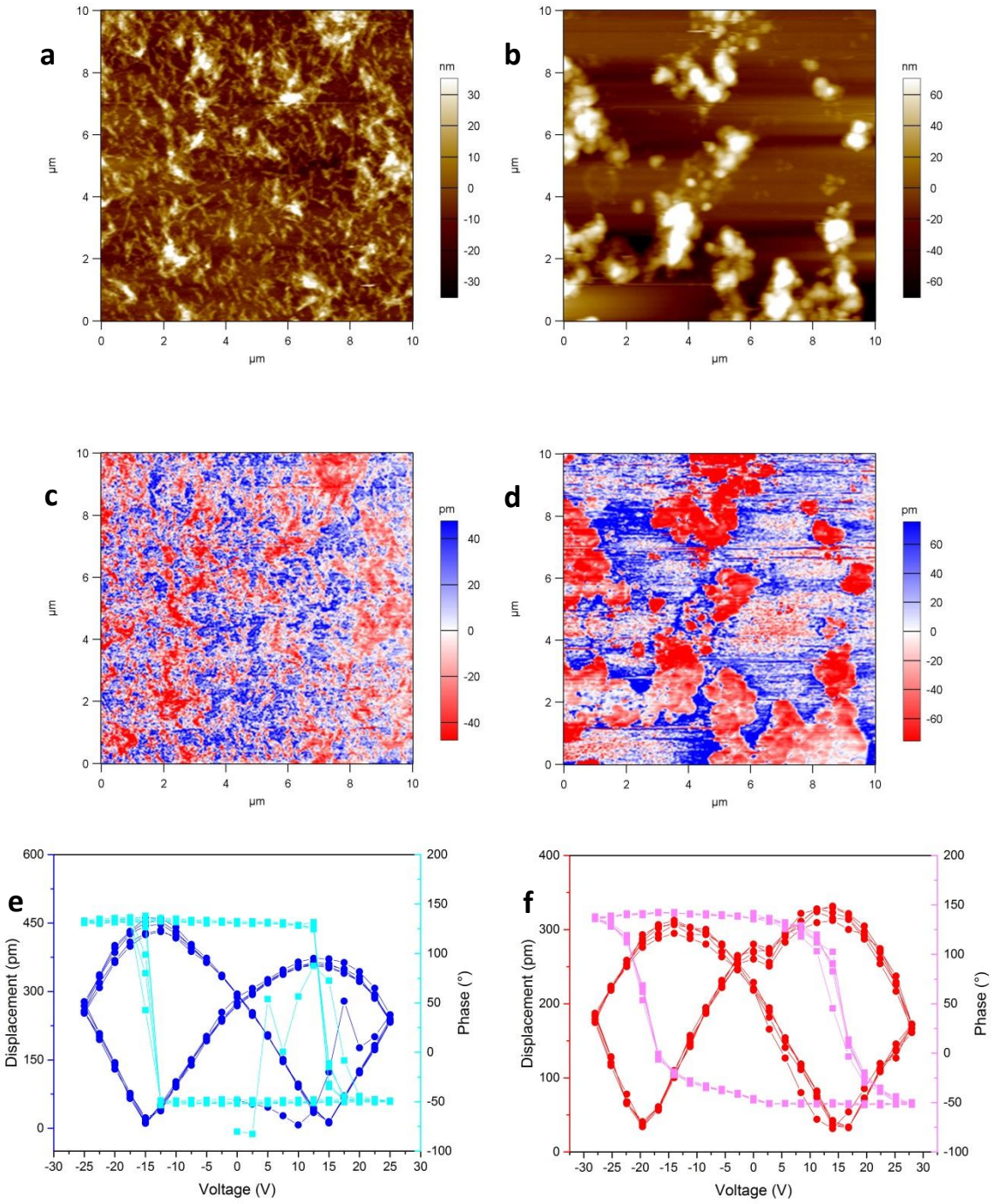

Figure A2. (a-c) PFM height, amplitude images and hysteresis loop of CNC nanowhisker and (d-f) PFM height, amplitude images and hysteresis loop of CNC nanosphere.

The piezoelectricity of the CNC whiskers and spheres is quantified using piezoresponse force microscopy (PFM) on drop cast films consisting of dispersed individual whiskers/spheres, with some area of aggregates on a gold substrate, as shown above (the results in **Figure A2e.f** are SS-PFM on CNC films). The biased tip causes shear piezoelectric response and the displacement is monitored vertically. Both two types of CNC clearly show a piezoelectric response in PFM amplitude images (red regions), specifically indicating good agreement with the CNC covered area in contrast to the non-piezoelectric substrate. To further elucidate their piezoelectric response, PFM-based switching spectroscopy used to measure the local piezoresponse reveal that both nanowhiskers and nanoparticles exhibit classical butterfly loops in the amplitude response and 180˚ change in phase, thus confirming the completed and reversible piezoelectric dynamic.

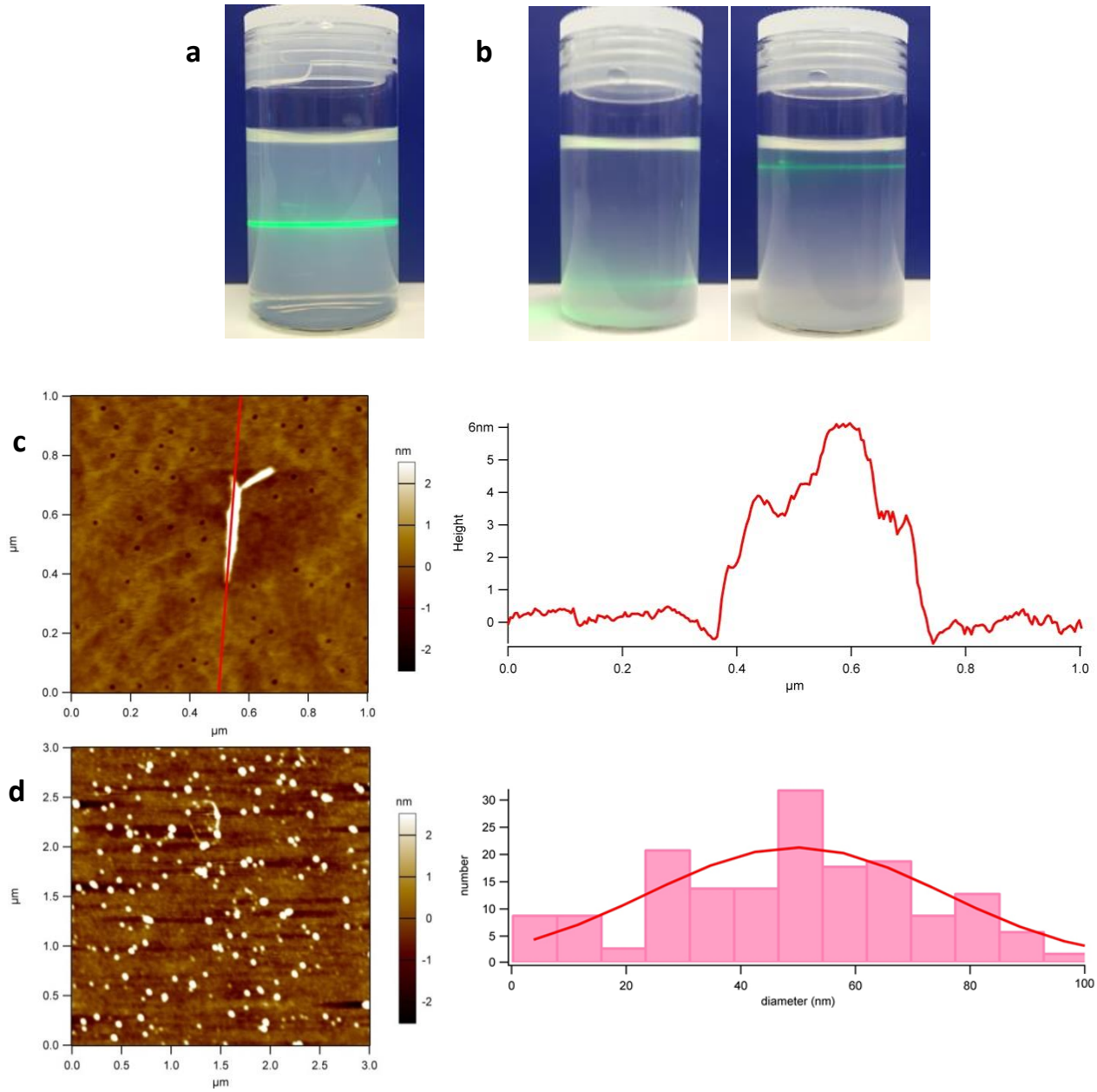

Figure A3. CNC (a) whiskers and (b) spheres after stay still for 48 hr. The Tyndall effect indicates the whiskers were well dispersed however the spheres had aggregations deposited. (c) AFM height image of single nanowhisker and the length profile. (d) AFM height image of upper layer of nanospheres suspension spread on mica and the sphere diameter distribution.

The aqueous suspensions of CNC nanowhiskers and nanospheres show different stability. The high-aspect ratio whiskers were well dispersed after standing for 48 h (**Figure A3a**). The longest nanowhisker was found to be 400nm (**Figure A3c**). The larger spheres (>100 nm) prefer to aggregate and only small spheres (<100 nm, **Figure A3d**) stay as in a homogenous phase (**Figure A3b**).

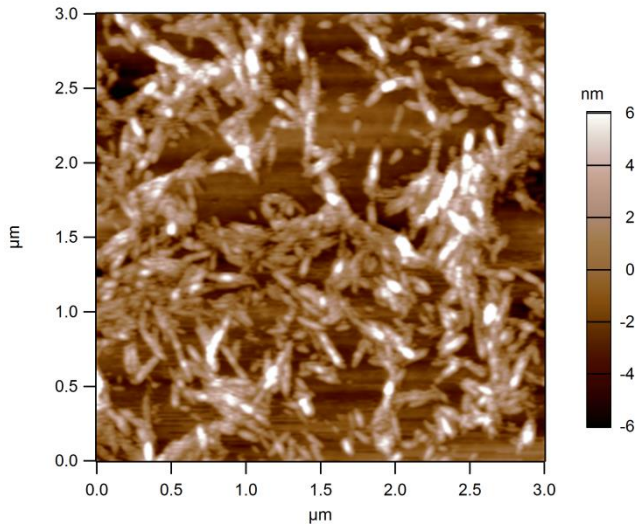

Figure A4. AFM height image of CNC nanowhiskers on glass slide surface.